Plasma deposition of thin film silicon at low substrate temperature and at high growth rate

Cover:
Impression of a silicon growth process, inspired on schematics encountered in various publications about nanocrystalline silicon growth. By the author, using POV-Ray.

ISBN 978-90-393-5206-9

This thesis was printed by Digital Printing Partners B.V., Houten.

Plasma deposition of thin film silicon at low substrate temperature and at high growth rate

Plasmadepositie van dunnefilm silicium bij lage substraattemperatuur en bij hoge groeisnelheid

(met een samenvatting in het Nederlands)

PROEFSCHRIFT

TER VERKRIJGING VAN DE GRAAD VAN DOCTOR AAN DE UNIVERSITEIT UTRECHT OP GEZAG VAN DE RECTOR MAGNIFICUS, PROF. DR. J. C. STOOF, INGEVOLGE HET BESLUIT VAN HET COLLEGE VOOR PROMOTIES IN HET OPENBAAR TE VERDEDIGEN OP MAANDAG 23 NOVEMBER 2009 DES MIDDAGS TE 12.45 UUR

DOOR

Arjan Daniël Verkerk

GEBOREN OP 22 OKTOBER 1979 TE MAARSSEN

Promotor: Prof. dr. R.E.I. Schropp

Co-promotor: Dr. J.K. Rath

The work described in this thesis was financially supported by the Netherlands Agency for Energy and the Environment (SenterNovem) of the Ministry of Economic Affairs of The Netherlands: program EOS (Subsidy Energy Research).

Contents

Chapter 1

Introduction

1.1 Solar energy and solar cells

With the world's ever rising energy consumption and the impending depletion of the fossil fuel reserves, research on alternative energy sources hardly requires an introduction. However, among the enormous variety in alternatives that are widely investigated, such as wind, tidal and hydropower energy, biomass power and geothermal heating, solar energy takes a special place.

The amount of power from the sun reaching our planet is tremendous. The energy received in only one hour by the earth is comparable to the energy consumed worldwide in one year. Solar power seems to be the most trivial source of energy, and yet it is quite a challenge to harvest this energy at a large scale with a reasonable efficiency. The most straightforward way to put solar power to electrical work is the use of concentrator systems in which the light is focused, through parabolic mirrors or Fresnel lenses, in order to heat a fluid that drives a turbine for electricity generation. The drawbacks of this type of system are the fact that only direct sunlight can be concentrated, and the relatively high maintenance costs that are involved because of the moving parts.

These drawbacks naturally reveal the advantages of photovoltaic solar cells which have practically unlimited scalability, with applications ranging from the power supply for watches, mobile phones and laptop computers, via medium sized installations on residential housing, on industrial complexes and in space, to large scale application in solar power plants. Moreover, photovoltaic solar panels are designed to operate for several decades without maintenance, since the panels have no moving parts (optional sun-tracking supports not taken into account), and can be encapsulated for protection against environmental influences.

1.2 Deposition and properties of thin film silicon solar cells

1.2.1 Thin film solar cells

Currently, the work horse of the photovoltaic economy is still the wafer-based silicon solar cell. But the tremendous growth of the photovoltaic market over the past years, has led to a silicon shortage which in turn stimulated research and investments on thin film alternatives for wafer-based cells [1]. Thin film silicon solar cells are typically about a hundred times thinner and use proportionally less silicon. Not only does that result in a strong cost reduction as far as the silicon base material is concerned, but it opens up a new area of fabrication methods and applications. Fabrication and storage can in principle be conducted in a roll-to-roll fashion and application on curved surfaces becomes feasible.

The use of thin film solar cells brings new challenges as well. Being deposited from the gas phase, high purity thin film silicon layers require investments in very high quality vacuum equipment, to prevent the incorporation of impurities in the material. But even when these measures are taken, the conversion efficiency of thin film silicon solar cells is significantly lower than that of wafer-based silicon solar cells. One of the reasons for this is that, in these drift-type solar cells, the collection of charge carriers is hampered by recombination in the bulk and at the interface with the defective doped layer at the front side, resulting in a reduced conversion efficiency for both the ultraviolet and the (infra) red end of the spectrum.

Notwithstanding these drawbacks, thin film silicon solar cell modules are presently commercially available at prices per unit of power output (Watt-peak) equal and even lower than conventional silicon solar cell modules. The increasing substrate sizes (up to 5.7 m^2) and the implementation of roll-to-roll production processes are likely to improve the price aspect even more in the near future.

1.2.2 Amorphous and nanocrystalline silicon solar cells

Hydrogenated amorphous silicon (a-Si:H) has been used for the fabrication of thin film solar cells for several decades. Typical for this material is the band gap of about 1.8 eV, which is relatively high, compared to crystalline silicon (c-Si), having a band gap of 1.1 eV. This makes a-Si:H a good semiconductor material for the conversion of the blue part of the

solar spectrum, since a larger fraction of the photon energy in that part of the spectrum is actually converted into electrical energy because of the higher band gap. Another difference between a-Si:H and c-Si is that the former behaves like a direct-band gap material unlike the latter; this results in a high absorption coefficient in the blue and green part of the solar spectrum. This makes the fabrication of very thin a-Si:H solar cells possible, on the order of 300 nm. A drawback of a-Si:H is the initial decrease in the conversion efficiency by typically 20% relative [1] with light soaking, due to the generation of light-induced defects in the a-Si:H material, during the first several hundreds of hours in operation. This phenomenon is named the Staebler-Wronski effect [2].

More recently, hydrogenated nanocrystalline silicon (nc-Si:H), also called microcrystalline silicon, is applied in thin film solar cells. This material has approximately the same band gap as c-Si, and therefore it is most suitable for the conversion of the energy in the red and infrared part of the solar spectrum, just like c-Si. It features also a low absorption coefficient due to an indirect optical band gap, although it is higher than the absorption coefficient of c-Si. Therefore, record efficiency thin film nc-Si:H solar cells typically have a thickness of only 1-2 μm. In the search for optimal device design, one of the challenges is to keep the actual cell thickness small enough to allow for a significant electric field, but to increase the optical path length via various light trapping schemes such as a textured front layer and a back reflector construction [3, 4]. Compared to a-Si:H, nc-Si:H has a higher stability against light soaking [5], although a degradation of the conversion efficiency of about 10% for nc-Si:H solar cells has sometimes been observed [5-7]. A key issue in the fabrication of nc-Si:H solar cells is the phase composition of the material, which consists of nm-sized crystallites in an amorphous environment. A too high crystalline ratio deteriorates the cell performance, among others by a decrease of the open circuit voltage [8]. Nanocrystalline silicon solar cells with relatively high open-circuit voltage of around 600 mV can be achieved at a relatively low crystalline ratio of about 30% [9].

The different properties of a-Si:H and nc-Si:H can be used in tandem solar cell designs, to take full advantage of the characteristics of each cell. The a-Si:H top cell, where the light arrives first, is then used to absorb the light in the blue part of the solar spectrum, while the nc-Si:H bottom cell takes care of the absorption of the red part, which is left unaffected by

the top cell. In this way, the energy of the blue photons is used more efficiently, and at the same time the high current from the nc-Si:H solar cell is obtained. Since the cells are stacked on top of each other they form a series connection, with more than twice the voltage of a nc-Si:H solar cell and more than half the current of an a-Si:H solar cell.

1.2.3 Deposition rate and substrate temperature

In addition to high conversion efficiency, two other aspects are of significant importance to unleash the full potential of thin film silicon solar cells.

One of these aspects is the increase of the deposition rate since it will have a strong effect on the industrial throughput, especially for nc-Si:H solar cells as bottom cells in tandem designs that require nc-Si:H absorber layers with a thickness of over 2 μm. Current deposition rates for record-quality solar cells in the laboratory are less than 1 nm/s, resulting in deposition times of the absorber layers in the order of hours. This will simply bottleneck the throughput in solar cell production via batch processing; in roll to roll deposition that will be even more significant since the deposition rate determines the length of the production line. If the nc-Si:H is deposited in a tandem structure together with a-Si:H, it becomes even more important to achieve the deposition of both the top cell and the bottom cell in a comparable time interval.

Increasing the deposition rate is not a straightforward process. Supplying higher discharge power and more silane source gas to the deposition plasma is harmful to the film quality. To compensate this, other measures have to be taken such as the variation of the reactor pressure, which in turn has its effects on the chemistry in the gas phase. The physics of a high-deposition rate regime are fundamentally different from that of the currently used low pressure regimes for high-quality films. Thus far, even when the necessary measures are taken, it has not been demonstrated that it is possible to increase the deposition rate by an order of magnitude without sacrificing a significant fraction of the conversion efficiency of the resulting solar cell, compared to the highest-quality material.

Another aspect of significant importance is the substrate temperature, which is related to substrate costs. Current record efficiency solar cells are deposited at a substrate temperature of around 200°C, since this temperature offers the best quality for both a-Si:H and nc-Si:H films. But to be able to deposit on cheap and flexible substrates such as polyethylene

terephthalate (PET), not only for use in roll to roll processes, but also to open up a whole new market of flexible, and lightweight photovoltaics, the substrate temperature has to be reduced to about 100°C. Again this is not achieved simply by reducing the substrate temperature, since the quality of the deposited film is strongly affected by the substrate temperature. Not only the surface chemistry is different at reduced temperatures, but also in the gas phase significant differences occur in density, powder formation and ion energy. To be able to compensate for these effects, a good understanding of these processes is of high importance.

1.3 Goal of this thesis

The goal of this thesis is to investigate the difficulties that arise when the regimes of high deposition rate and low deposition temperature are explored, both for material quality and deposition control; and to find ways to compensate the negative effects of these deposition regime changes, with the aim to approach the quality level of performance-optimized regimes in high deposition rate and low substrate temperature deposition conditions.

1.4 Outline

The next chapter is a dedicated chapter for the introduction of the experimental methods and techniques employed, ranging from plasma deposition via plasma diagnostics to optical and electrical material and solar cell characterisation.

Chapter 3 focuses on the effects of a reduced substrate temperature on the properties of the gas mixture and the energy flux of the ions towards the substrate. An introduction into the mechanism for powder formation is given and the part of this mechanism that has significant temperature dependence is identified. An instrument for the measurement of the ion current and the ion energy is described and the results obtained with this instrument are presented and discussed, together with possible methods to mitigate the effects of the reduced substrate temperature. The relation between the degree of powder formation and the substrate temperature is verified using plasma impedance analysis.

The subject of Chapter 4 is the transition regime from a-Si:H to nc-Si:H. The role of hydrogen in the transition is discussed and the use of the optical emission from the plasma deposition to predict the transition is revisited. The different mechanisms that undermine a

straightforward interpretation when switching to conditions for higher deposition rates are explained and an existing computer simulation was extended to incorporate optical emission prediction for a good understanding of its behaviour under the changing deposition conditions. With the results from this simulation, an easy to use model purely based on measurable quantities is derived that helps to convert the measured optical emission into an accurate prediction of the transition from a-Si:H to nc-Si:H.

The challenges that accompany high rate growth, as far as control of the crystalline ratio is concerned, are the topic of Chapter 5. It is elaborated in this chapter that simple variation of the hydrogen flow can not control the crystalline ratio in a regime of very high silane depletion, which is typical for the high-deposition rate regime. The key to the control of the crystalline development is the degree of this depletion. The strong effect of the initial gas conditions on the film homogeneity is demonstrated, and a few methods for improvement of the material homogeneity are offered and explored.

In Chapter 6 the properties of materials grown with very high deposition rates are presented. Both the material properties obtained from a series of layers with different deposition power around the transition from a-Si:H to nc-Si:H, and the performance of a typical high-deposition rate a-Si:H solar cell and a high-deposition rate nc-Si:H solar cell are discussed. The light-soaking stability of the high-deposition rate a-Si:H solar cell is investigated. Furthermore, a high-deposition rate nc-Si:H solar cell is subjected to a 1-MeV proton beam to investigate its radiation hardness and compare this to similar experiments from literature.

Chapter 2

Experimental techniques

2.1 Solar cell design

Both amorphous and nanocrystalline silicon solar cells have been deposited in the framework of this thesis. Each type of solar cell has distinct design considerations, although the principal sequence is conserved. A schematic view of the different components present in both types is shown in Figure 2.1.

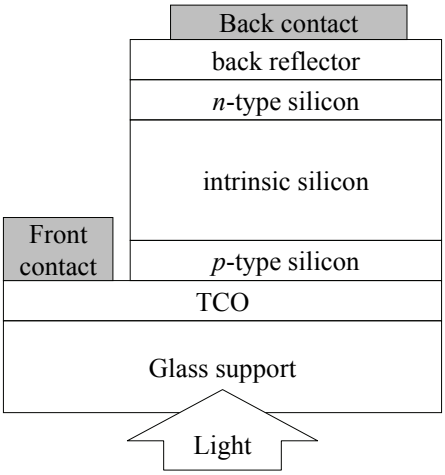

Figure 2.1: Schematic cross-sectional view of a *p-i-n* solar cell.

The amorphous silicon solar cells were deposited on a commercial Asahi U-type substrate, that combines glass with a SnO_2:F transparent conductive oxide (TCO) layer, which was given a surface texture that scatters light in the visible part of the solar spectrum, where the amorphous silicon conversion efficiency reaches its maximum. This surface texture is to some extent replicated by all layers deposited on top of the TCO. On top of the TCO subsequently a boron-doped a-Si:H:C *p*-type layer of ~10 nm, an intrinsic absorber layer of 200 to 300 nm and a phosphorus-doped *n*-type layer of ~20-30 nm of hydrogenated amorphous silicon (a-Si:H) films are deposited, hence this configuration is called a *p-i-n* configuration. After the silicon a ZnO:Al layer of 100 nm is deposited using RF magnetron

sputter deposition. Together with the metal back contact this layer forms a reflector that has the purpose of enhancing the reflection of the unabsorbed light via constructive interference. In this way the optical path of the light in the device is increased without sacrificing the strength of the electric field. The metal back contact, consisting of successively evaporated silver and aluminium, defines the area (4×4 mm^2) of the solar cell. The purpose of the aluminium layer is to prevent the back electrode from oxidisation during storage. After deposition of the metal back contact through a mask, the uncovered ZnO:Al is removed by etching in diluted HCl. Next to the main stack of films a strip of sputter-deposited silver on the Asahi TCO surface extends outside the deposition area for the silicon, to reduce the sheet resistance and to facilitate contacting in the characterisation experiments.

The solar cells with a hydrogenated nanocrystalline silicon (nc-Si:H) absorber layer are deposited on glass substrate covered with a texture-etched ZnO:Al TCO layer, made available by the IEF-5 institute at Jülich [10]. This ZnO:Al TCO layer is better suited to the deposition of nc-Si:H, because its transmission does not deteriorate in the atomic hydrogen ambient in the deposition regime for nc-Si:H. The feature size of the texture in this TCO layer is considerably larger compared to the feature size of the texture in the Asahi TCO layer used in amorphous silicon solar cells, since the optimal absorption for nc-Si:H is at longer wavelengths compared to amorphous silicon. On top of the TCO boron-doped *p*-type nc-Si:H layer of 27 nm is deposited, which has an additional function as a seed layer for the subsequently deposited intrinsic nc-Si:H absorber layer. After this *i*-layer, an a-Si:H *n*-layer is deposited with a recipe equal to the *n*-layer used in the amorphous silicon solar cells, because the lower conductivity of this material prevents side collection of charge carriers from outside the area that is defined by the back contact. Also, the compact nature of this amorphous layer prevents penetration of contaminants from the ambient into the cell. The back reflector structure consisting of a ZnO:Al TCO layer and a metal back contact is identical to the structure used in the a-Si:H solar cell.

2.2 Plasma deposition and characterization

2.2.1 Deposition reactor

All the materials and solar cells in this thesis are deposited using Very High Frequency Plasma Enhanced Chemical Vapour Deposition (VHF PECVD) in the ASTER ultra high vacuum (UHV) multi-chamber deposition system [11, 12]. The layout of the ASTER is depicted schematically in Figure 2.2. The system features a parking chamber for storing and gradual cooling of samples, a shutter-equipped viewport in the reactor for intrinsic material to enable spectroscopic measurements.

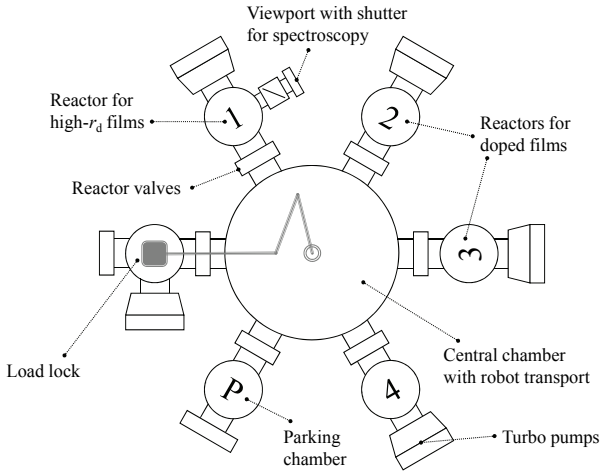

Figure 2.2: Layout of the ASTER deposition system.

The advantage of VHF PECVD over conventional Radio Frequency (RF) PECVD at 13.56 MHz is the increased electron density, which results in an increased dissociation rate, and the lower electron temperature and electrode voltage, resulting in reduced ion energy and consequently in improved material quality [13]. The frequency used for the fabrication of high deposition rate (r_d) intrinsic silicon (chamber 1) in this system is 60 MHz. Because of the shorter wavelengths in VHF PECVD compared to RF PEVCD, it is a greater technical challenge to achieve homogeneous power deposition, especially over large areas. To increase the homogeneity of films deposited in regimes of high silane depletion, the reactor for high-r_d intrinsic silicon deposition is fitted with a showerhead electrode which functions

as a gas distribution plate and powered electrode at the same time [14]. The inter-electrode distance is freely adjustable in the range between 5 and 27 mm.

2.2.2 Standard regimes for low and high deposition rate

In this thesis the results obtained in a high deposition rate regime for the deposition of nc-Si:H and a-Si:H are in certain places compared to the results of performance-optimized deposition of the respective materials. The deposition parameters for the different regimes are presented in Table 2.1.

Table 2.1: Comparison between the deposition parameters for high deposition rate nc-Si:H and a-Si:H and the deposition parameters for their respective performance-optimized (P.O.) regimes.

Material	*Regime*	r_d *(nm/s)*	*VHF power (W)*	SiH_4 *flow (sccm)*	H_2 *flow (sccm)*	*p (mbar)*	$d_{electrode}$ *(mm)*	T_{heater} *(°C)*
nc-Si:H	P.O.	0.5	20	3	84	5	6	252
	High-r_d	4.5	350	20	300	9	6	252
a-Si:H	P.O.	0.2	5	30	30	0.16	27	280
	High-r_d	3.2	200	20	300	9	6	252

2.2.3 Delivered power measurement

The VHF power is coupled to the reactor via a matching network with adjustable capacitors. Although the forward power at the power source is known, the power loss in the cables and the matching network may vary with the setting of the capacitors. Moreover, the coupled power may depend on the actual plasma conditions that determine the plasma impedance at the applied frequency. To be able to perform experiments at a constant, known delivered power to the plasma, a V/I Probe RF Impedance Analyzer from MKS Instruments was installed between the matching network and the electrodes. In this way, the actual delivered power to the plasma could be measured accurately. With the probe also the phase lag between the plasma current and the voltage can be measured, which provides information whether the plasma is in a capacitive or a resistive regime.

2.2.4 Optical Emission Spectroscopy

The use of the optical emission for the characterization of silane plasmas has been known for quite some time [15, 16]. For the Optical Emission Spectroscopy (OES) data presented in this thesis an Avantes MC2000 spectrometer is used to record the emission spectrum

from the plasma. The viewport to the reactor is equipped with quartz glass with sufficient transmission for the measurement of wavelengths in the ultraviolet, and a shutter to prevent deposition of silicon on the glass that would affect the emission spectrum. The emitted light is guided to the spectrometer via an optical fiber. The setup is shown schematically in Figure 2.3.

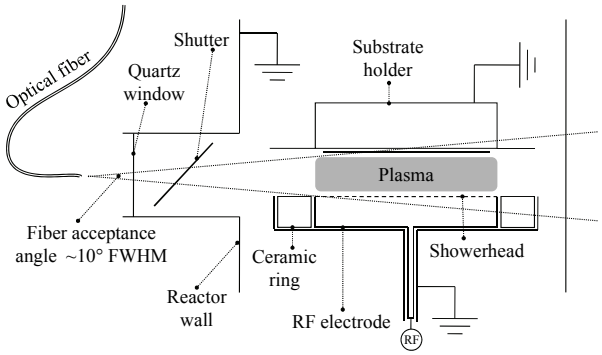

Figure 2.3: The setup for Optical Emission Spectroscopy at reactor 1 of the ASTER.

The emission from Si^* and SiH^*, emitting at 289 and 414 nm, respectively, are related to the electron impact dissociation of silane molecules. The Balmer H_α (656 nm) and H_β (490 nm) spectral lines originate from the electron impact dissociation of hydrogen molecules. Typical recording times for the spectra are in the range between 10 and 100 ms. In Chapter 4 and Chapter 5 it will be demonstrated how these emission peaks can be used to predict the a-Si:H to nc-Si:H transition and the deposition rate.

2.3 Material characterization

2.3.1 Dark and light conductivity

To measure the dark conductivity, the photoconductivity and thus the photosensitivity of the deposited materials, two parallel coplanar silver contacts are evaporated on the deposited film. A potential difference V applied between the contacts results in a measurable current J from which the conductivity can be determined according to

$$\sigma = \frac{Jw}{Vld}, \tag{2.1}$$

where d is the film thickness, w is the distance between the contacts and l is the length of the contacts. The photoconductivity σ_{ph} was determined as excess conductivity under AM1.5 light and the dark conductivity σ_d was determined at 300 K after annealing at 160 °C for 90 minutes in a vacuum environment. The photosensitivity is calculated as σ_{ph} / σ_d.

2.3.2 Raman Spectroscopy

The phase composition of the deposited nc-Si:H material can be investigated using Raman spectroscopy. In this technique the spectrum of the inelastically scattered light from the material is recorded. A fraction of the scattered light shows a frequency shift relative to the incident light that corresponds to phonons that are created or annihilated in the material under investigation. Therefore, the recorded spectrum reflects the phonon density of states. The observable modes are the transverse-optic (TO) mode of crystalline silicon (520 cm^{-1}) and the transverse-acoustic (TA, ~100-200 cm^{-1}), longitudinal-acoustic (LA, ~300-360 cm^{-1}), longitudinal optic (LO, ~380-450 cm^{-1}) and TO (~470-490 cm^{-1}) modes of amorphous silicon [17, 18].

The light source used for the incident beam is a Spectra Physics Ar^+-ion laser emitting at 514.5 nm. The scattered light is analysed in the range between 0 and 1200 cm^{-1} using a Spex triple grating monochromator and a Roper Scientific CCD camera. The laser light, that is incident at an angle of 30° with the investigated film, is polarized in the horizontal direction, while the measured signal, in a back scattering geometry, is polarized in the vertical direction, to suppress contributions from the laser line and the glass background.

To arrive at a Raman crystalline ratio (which is not the actual fraction of crystalline material, but rather a useful quantity that indicates the amount of material in the crystalline phase in a film) two different methods are used in this thesis. The first method is to simultaneously fit five Gaussian peaks to the obtained spectrum, where three fixed peaks are used at 330, 440 and 480 cm^{-1} associated with the amorphous phase and two variable

peaks, associated with the crystalline phase, are fit between 500 and 520 cm^{-1}. The definition for the Raman crystalline ratio R_c is then:

$$R_c = \frac{I_{510} + I_{520}}{I_{480} + I_{510} + I_{520}}, \tag{2.2}$$

where I_x denotes the integrated intensity of the contribution centred around x cm^{-1}. An example of the fitting procedure is shown in Figure 2.4.

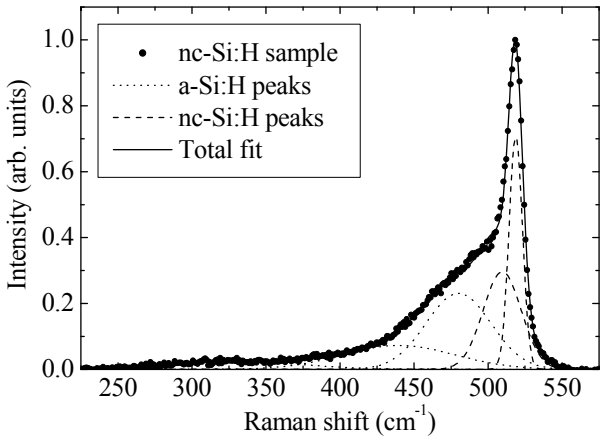

Figure 2.4: Example of the simultaneous fitting of five Gaussian peaks to the Raman spectrum of a nc-Si:H film after background subtraction.

A disadvantage of this method is the strong effect of the noise in the spectrum on the distribution of the intensity between the amorphous and crystalline peaks. Therefore, differences of 20% relative are not uncommon in the obtained R_c from spectra that appear very similar.

The second method used is the subtraction of an experimentally observed spectrum [19]. In this method the backgrounds of the Raman spectrum under investigation and a separately obtained Raman spectrum of a fully amorphous silicon is identified [18] and removed. Then this amorphous spectrum is scaled to match the investigated spectrum in a region where only the contribution from the amorphous phase to the spectrum is present. After subtraction of this scaled amorphous spectrum a differential spectrum remains that is representative of the crystalline phase in the material. The result of this process for a typical

spectrum is shown in Figure 2.5. The R_c is defined in this method as the ratio of the area under the residual spectrum to the area under the original spectrum after background subtraction, in the range between 375 and 575 cm^{-1}. This integration range is chosen so that the two methods result in roughly the same R_c for identical spectra.

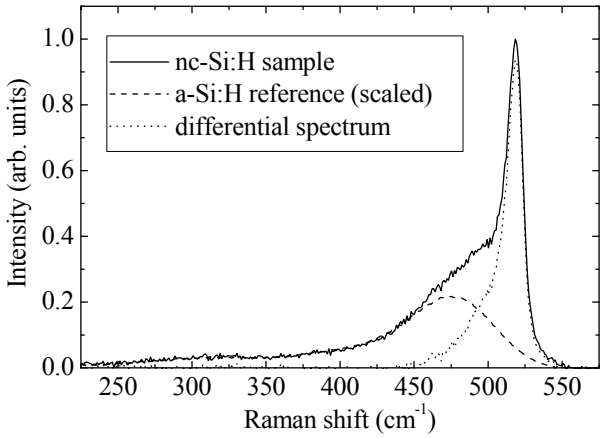

Figure 2.5: Example of the method of a-Si:H spectrum subtraction for determination of the Raman crystalline ratio R_c.

A drawback of this method is that it proved to be unsuitable for thin or weakly absorbing films where a contribution from the glass background is also present in the recorded spectrum. From a more fundamental perspective, it should be kept in mind that the Raman spectrum of a-Si:H may vary from sample to sample, depending on the measurement temperature, the deposition conditions and the microstructure of the amorphous content in nc-Si:H films. Nevertheless, whenever a sufficient agreement is encountered between the scaled a-Si:H spectrum and the investigated sample, this method provides a useful tool for the assessment of the phase composition; since it relies on only a single fitting parameter, the results obtained with it offer a higher consistency in series with small differences in the crystalline ratio.

2.3.3 Reflection / transmission

The thickness of deposited films is determined using reflection and transmission spectra simultaneously obtained from the same spot using a halogen lamp as light source, optical

fibres to feed the signals into two separate spectrometers that record the spectrum in the range from 380 to 1050 nm with a resolution of 512 pixels. This setup is made by W. Theiss Hard- en Software.

The layer thickness is found from a fitting procedure in which the simulated reflection and transmission, as calculated from a mathematical description of the dielectric function of the material [20], is fitted to the experimentally obtained spectra as implemented in the computer program 'SCOUT' [21].

2.4 Solar cell characterization

2.4.1 Current-Voltage measurements

The performance of the deposited solar cells is measured under AM1.5 light using a dual-beam WACOM super solar simulator employing both a halogen lamp and a xenon arc lamp. The spectrum of the solar simulator is calibrated to the 100 mW/cm^{-2} AM1.5 solar spectrum. The light spectrum and intensity is verified before every measurement using independently calibrated reference solar cells. The current-voltage (J-V) curve is recorded, at a temperature of 25°C, within a few tenths of a second, to prevent heating of the cells, by a computer controlled Keithley 238.

For an idealized diode, the J-V characteristics can be described by an equivalent circuit that consists of a photocurrent J_{ph}, a diode and a resistance R_p in parallel, series connected to a resistance R_s, resulting in the following J-V curve description:

$$J(V) = -J_{ph} + J_0\left(\exp\left(\frac{e(V - JR_s)}{nkT}\right) - 1\right) + \frac{V - JR_s}{R_p} \qquad (2.3)$$

Here J_0 is the dark saturation current, n is the diode quality factor, k is the Boltzmann constant, and T is the absolute temperature. J_0 and n are obtained from dark J-V measurements, where $J_{ph} = 0$. From AM1.5 J-V measurements the intersection of the curve with the current axis is identified as the short-circuit current density (J_{sc}). The slope at this point is $1/R_{sc}$; R_{sc} is associated with the parallel resistance R_p. The intersection with the voltage axis is identified as the open-circuit voltage (V_{oc}). The slope at the V_{oc} is $1/R_{oc}$; R_{oc} is associated with the series resistance R_s. The fill factor FF is defined as the ratio of the

maximum output power density to the product $V_{oc} \times J_{sc}$. The conversion efficiency is calculated as the ratio between the maximum power density and the AM1.5 light intensity of 100 mW/cm^2.

2.4.2 Quantum efficiency

The Quantum Efficiency (QE) of solar cells is defined as the number of collected electrons per incident photon, which is a function of the wavelength of the incident light. The QE in the wavelength range from 350 to 950 nm is determined using a reference measurement of the spectrum of a Xenon arc lamp using a monochromator and calibrated photodiode connected to a lock-in amplifier, to determine the flux of photons for each wavelength. After the reference measurement the calibrated diode is replaced by the solar cell to be measured, to determine the wavelength-resolved photocurrent caused by the now known photon flux. From the photon flux and the corresponding photocurrent the QE can be calculated.

2.4.3 Fourier Transform Photocurrent Spectroscopy

The midgap density of defect states in nc-Si:H is proportional to the sub-bandgap absorption coefficient; provided the scattering and the transmission of the TCO are not too strongly energy dependent an absorption coefficient (α) of 0.12 cm^{-1} at 0.8 eV corresponds to a midgap density of defect states (N_d) of 2×10^{16} cm^{-3} [22]. In this thesis, Fourier Transform Photocurrent Spectroscopy (FTPS) is used to determine the absorption coefficient in the absorber layer of nc-Si:H solar cells. FTPS is a sensitive technique for measurement of the photocurrent of solar cells with a high dynamic range [23]. A schematic drawing of the FTPS measurement is depicted in Figure 2.6.

The general principle is to use a Fourier-Transform Infrared (FTIR) spectrometer with an external beam exit and optional external detector. In a general FTIR spectrometer, an interferometer setup with a movable mirror imposes a spectrally dependent modulation frequency on the beam from the broadband light source. A Fast Fourier Transform algorithm converts the recorded signal from a photodetector from the time domain into the spectral domain. In a typical FTIR measurement, the detector remains unchanged and the difference between a measurement without sample and a measurement with a sample

reveals the absorption of the sample. However, in FTPS, the sample (the solar cell) is used *as the detector* and the comparison between a measurement with the solar cell as the detector and a measurement with a reference detector reveals the spectral sensitivity, or quantum efficiency, of the solar cell.

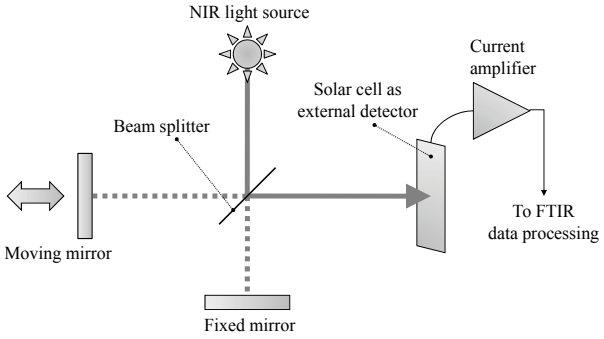

Figure 2.6: FTPS operating principle.

The FTPS setup that was used in this study employed a Bruker Optics VERTEX 70 FTIR spectrometer in combination with a Stanford SR570 low-noise current amplifier. The processing and analysis software, OPUS, that accompanied the spectrometer was used for FTPS as well. The light source was a halogen lamp, which is called the near-infrared (NIR) source by the software. It provided light with a spectral range that extended well into the visible (VIS) spectrum, however, so that it was a suitable source for the assessment of the photoresponse of nc-Si:H solar cells in the range 0.7 – 1.5 eV. The lamp spectrum was determined using, consecutively, two calibrated reference photodiodes as the external detector; a germanium (Ge) photodiode for measurement of the NIR part and a silicon (Si) photodiode for measurement of the VIS part of the lamp spectrum. Using the available calibration of these reference photodiodes, the wavelength-resolved photon flux from the light source was calculated. After this characterisation of the light source, the solar cell under investigation was used as the external detector, thus measuring its photocurrent.

The beam splitter (called BMS in the software) could be chosen to be KBr or quartz. Although the software recommended to use the KBr beam splitter in the spectral range between 0.7 and 1.5 eV, experiment showed that the transmission of the KBr beam splitter approached zero near 1.1 eV, making it unsuitable for photocurrent measurements in this

spectral range. Figure 2.7 shows that this low-signal point was really a consequence of the use of the KBr BMS: When the quartz BMS was used, both the Ge and the Si reference photodiodes generated enough photocurrent at 1.1 eV so that a single flux spectrum could be constructed from the two separate measurements. It is therefore recommended to use the quartz BMS in the FTPS setup to measure the absorption spectrum of nc-Si:H solar cells.

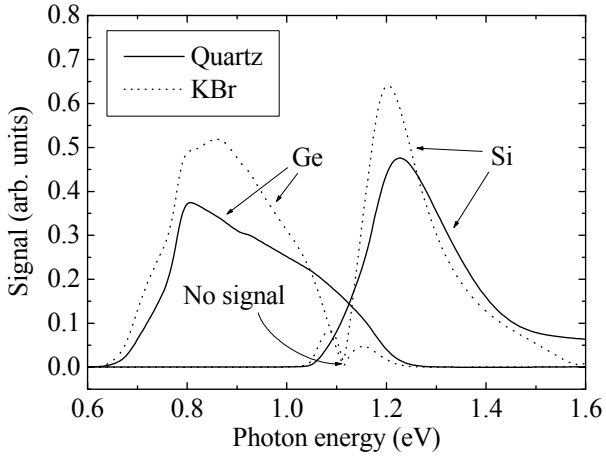

Figure 2.7: Comparison of reference cells and beam splitters available in the FTPS setup.

From the photocurrent measurement using the solar cell under investigation and the photon flux obtained using the calibrated reference photodiodes, the quantum efficiency (QE) can be calculated. For infrared light, where, for thin nc-Si:H films, the product of the absorption coefficient, α, and the film thickness, d, of the investigated film is much smaller than 1, the QE is proportional to the absorption coefficient, which is in turn proportional to the density of mid-gap defect states.

The absorption curves were calibrated to the c-Si spectrum at 1.4 eV. Because the absorption of nc-Si:H at 0.8 eV is many orders of magnitude lower than its absorption at 1.4 eV, it was not possible to measure the whole spectrum with one amplification setting of the current amplifier. Therefore, the low-absorption part was measured with stronger amplification, using a c-Si wafer as a low-pass filter to suppress the much stronger signal from higher photon energies. For proper calculation of the absorption, the reference

measurement with the Ge photodiode had to be performed with the same low-pass filter in place as well.

Chapter 3

The effect of substrate temperature on the plasma

Abstract

New applications for thin film silicon solar cells become possible with the shift towards cheap substrates with a low temperature resistance. Electronic quality and cell performance are strongly reduced when deposition temperatures are reduced below 200°C. Often the altered conditions at the growing surface are considered as the main cause for the performance decrease. On the other hand the addition of hydrogen in the gas mixture is known to have compensating, positive effects on the film quality at both optimal and reduced substrate temperatures. In this chapter, the effects of variation of substrate temperature and hydrogen dilution on the plasma conditions are investigated. The ion energy distribution and the plasma impedance are monitored at a range of substrate temperatures. The energy flux towards the film due to the ions decreases with decreasing substrate temperature. This is related to changes in gas density and composition. The effect of dust formation on the impedance is observed, indicating stronger dust formation at low substrate temperature. The ion energy can be partially restored by decreasing the concentration silane in the silane-hydrogen mixture, by increasing the power or by lowering the pressure.

3.1 Introduction

Thin film silicon solar cell technology has already delivered an initial conversion efficiency of 15.3%, employing a triple junction concept [24]. For tandem structures of hydrogenated nanocrystalline (nc-Si:H) and amorphous (a-Si:H) silicon solar cells even an initial conversion efficiency of 14.7% [25] has been achieved. At this point it is a logical step forward to investigate more of the promises of thin film solar cells, apart from the reduced material cost: reduced weight and the possibility of flexible, rollable photovoltaics. Therefore, the deposition process has to be transferred from the conventional substrates such as glass and stainless steel, to light-weight, flexible and cheap plastic substrates. One of the methods to achieve this has been demonstrated by the company Nuon Helianthos,

using a lift-off process, in which the film is deposited on a temporary, heat resistant metal foil, and subsequently transferred to a plastic substrate, resulting in 9.4% conversion energy [26]. For direct deposition on plastics, one has to choose between deposition on expensive, high temperature resistant polyimide type plastics, or on cheap plastics with a much lower glass transition temperature. In the first case, conventional deposition temperatures can be applied, for example resulting in a tandem cell with a conversion energy of 10.1% [27]. However, in the second case the deposition temperature has to be lowered drastically, to be able to use plastics such as polyethylene terephthalate (PET), which can withstand only a low processing temperature of around 100°C. Deposition of a thin film solar cell using Plasma-Enhanced Chemical Vapour Deposition (PECVD) under these conditions and on this type of substrate has so far reached 5.9% conversion efficiency [28].
Several clues have been proposed to improve the understanding of the effects of lower substrate temperatures on the film growth and quality. It is clear that an improved understanding of the mechanisms involved can be of much advantage in the development and improvement of low-cost silicon solar cells. This chapter addresses the way in which key figures in the plasma process are affected by changes in the substrate temperature.

3.2 Known causes and cures for low process temperature problems

3.2.1 Effects of low substrate temperature on the material quality

For both a-Si:H and nc-Si:H a minimum in the defect density is found in films deposited with a substrate temperature around 200°C [29]. Infrared absorption measurement and hydrogen evolution experiments indicate an increased density of defects and weak bonds in films deposited at reduced process temperatures, as well as a decreased compactness and higher porosity, compared to films deposited at substrate temperature of 200°C [30, 31]. Using transmission electron microscopy even macroscopic defects can be identified such as an elongated void structure and columnar amorphous growth [32]. These structural defects lead to a lower initial efficiency of the solar cells employing these films.
The negative effects described above can partially be ascribed to the decreased surface mobility of SiH_3 molecules at the growing surface [29, 32]. One of the benefits from

PEVCD is that it takes advantage of the energy and flux of ions so that the amount of extra kinetic energy arriving at the growing film can be utilised and controlled. The effects of changes in substrate temperature on these important plasma properties are not well understood.

3.2.2 Effect of hydrogen dilution on amorphous silicon

By optimization of the hydrogen dilution the negative effects of the reduced substrate temperature can at least partially be compensated. At standard substrate temperatures, the admixing of hydrogen into the silane feedstock gas (hydrogen dilution) was shown to be beneficial to the stability of solar cells against light-induced degradation [33], due to an increased medium-range order of the amorphous network [34, 35]. Such a material, deposited in the proximity of the amorphous-to-nanocrystalline transition but on the amorphous side, is often called "protocrystalline" silicon. Similarly, hydrogen dilution can be applied to improve the material quality at low deposition temperatures [36].

Experiments showed that for lower process temperature, relatively more hydrogen is necessary to achieve optimal material: Thin amorphous silicon films have been deposited on glass using Very High Frequency (VHF) PECVD at 50 MHz in the ASTER [12] high vacuum multichamber deposition system at different substrate temperatures using a mixture of silane and hydrogen. The heater temperatures used were 280°C, 157°C and 50°C, calibrated to achieve substrate temperatures of 200°C, 100°C and 39°C, respectively. It was found that the silane concentration, defined as the ratio of the SiH_4 flow to the total flow, had to be decreased from 50% to 6.3% and to 2.4%, going from high to low substrate temperature, in order to obtain optimal device quality material for that particular substrate temperature.

The a-Si:H material with the highest quality in the series deposited at 100°C had a photoresponse of 10^6. To confirm this quality, this material has been used as the absorber layer in test solar cells deposited on a stainless steel substrate with a smooth Ag/ZnO back reflector in an n-i-p configuration. The solar cell showed a conversion efficiency of 5.3%.

3.2.3 Dust formation and the gas temperature

Another mechanism deteriorating the situation for films grown at low process temperatures can be found in the gas temperature dependence of the dust formation in the gas phase. When plasma properties like power, dilution and pressure are altered, a regime change may occur in the plasma. Two clearly distinct regimes are the dust free α-regime and the dusty γ'-regime [37-39]. The α-regime is the conventional, powder-free regime where electrons are mainly lost at the electrodes and the strongest electric field is found near those electrodes. The bulk of the discharge has a positive potential on average because of the mass difference between positive ions and negative electrons. The γ'-regime arises due to dust formation in the plasma bulk. The dust particles capture the electrons giving the plasma a lower electron density and higher resistivity which can be observed in the changing physical properties of the plasma, for example the impedance and the optical emission.

Dust particle formation can occur when negative ions become trapped in the positive bulk of the plasma, being repelled by the fields present at both electrodes. These ions grow into polysilanes according to a polymerisation reaction:

$$SiH_3^- + SiH_4 \rightarrow Si_2H_5^- + H_2 \tag{3.1}$$

$$Si_2H_5^- + SiH_4 \rightarrow Si_3H_7^- + H_2 \tag{3.2}$$

This chain reaction for cluster growth is stopped due to ion-ion recombination with positive ions, which are abundant in the discharge. For these clusters to remain 'trapped' in the bulk of the plasma, it is necessary that they acquire a negative charge again, by capture of free electrons. However, the capture cross-section depends strongly on the size of the clusters. Therefore, only clusters that are large enough, with a size of 2 nm and larger capture at least one electron before being lost via diffusion towards the electrodes. After electron capture, the clusters are trapped by the time-averaged electric field between the electrodes, until the next ion-ion recombination event. The trapped clusters can grow further until a critical concentration of 10^{10}-10^{11} cm^{-3} and a diameter of about 6 nm is reached; at this point the clusters start to coagulate together and the dusty γ'-regime sets in [40].

It has been reported that dust formation is strongly dependent on the gas temperature [41]. The largest temperature dependence is found in the initial polymerisation reactions such as Equations 3.1 and 3.2. The rate of these reactions is enhanced by vibrational excitation of the silane molecules in the plasma. However, according to Landau-Teller theory [42], the relaxation of these vibrational excitations at the walls and in the plasma bulk, depend exponentially on the gas temperature. Thus, at lower gas temperatures, the vibrational excitation of silane molecules decays more slowly, and as a consequence the polymerisation rate is enhanced. Therefore, in plasmas with a lower gas temperature, caused by for example a lower substrate temperature, the critical cluster concentration is reached much quicker.

3.3 Experiments with the ion energy analyser

3.3.1 Reactor volume and gas temperature

To determine the gas temperature T_{gas} at a given substrate temperature the, volume V of the plasma reactor needs to be determined. If the valve towards the pump system is closed, a constant flow of molecules S that can be calculated from the gas flow, which is set by the mass flow controller, gives rise to a linearly increasing number of molecules n in the reactor: $S = \mathrm{d}n/\mathrm{d}t$. V can be determined through the ideal gas law:

$$pV = nkT_{gas} \tag{3.3}$$

$$\frac{\mathrm{d}p}{\mathrm{d}t}V = \frac{\mathrm{d}n}{\mathrm{d}t}kT_{gas} \tag{3.4}$$

$$V = \frac{SkT_{gas}}{\mathrm{d}p/\mathrm{d}t} \tag{3.5}$$

In these equations, p is the chamber pressure and k is Boltzmann's constant. If the heater, the reactor walls and the gas are all at room temperature the gas temperature is assumed to have the same temperature. Using this method, it is found that the volume of the ATLAS reaction chamber $V = 10.58$ l.

After the reactor volume was determined, the pressure as a function of time with the pumping valve closed was measured at different substrate temperatures, while there was no plasma between the electrodes and no applied RF power. The pressure depended linearly on the time. Knowing the volume of the reactor, the average gas temperatures could now be determined at different substrate temperatures:

$$T_{\text{gas}} = \frac{\mathrm{d}p}{\mathrm{d}t}\frac{V}{Sk} \tag{3.6}$$

For heater temperatures of 50°C, 157°C and 280°C this results in average gas temperatures of 34°C, 54°C and 78°C respectively, at a typical total gas flow of 50 sccm. Because of the small heat capacity of the gas in the reactor (~10 mJ/K), heating of the gas occurs with a rise time of less than a second. Therefore it is well possible that the gas between the electrodes reaches a higher temperature compared to the gas in the remainder of the reactor. Therefore, the average gas temperatures determined here represent a lower limit to the actual gas temperature between the electrodes.

3.3.2 The retarding field ion energy analyser

In a separate reactor (in the high vacuum system ATLAS) that has a design similar to the reactor in ASTER where the films for the solar cells are deposited, an electrostatic ion energy analyser (Figure 3.1) was installed in order to measure in situ the ion energy distribution function (IEDF) and the ion current in relation to the deposition temperature and silane concentration.

The spacing between the grids in the analyser is 1 mm and the diameter of the aperture is 1 cm. The first grid, as seen from the discharge, is in the plane of the electrode and it was grounded to leave the plasma unaffected. To the next grid a potential of about -50 V was applied, repelling electrons and negatively charged particles. The potential of the third grid was varied between 0 and 50 V to allow ions with sufficient energies to pass. The last grid was kept at a constant negative voltage of -15 V to prevent any secondary electrons from contributing to the measured current. The current is converted to a voltage by a current amplifier and subsequently measured by a computer-controlled digital multimeter.

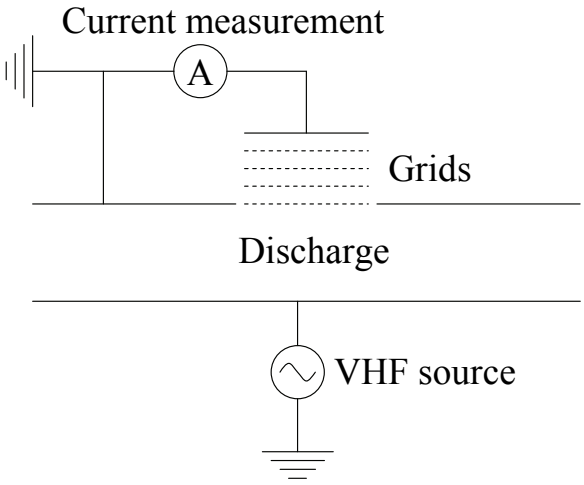

Figure 3.1: Ion energy analyser principle of operation.

The IEDF is obtained by differentiating the measured ion current with respect to the voltage applied to the third grid. The experiments with the analyser were performed using both 50 and 60 MHz plasma excitation frequencies. A series of layers was deposited with these parameters at all the three substrate temperatures mentioned above, to determine the deposition rate of the material at a silane concentration of 0.2.

3.3.3 Preliminary simulation and instrument characterisation

The experimental results were compared to available data from 1-D discharge simulations based on a fluid model [43], which is described in more detail in Subsection 4.3.1, to verify the correct operation of the ion energy analyser. This comparison is presented in Figure 3.2, where the dependence of the ion flux on the silane concentration is presented.

The most important observation from this comparison is that the same trend for the ion flux dependence on discharge parameters is found in both the experimental result and the simulation data. The simulated flux values exceed the measured flux values by a factor of 4. The discrepancy is explained by the difference between the available simulation data and the experiment: The power density was much lower and the simulated gas temperature was rather high in view of the observations in Subsection 3.3.1. Figure 3.6 shows how

increasing gas temperatures correspond to increased ion fluxes over a range of hydrogen dilution values.

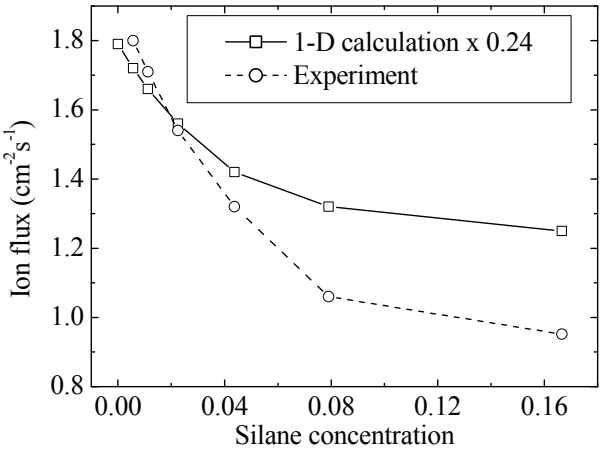

Figure 3.2: Dependence of measured and calculated ion flux on the silane concentration. The gas temperature was 550 K, the pressure was 0.16 mbar, discharge power was 13 mW/cm^2, the inter-electrode distance was 27 mm and the discharge frequency was 50 MHz.

Although the fluid model did not provide the ion energy distribution function, a good agreement exists between the sheath voltage drop in the simulations and the measured ion energy.

3.3.4 Ion Energy Distribution Functions at different dilutions

Typical IEDFs, measured using the ion energy analyser, are presented in Figure 3.3 for several values of silane concentration. The peak energy of the IEDF, the average ion energy and the ion flux are highest for a pure hydrogen discharge. If the hydrogen dilution is decreased, the peaks get less pronounced and eventually the IEDFs show a band of ion energies where a peak energy can no longer be identified. This behaviour is similar to the behaviour of the IEDF at higher pressures, suggesting an increased collision rate. In this case, the increased collision rate for the ions is not due to a decreased mean free path, but more likely due to an increased travelling distance caused by sheath thickening. Because the peak ion energy can not always be identified, in the following section the results are presented in terms of the total ion flux and the average ion energy.

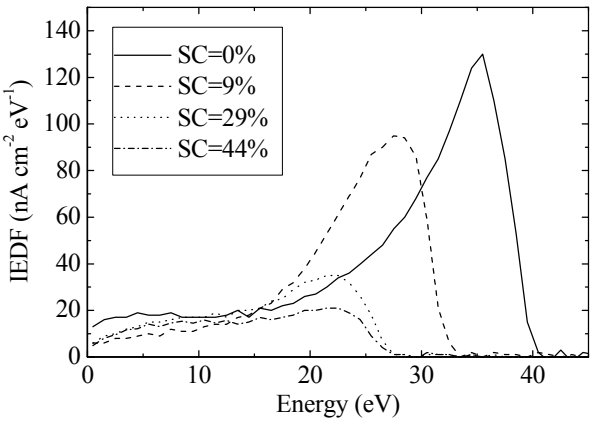

Figure 3.3: Examples of IEDFs recorded in discharges with the indicated silane concentration. The substrate temperature was 200°C, the pressure was 0.10 mbar, the discharge power was 80 mW/cm^2, the inter-electrode distance was 27 mm and the discharge frequency was 60 MHz.

3.4 Retarding Field Ion Energy analysis

3.4.1 Power variation

The increase of the ion energy with increasing VHF power is one of the difficulties that arise when one tries to increase the deposition rate of thin film silicon. Both the peak ion energy and the amount of ion energy per deposited silicon atom are key parameters that have an effect on the quality of the deposited films. The energy per deposited silicon atom should be at least 5 eV for compact film formation [44]. At the same time, if the peak ion energy is significantly higher than 16 eV, ions start to become implanted in the subsurface layers, resulting in defect formation [45]. Therefore, both the peak energy and the relation between the ion energy flux and the deposition rate are of importance to the film quality [46]. The effects of the VHF power on the ion current and energy are shown in Figure 3.4. Since the ion current density and the deposition rate are both roughly proportional to the VHF power, the amount of ions per deposited silicon atom remains constant. However, the average ion energy increases as well, and therefore both the amount of ion energy per deposited silicon atom and the peak ion energy increase.

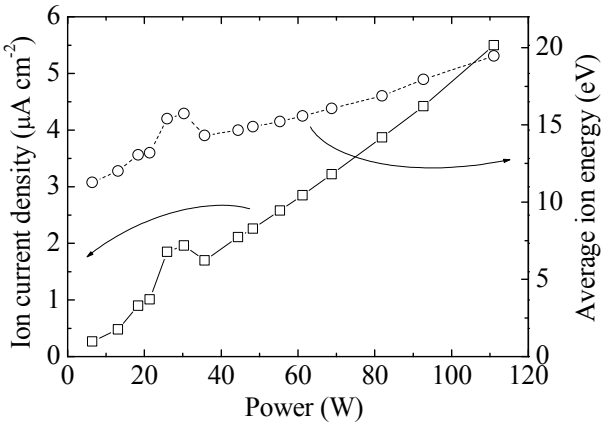

Figure 3.4: The effect of power on the ion energy and current. The deposition pressure was 0.10 mbar, the hydrogen flow was 10 sccm, the inter-electrode distance was 27 mm and the substrate was at room temperature. The discrepancies observed around 30 W are a result of difficulties with the manual pressure valve.

3.4.2 Pressure variation

In a low pressure VHF discharge, the majority of the ions that arrive at the substrate will have an energy corresponding to the potential difference across the plasma sheath. This may be well above the threshold for defect formation mentioned in the previous subsection, especially when the power is increased with the aim to achieve higher deposition rates.

An increase of the pressure can reduce the ion energy, because the mean free path for the ions is reduced, so that an increasing amount of ions lose their energy in collisions with molecules on the route towards the electrodes. This will affect the shape of the IEDFs significantly. The distribution will broaden and the average ion energy will decrease; the ion current will decrease as well, because of positive and negative ions exchanging charge in the increased number of collisions.

In Figure 3.5 the peak ion energies are presented for a pressure series in a pure hydrogen plasma. The observed ion energies at the low-pressure end were rather high, partially because the power was high compared to, for example, the standard regime for a-Si:H deposition (subsection 2.2.2), and also because this was a pure hydrogen plasma, which showed an *rms* voltage of 60 V. If the pressure is increased too much, the ion energy may fall below the threshold for beneficial effect to the film compactness. Moreover, the

increased pressure increases the probability for dust forming polymerisation reactions in the gas phase.

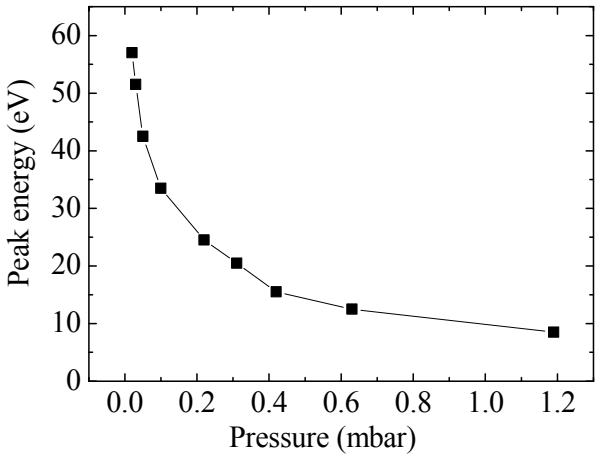

Figure 3.5: Measured peak ion energy as a function of pressure of a pure hydrogen plasma. The VHF power was 12 W, the hydrogen flow was 20 sccm, the electrode distance was 27 mm and the substrate temperature was 200°C.

3.4.3 Hydrogen dilution variation at different substrate temperatures

Figure 3.6 shows the measured ion flux towards the substrate as a function of the silane concentration in the process gas.

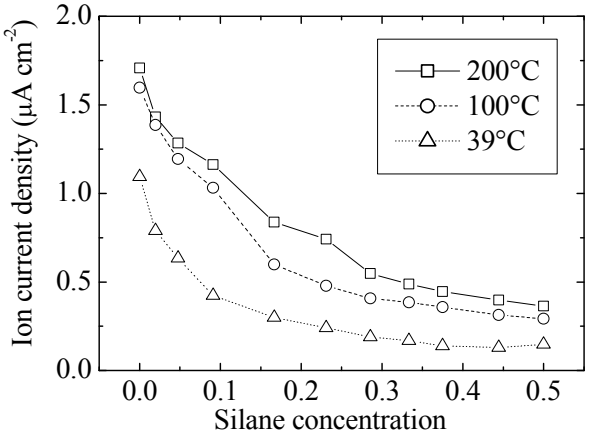

Figure 3.6: Ion current density as a function of the silane concentration at indicated substrate temperatures. The pressure was 0.10 mbar, the discharge power was 80 mW/cm2, the inter-electrode distance was 27 mm and the discharge frequency was 60 MHz.

Going from a hydrogen dominated discharge to a silane dominated discharge, the flux of ions vanishes almost completely, especially for the lowest temperature series. This indicates that the beneficial effect of ions to the film growth is drastically reduced in a low substrate temperature deposition when the process solely relies on the use of pure silane or a source gas with a high silane concentration. Furthermore, Figure 3.7 shows how the average ion energy is also significantly reduced.

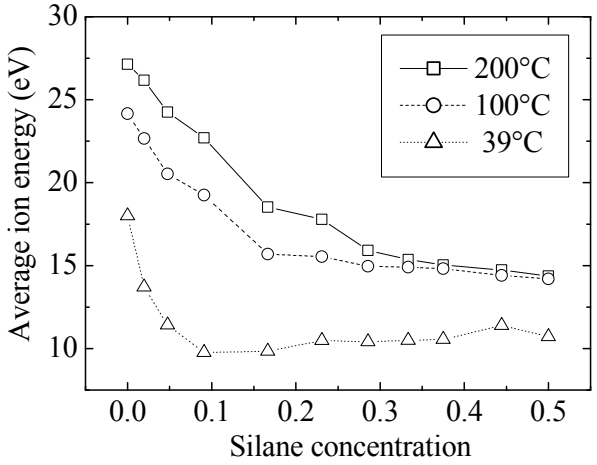

Figure 3.7: Average ion energy as a function of the silane concentration at indicated substrate temperatures. Other parameters are equal to those of Figure 3.6.

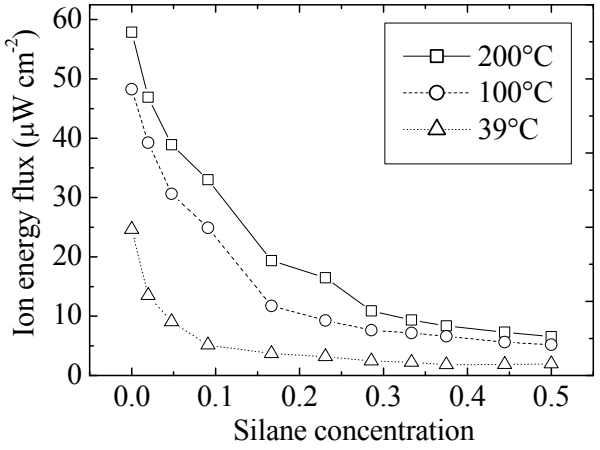

Figure 3.8: Ion energy flux as function of the silane concentration at the indicated substrate temperatures. Other parameters are equal to those of Figure 3.6.

Figure 3.6 and Figure 3.7 may be combined to obtain the ion energy flux (Figure 3.8).
It can be concluded that the total ion energy carried to the growing silicon film is strongly reduced when the deposition temperature is lowered from 200°C to 39°C at a constant silane concentration. Therefore, in order to restore the original optimal ion energy condition of 200°C, it is a reasonable solution to decrease the silane concentration. This is in agreement with the experimentally found requirement of higher hydrogen dilution to achieve device-quality thin films when decreasing the substrate temperature (see Subsection 3.2.2).

3.4.4 Increasing the ion energy by power or pressure variation

Although an increased hydrogen dilution has a positive effect on the ion energy in the deposition of films at a lower substrate temperature, it has a negative effect as well. The increased hydrogen dilution, at a fixed total flow to keep the residence time unchanged, leads to a lower deposition rate because of the lower silane flow and because of etching of the deposited film [47]. It is therefore worthwhile to investigate if the same effect on the ion energy could be obtained using a method that does not have this negative effect on the deposition rate. Possible methods are the increase of the RF power (Subsection 3.4.2) and the decrease of the pressure (Subsection 3.4.1). Figure 3.9 shows the IEDFs for a typical deposition regime, the same regime at lower substrate temperature, and the two best attempts of reproducing the shape of the high temperature IEDF at low temperature using each of the ion energy adjustment methods. In the figure, the integrated ion energy flux of each IEDF is indicated near the corresponding peak. This ion energy flux is calculated using a numerical evaluation of the integral

$$\frac{1}{e}\int_0^{40} IEDF(\mathrm{eV})E(\mathrm{eV})\mathrm{d}E\,, \tag{3.7}$$

where E is the ion energy.

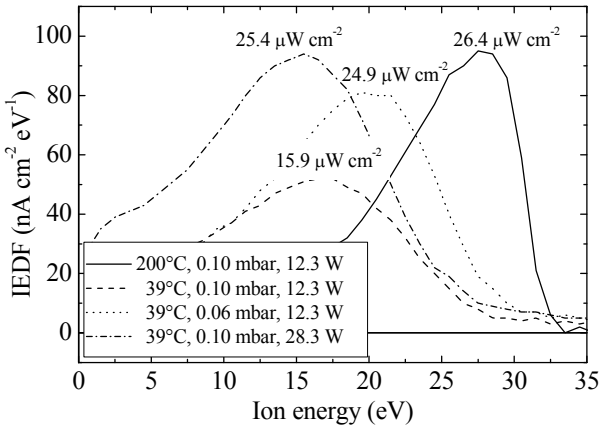

Figure 3.9: Restoring the energy flux found at high substrate temperature by means of power or pressure variation at low temperature. The silane concentration is 0.1 and the substrate temperatures are indicated. The peak energy of the high substrate temperature cannot be restored. The integrated ion energy flux of each IEDF is given in the figure near the maximum of the corresponding peak.

The IEDF obtained at a low substrate temperature has a broader shape and a lower average ion energy compared to the IEDF obtained from the otherwise similar regime at a higher substrate temperature. The effect of the pressure decrease is an increase of both the ion current and the ion energy. However, the effect of the power increase is an increase in the ion current, but a decrease in the ion energy and an overall broadening of the ion energy distribution. This indicates that a regime transition takes place, from the α-regime to the dusty γ'-regime. In the γ'-regime powder starts affecting the discharge properties via two different mechanisms. Firstly, the larger particles capture electrons more efficiently, increasing the resistive character of the discharge and resulting in broader and weaker electric field near the electrodes. Secondly, the larger particles, which are formed in this regime, scatter the ions that are accelerated towards the electrode, which causes the broadening of the ion energy distribution.

In conclusion, the IEDFs reveal that it is possible to restore the ion energy flux that was present at the higher substrate temperature, but that the peak energies of the IEDFs in the modified deposition conditions are different compared to the original peak energy.

3.5 Effects of low substrate temperature on plasma resistance and deposition rate

3.5.1 Plasma resistance at different substrate temperatures

In the ASTER deposition system the effect of substrate temperature on the electrical properties of the plasma were investigated. The hypothesis that the low substrate temperature results in a lower gas temperature and therefore a higher probability for dust formation is supported by these measurements: Figure 3.10 shows the phase difference between the alternating current through and the alternating voltage across the electrodes.

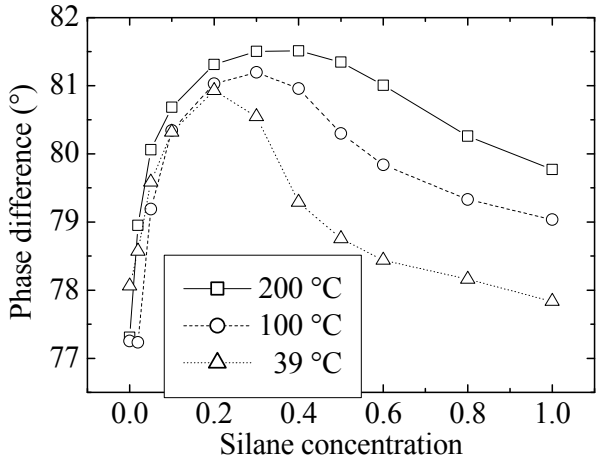

Figure 3.10: Phase between current and voltage as function of silane to hydrogen flow ratio for different substrate temperatures. Other parameters are equal to those of Figure 3.6.

The more this phase difference departs from 90°, the more resistive the plasma is. On the hydrogen rich side the electron density must be lower because the ionization energy threshold for hydrogen is much higher than that for silane. This effect is not dependent on the temperature.

In the silane rich part of the figure the resistance of the plasma is also increasing, as can be observed in the decrease in the phase. This change in the phase marks the transition into the γ'-regime, characterised by electron loss in the bulk of the plasma, because the electrons are captured by dust particles and spent in negative ion formation. In this case the phase

decrease is clearly dependent on the substrate temperature, confirming again that stronger particle formation occurs at lower substrate temperatures.

3.5.2 Deposition rate of materials deposited at varying substrate temperatures

Substrate temperature variation might influence the growth rate and film compactness. Therefore, a series of three films was deposited at a fixed silane concentration at the three substrate temperatures used in this chapter. Figure 3.11 shows the deposition rate and refractive index of these films as a function of substrate temperature.

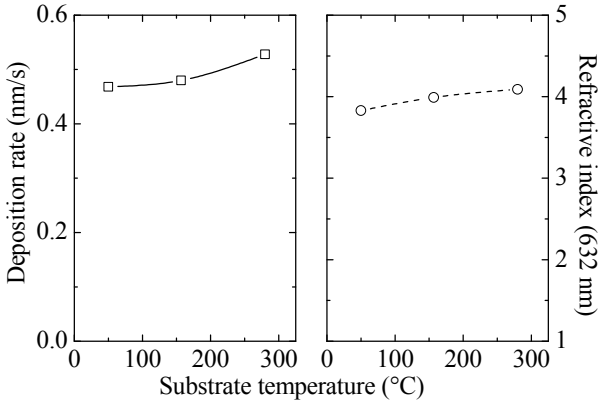

Figure 3.11: Deposition rate and refractive index as function of the substrate temperature. The silane concentration was 0.2. Other parameters are equal to those of Figure 3.6. The dotted lines are a guide to the eye.

Both the deposition rate and the refractive index increase with increasing substrate temperature. The increasing deposition rate indicates that an increased amount of silicon species is deposited at a higher substrate temperature. Moreover, at higher substrate temperature, the deposited films appear to have a higher compactness.

3.6 Discussion

A possible explanation for the effect of decreasing temperature on the ion energy is that it originates from the increase in the gas density that accompanies the decrease in gas temperature. This increases the ion energy loss due to the increased rate of collisions. This is in agreement with the observation that the shape of the IEDFs is becoming broader, not

only when the pressure is increased as in Subsection 3.4.2, but also when the temperature is lowered at a constant pressure, as became clear from Figure 3.9. However, in Subsection 3.3.1 it was shown that the relative differences in the gas temperature are much smaller than the corresponding relative differences in the substrate temperature and therefore, the observed effect on the ion energy cannot be explained from the gas density perspective only.

It was investigated whether the effect of temperature on the deposition rate and the compactness of the material can provide an additional explanation. Every deposited silicon atom yields two extra hydrogen molecules in the gas phase, when incorporation of hydrogen in the film is neglected. Therefore, a decrease in the deposition rate may cause a significant shift in the actual gas mixture towards higher silane concentration, resulting in lower ion current and energy. Since the fraction of the silane actually used in deposition in this regime is estimated to be 20% at most, and the deposition rate decreases by 11% according to Figure 3.11, this would give an increase of the 'effective' silane concentration of about 2% within the temperature range investigated. Moreover, from the refractive index, the material compactness appears to increase at higher temperatures as expected, resulting in an extra shift towards a higher effective silane concentration. Although small, the changes in both the deposition rate and the refractive index shift the energy curves in the correct direction to partially account for the observed effects.

The observation that the ion energy is restored with increasing hydrogen dilution can be explained via the electron temperature: In order to sustain a discharge in a hydrogen gas, an important electron impact ionisation mechanism will be:

$$H_2 + e^- \rightarrow H_2^+ + 2e^- \qquad (3.8)$$

This mechanism has a threshold energy of 15.4 eV [48], whereas for electron impact ionisation mechanisms for silane, such as

$$SiH_4 + e^- \rightarrow SiH_2^+ + 2H + 2e^- \qquad (3.9)$$

an electron energy of 11.9 eV is sufficient. To sustain a discharge in a gas with a low SiH_4 concentration, a higher electron temperature is necessary, resulting in a higher plasma potential and consequently higher ion energies compared to a pure SiH_4 discharge. At the same time, a hydrogen-rich mixture, in which cluster formation is less probable, causes the discharge to move towards a more capacitive regime. To compensate for the decrease in phase overlap between voltage and current at constant delivered power, the RF voltage will increase. This will result in an increasing ion energy as well.

3.7 Conclusions

The plasma properties depend significantly on the substrate temperature during the deposition of amorphous silicon using a low pressure VHF PECVD deposition process. The experiments show that both the ion flux and the average ion energy decrease with decreasing deposition temperature. On the other hand, the experiments also indicate that a solution exists in compensating the temperature effect by proper adjustment of the silane concentration. Variation of pressure and RF power can also be applied to increase the ion energy flux, but, contrary to adjustment of the hydrogen dilution, these methods do not restore the peak value of the ion energy distribution in a high-substrate temperature regime.

Chapter 4

Prediction of the phase transition using Optical Emission Spectroscopy

Abstract

The literature on the transition mechanism from amorphous (a-Si:H) to nanocrystalline (nc-Si:H) silicon is reviewed. It is known that a threshold in the flux ratio of atomic hydrogen to silicon species at the growth surface determines nc-Si:H growth in Plasma-Enhanced Chemical Vapour Deposition (PECVD). In some cases this threshold is also reflected in the easily obtained optical emission ratio H_α/Si^*. The development of a simulation for silane discharges and the recent inclusion of various optical emissions into this simulation are reviewed as well. A comparison is carried out between experimental and simulated emission in different deposition conditions, showing good agreement.

A correction factor, solely based on in situ obtainable quantities, for the optical emission ratio H_α/Si^* is derived that make this ratio reflect the flux ratio of atomic hydrogen to silicon species at the electrodes in a much wider range of deposition conditions, including the high pressure, high power regime.

4.1 Introduction

High quality thin film silicon, hydrogenated amorphous silicon (a-Si:H) as well as hydrogenated nanocrystalline silicon (nc-Si:H), is obtained in a Plasma-Enhanced Chemical Vapour Deposition (PEVCD) deposition regime close to the transition from a-Si:H to nc-Si:H [49, 50]. Therefore, after the technical requirements such as ultra high vacuum, very pure source gases, suitable reactor design, etc. have been met, one of the challenges of optimal material deposition is to find the transition regime and control the process parameters accordingly. It would be very useful for industrial, inline production systems if a suitable indicator could be found to accurately monitor the crystalline ratio of the deposited material in situ for quality assessment of materials and solar cells.

Conventionally, investigating the phase composition of a layer is a time consuming process that is done ex situ using Raman spectroscopy or X-ray Diffraction (XRD). A typical

sequence includes loading substrates and evacuating the deposition system, heating the substrate up to about 200°C, depositing a sufficiently thick layer, cooling down, venting and finally the characterisation. The characterisation should also include a determination of the thickness of the deposited film to interpret the phase composition correctly, since the phase composition shows a development with increasing thickness. Characterization methods observing the deposition directly in the deposition reactor are in use, such as in situ Optical Emission Spectroscopy (OES) [51]. Another method employing OES is the etch product detection method [52], which takes advantage of the optical emission from a hydrogen plasma etching step, using the fact that etch rate of a-Si:H is different from that of nc-Si:H. A different approach is found in the use of real-time spectroscopic ellipsometry to probe the phase composition of the growing film [53-55]. Lastly, measurements of the residual silane concentration at the pump line, employing infrared spectroscopy, have been shown to correlate with the observed phase composition [56]. All of these procedures offer considerable speed advantages over the ex situ method and have revealed key insights in the plasma process. In this chapter an extension of the in situ OES method is presented, enabling this simple technique to be used in an increased range of PECVD conditions, by providing a correction procedure for plasma conditions that would otherwise cause inaccurate results.

4.2 Phase transition at different deposition conditions

4.2.1 Optical Emission Spectroscopy and the phase transition

Hydrogen plays a key role in the formation of nc-Si:H silicon, regardless of the method of deposition of the thin film silicon material. Both in Hot Wire Chemical Vapour Deposition (HWCVD) and in various forms of PECVD processes, series of varying hydrogen to silane ratios are used to arrive at the desired amount of crystalline phase in the nc-Si:H material.

More precisely, it was recognized through the years that it is the atomic hydrogen that interacts with silicon film at the growing surface [57] and in the growth zone close to the surface, to initiate and sustain nc-Si:H growth [58-63].

In a low pressure VHF PECVD process, the production of atomic hydrogen and silicon species is predominantly determined by electron impact dissociation reactions such as (threshold energy indicated):

$$SiH_4 + e^- \rightarrow SiH_3 \cdot + H \cdot + e^- \ (\approx 8 \text{ eV [64, 65]}), \tag{4.1}$$

$$SiH_4 + e^- \rightarrow SiH_2 \cdot + 2H \cdot + e^- \ (\approx 8 \text{ eV [64, 65]}) \text{ and} \tag{4.2}$$

$$H_2 + e^- \rightarrow 2H \cdot + e^- \ (8.9 \text{ eV [66]}). \tag{4.3}$$

A certain fraction of these dissociation reactions results in optical emission, where H_α (656 nm) and Si^* (288 nm) are of special interest since they are single and strong peaks in the UV-VIS spectrum of the discharge in a typical silane-hydrogen mixture and can therefore easily be detected.

Since the optical emission and radical production are closely related, the emission from a PECVD process may reveal information on the growth of the film. For example, Si^* emission has been correlated to the deposition rate [57]. But also the production of atomic hydrogen, that plays an important role in the transition to nc-Si:H growth, is predicted by the observed emission. This was clearly demonstrated by the discovery of a threshold value in the intensity ratio H_α/Si^* in a VHF PECVD process at which the phase transition occurred [51]. All process regimes with an intensity ratio H_α/Si^* below this threshold were found to produce a-Si:H material, and regimes with the emission ratio above the threshold resulted in nc-Si:H growth.

By estimation of the atomic hydrogen flux in a HWCVD process while monitoring the growth rate and the phase composition of the deposited material, a strong clue was found supporting the idea that a certain minimal flux ratio of atomic hydrogen to silicon to the surface of the growing film has to be generated in order to achieve nanocrystallinity [67]. Recently, evidence was found that the phase transition from a-Si:H to nc-Si:H is uniquely determined by the flux ratio of atomic hydrogen and silicon species [68].

Thus the flux ratio between atomic hydrogen and silicon species at the surface determines the phase transition. In many low pressure, low power deposition regimes, the emission ratio between the H_α and Si^* emission predicts this transition reasonably well, because the fluxes of atomic hydrogen and silicon species in these regimes are well related to the optical emission from the respective dissociation reactions.

However, unlike the flux ratio of atomic hydrogen and silicon species, the threshold value of the emission ratio is not a universal one. Not only is it dependent on the geometry of the experimental setup, the characteristics of the optics in use and the spectrometer sensitivity – constant factors which can be corrected for using a single calibration series – but the threshold is also dependent on some key process parameters such as the pressure and the substrate temperature.

4.2.2 Effect of pressure on the prediction by Optical Emission Spectroscopy

At elevated pressures, which are increasingly applied to achieve high deposition rate conditions, the proportionality between the optical emission and the production of the fluxes relevant to the a-Si:H / nc-Si:H transition may not hold anymore. This is because various gas phase reactions between the neutrals and the reactive species, mostly radicals that are not affected by the field, and negative ions that are trapped in the positive plasma bulk, become increasingly probable. One of the main reasons for the arising disproportionality between flux ratio and emission ratio is the abstraction reaction:

$$SiH_4 + H\cdot \rightarrow SiH_3 + H_2 \qquad (4.4)$$

This mechanism provides a new radical involving a silicon atom that may contribute to the growth and therefore to the silicon flux, at the cost of atomic hydrogen flux. Other mechanisms can appear such as the formation of ‘higher’ silanes and formation of silane respectively:

$$Si_nH_{2n+2} + SiH_2\cdot \leftrightarrow Si_{n+1}H^*_{2n+4},$$
$$Si_{n+1}H^*_{2n+4} + M \rightarrow Si_{n+1}H_{2n+4} + M \qquad (4.5)$$

$$H_2 + SiH_2 \cdot \leftrightarrow SiH_4^*,$$
$$SiH_4^* + M \rightarrow SiH_4 + M \qquad (4.6)$$

As illustrated in Equation 4.5 and Equation 4.6, the excess energy from the collision of the two particles in the first step of each mechanism has to be transferred onto an extra particle, M. Because of this requirement, these recombination mechanisms are strongly pressure dependent; they become significant when the pressure is in the mbar range [69]. The type of reactions discussed above causes the simple proportionality between the flux and emission ratios to fail at these pressures.

Apart from pressure, the electrode distance can play an important role relating the generation rate of hydrogen to its flux to the walls. The abstraction reaction mentioned above is proportional to the density of atomic hydrogen. The generation of atomic hydrogen is reflected in the optical emission of, for example, H_α. However, the density of atomic hydrogen is determined by the diffusion of atomic hydrogen in a typically hydrogen rich environment. For an increasing electrode distance, an increased concentration of atomic hydrogen is established before the flux to the walls, driven by diffusion, balances the generation rate. So the abstraction reaction is not only dependent on the pressure, but also on the electrode distance.

4.3 Flux determination by computer simulation

4.3.1 Description of the simulation and its development

Since the a-Si:H to nc-Si:H transition is determined by the flux ratios and not uniquely by the OES emission ratio, it is necessary to find out the behaviour of the fluxes and the way they depend on the various deposition process parameters. The method chosen here to arrive at this information is to investigate the transition regime with the use of computer simulation. A one-dimensional simulation for silane-hydrogen deposition plasmas is employed that has been developed by Nienhuis [43] based on the work of Passchier en Meijer [70, 71]. This simulation is constituted by two parts: Firstly the simulation contains a fluid model that consists of balances for all particles (electrons, ions and neutrals), a balance for the electron energy and the Poisson equation; secondly the simulation uses a

Boltzmann equation in the two term approximation to describe the electron energy distribution function for the available electrons. The contribution of Nienhuis to the model included gas-phase chemistry and particle-electrode interactions, so that, amongst others, the fluxes toward the electrodes of silicon species and atomic hydrogen can be predicted.
The existing simulation was extended [72] to incorporate the optical emission arising from electron impact dissociation reactions of silane and hydrogen, which are similar to the reactions described by Equations 4.1-4.3, although the threshold energies are significantly higher for reactions that result in excited Si and H atoms. This extension made it possible, using only one-dimensional simulations, to reproduce the experimentally observed emission trends that had been recorded in ASTER. In Subsections 4.3.2 and 4.3.3 the emission prediction capabilities of this extended simulation will be presented.

4.3.2 Comparison of simulation and experiment for conventional deposition

Good agreement exists between the experimentally observed emission from the OES setup described in Chapter 2 and the calculations of the emission as provided by the one-dimensional simulation, for various regimes of the deposition process. Figure 4.1 and Figure 4.2 show the results for a 'conventional' deposition regime, characterized by low pressure ($\leq$ 1 mbar) and low power density ($\leq$ 1 W/cm^2), and a correspondingly low deposition rate (< 1 nm/s). The emission is shown as a function of the hydrogen dilution R, which is defined as the flow ratio $f(H_2)/f(SiH_4)$. In the series represented by Figure 4.1 an electrode distance (d_e) of 27 mm was used and the dilution was varied via the SiH_4 flow. In the series represented by Figure 4.2 a d_e of 6 mm was used and the dilution was varied via the H_2 flow. In the figures, the simulated series have been scaled to match the magnitudes of the experimental series. This is necessary since the simulation provides only the produced emission, while the experiment records the emission as perceived by the optical emission spectroscopy setup, which is influenced by the reactor geometry, the spectrally dependent transmission of the viewport and the fiber glass, and finally the sensitivity of the CCD array of the instrument. Further discrepancy between simulated and experimental emission, which is a function of the dilution and appears most clearly in Figure 4.1, may be explained in terms of the non-uniformity of the plasma. The electrode distance was rather

large in that case, making it plausible that the optical setup monitors only a subsection of the active region, whereas the simulated emission is integrated over the whole (one-dimensional) region between the electrodes.

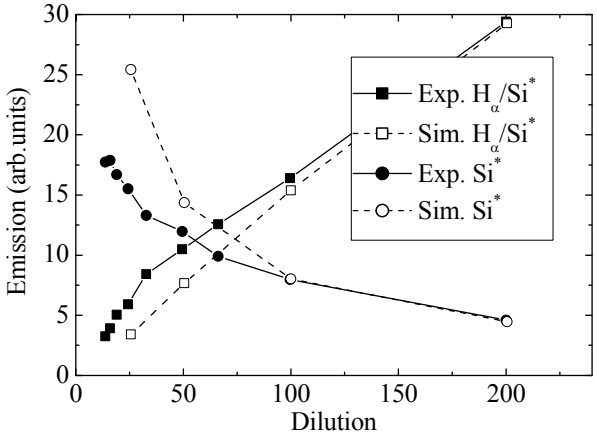

Figure 4.1: Simulated and measured emission from a deposition plasma with P = 15 W, p = 1.1 mbar, d_e = 27 mm, $f(H_2)$ = 100 sccm.

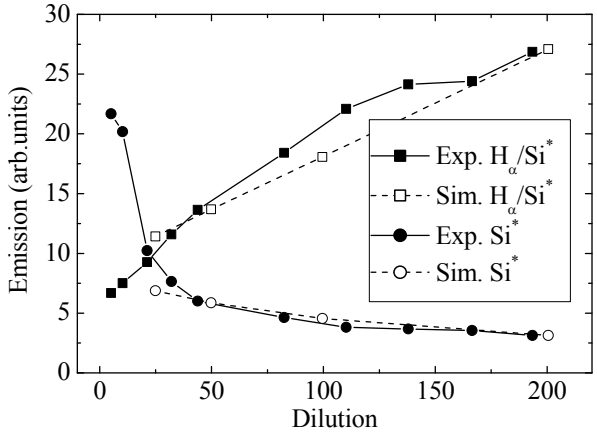

Figure 4.2: Simulated and measured emission from a deposition plasma with P = 15 W, p = 1.1 mbar, d_e = 6 mm, $f(SiH_4)$ = 1.2 sccm.

4.3.3 Comparison of simulation and experiment for deposition at higher power

For regimes of higher power and pressure, the simulation was limited to effectively 200 W of input power. At higher powers, the electric fields and the corresponding particle accelerations become too large for the simulation to converge. Therefore it was not possible to produce as much overlap between experiment and simulation in the high power and pressure case, compared to the conventional plasma. Nevertheless, the simulated emission, as presented in Figure 4.3, scaled according to the same procedure that was applied for Figure 4.1 and Figure 4.2, shows a remarkable similarity in trend. It can therefore be concluded that de simulation predicts the optical emission still reasonably well in this high pressure, high power regime.

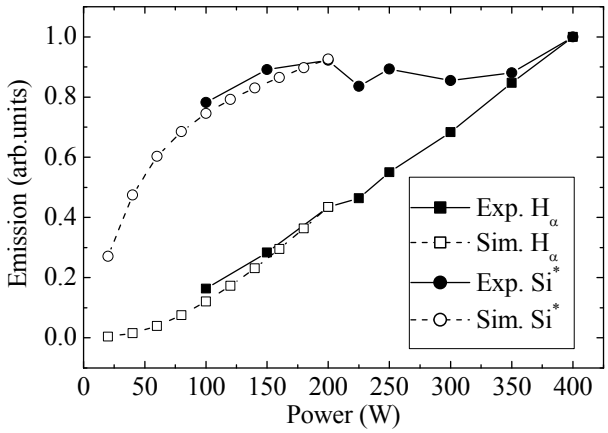

Figure 4.3: Simulated and measured optical emission from a deposition plasma with p = 9 mbar, d_e = 6 mm, f_{silane} = 20 sccm, $f_{hydrogen}$ = 500 sccm.

To be able to predict the fluxes of atomic hydrogen and silicon species the simulation has to provide these quantities as well. Although it is not a simple matter to verify the predicted atomic hydrogen flux, the silicon species flux that is calculated by the computer simulation can be compared to the ex situ, experimentally observed deposition rate, which is estimated from the thickness of the deposited films, calculated from the reflection and transmission spectra as described in Chapter 2. The results of this experiment can be found in Figure 4.4. In both cases the deposition rate shows the same increasing trend with increasing power, but the discrepancy between the graphs is rather high. An overestimation of the growth rate

by the simulation is also found in low pressure, low power regimes [43]. Some possible explanations for this discrepancy are the following: The density of the growing film was assumed to be equal to that of crystalline silicon (c-Si). Various deposition conditions such as the ion energy, the substrate temperature, the flux of atomic hydrogen and the transition from a-Si:H to nc-Si:H can alter the compactness of the deposited films, so that the actual density may vary up to 10% compared to the case of c-Si. This can explain the trend difference, but not the overestimation by the simulation. Etching of silicon species from the growth surface during the deposition is possible as well. Furthermore, there could be inaccuracies in the sticking coefficients of the various generated silicon species; also the residence times (τ_{res}) for the silicon species can be different from the assumed τ_{res}. Finally, small errors in the reaction rates for powder forming chain reactions could have a strong influence here; moreover, these reactions resulting in higher silanes are only included in the simulation up to a certain level. It is likely that the gas phase chemistry becomes richer at higher powers.

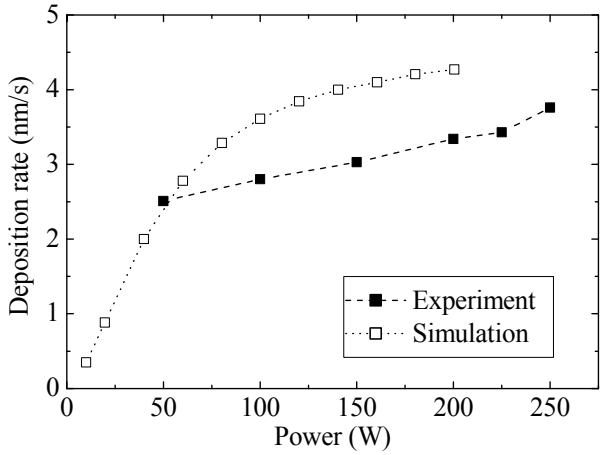

Figure 4.4: Growth rate for films obtained from simulation via calculated fluxes and from experiment via reflection/transmission measurements of films, deposited using a deposition plasma with p = 9 mbar, d_e = 6 mm, f_{silane} = 20 sccm, $f_{hydrogen}$ = 500 sccm.

Nevertheless, in simulating the flux ratio and comparing this to the emission ratio, the most important observation in Figure 4.1 to Figure 4.4 is that proportionality often exists between simulation and experiment. When the simulated emission is proportional to the

experimental results, the simulation can be used to predict the fluxes of atomic hydrogen and silicon species. When the proportionality factor between simulated and observed emission for a given deposition system is determined, in many cases the actual fluxes can be predicted using the simulation. These fluxes can in turn be used to predict the transition from a-Si:H to nc-Si:H growth.

4.3.4 Results of simulation of the emission and flux ratios

As the comparison between simulated emission and experimentally observed emission using optical emission spectroscopy gives positive results, the next step is to consider the fluxes of atomic hydrogen and silicon species towards the walls, taken from the simulation, for the prediction of the transition from a-Si:H to nc-Si:H material.

The relationship between the ratio of the optical emission H_α/Si^* and the flux ratio of atomic hydrogen to deposited silicon species is explored in Figure 4.5. The points in this figure represent series of simulations using realistic process parameters, where the simulation provided both the optical emission and the particle flux for each given process regime.

The following trends are observed: The points in the low pressure regime (circles) are on a straight line indicating complete proportionality between the emission ratio and the flux ratio. Therefore, the intersection between the line through these points and the vertical line that indicates the threshold of the emission ratio for crystalline growth can be used to convert the emission ratio threshold into a flux ratio threshold, that is, to draw the horizontal line.

For series in which the power or the dilution is varied, Figure 4.5 shows how, by variation of the hydrogen dilution or the power, the ratios of the two criteria for crystalline growth are varied more or less proportionally, including the points in the high pressure regime. By an increase of the pressure, the regime moves along the curved paths towards the origin, where at the first stages of the pressure increase, the flux ratio increases, while the OES ratio decreases. If the pressure is increased even further, the behaviour of the criteria returns to be roughly proportional.

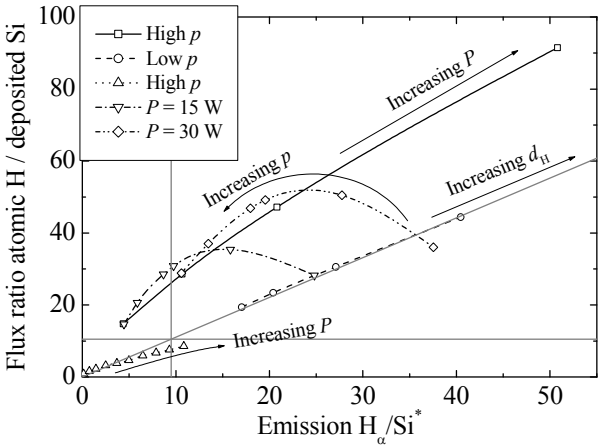

Figure 4.5: Trends in flux ratio vs. emission ratio for various deposition regimes.
(□) p = 8 mbar, d_e = 6 mm, f_{silane} = 1.2 sccm, $f_{hydrogen}$ = 100 sccm, P = 15 – 100 W;
(○) P = 15 W, p = 1.1 mbar, d_e = 6 mm, f_{silane} = 1.2 sccm, d_H = 25 – 200;
(△) p = 9 mbar, d_e = 6 mm, f_{silane} = 20 sccm, $f_{hydrogen}$ = 500 sccm, P = 20 – 200 W;
(▽) P = 15 W, d_e = 6 mm, f_{silane} = 1.2 sccm, $f_{hydrogen}$ = 100 sccm, p = 1.1 – 8 mbar;
(◇) P = 30 W, d_e = 6 mm, f_{silane} = 1.2 sccm, $f_{hydrogen}$ = 100 sccm, p = 1.1 – 8 mbar;
The gray lines indicate the emission ratio threshold for nc-Si:H growth from experiment (vertical), the low pressure regime for which emission and flux ratio are proportional and determined by dissociation reactions only (diagonal) and the flux ratio threshold inferred from the low pressure regime (diagonal).

The regime with high silane flow starts out along the lower slope, but when the power is increased, the OES ratio rises more quickly than the flux ratio. These observations can be understood as follows:

More power causes more hydrogen to be dissociated, especially when silane is already depleted, and more hydrogen atoms to reach the film. In this case both the flux ratio of hydrogen atoms to silicon species and the emission ratio of H_α to Si^* increase. If the dilution is increased, an increasing amount of hydrogen is dissociated compared to the silane dissociation, which has the same result on the flux and emission ratios.

Increase of the pressure yields a lower electron temperature (T_e) and a higher electron density (N_e) leading to more silane dissociation, which would cause both the flux ratio and the emission ratio to decrease. However, the increased pressure also results in an increase in gas phase reactions, decreasing mainly the contribution of the reactive SiH_2 radicals to the silicon species flux. The SiH_2 radicals react via the type of reactions given in Equation 4.5 and Equation 4.6 to higher silane related species, which have a much lower deposition probability, resulting in lower silicon atom flux towards the electrodes. Thus the pressure

increase does cause the emission ratio to decrease, but the flux ratio decreases less, or may even increase.

At even higher pressures, a new but different proportionality between the flux and emission ratio is established, where the reactive silicon species are observed in the emission from dissociation reactions, but contribute very little to the flux of silicon to the electrodes.

The behaviour at high silane flow can be explained by the hydrogen abstraction reaction (Equation 4.4). In this regime an increasing fraction of the silicon species contributing to the flux to the electrodes is generated via the abstraction mechanism rather than via electron impact dissociation, when the power is increased. This fraction is therefore not monitored via the emission of the dissociation reactions. Therefore, in this regime the emission ratio increases faster than the flux ratio.

4.4 The correction factor between emission and flux ratios

4.4.1 Derivation of the correction factor

In the previous section it was shown with the use of computer simulation that there is no constant proportionality factor between the emission ratio H_α/Si^* and the flux ratio of hydrogen atoms to silicon species in varying deposition regimes. Therefore, the transition from a-Si:H to nc-Si:H does not occur at a fixed value of the H_α/Si^* emission ratio. To be able to use the simple technique of OES for the prediction of the transition from a-Si:H to nc-Si:H via the H_α/Si^* emission ratio, a regime-dependent correction factor is required to relate the measured H_α/Si^* emission ratio to the true flux ratio of atomic hydrogen to silicon species.

Using a few basic assumptions about the deposition conditions it can be shown that the correction factor depends only on a limited number of measurable process parameters. One assumption is that the hydrogen flow is much higher than the silane flow, which is typical for a process regime aimed at nc-Si:H growth, and therefore the hydrogen flow dominates the residence time of the gas mixture. Another assumption is that the inter-electrode spacing, d_e, is much smaller than the electrode size, so that deposition on the reactor wall can be neglected. Further more, a fully symmetrical reactor is assumed, so that the field distribution is symmetrical as well, and there is no difference between the particle flux at

the powered electrode and the flux at the substrate. The emission observed by the spectrometer originates directly from the electron impact dissociation reactions:

$$\frac{I_{\mathrm{rad}}^{\mathrm{H}_\alpha}}{I_{\mathrm{rad}}^{\mathrm{Si}^*}} = \frac{K_{\mathrm{rad}}^{\mathrm{H}_\alpha} N_{\mathrm{e}} N_{\mathrm{H}_2}}{K_{\mathrm{rad}}^{\mathrm{Si}^*} N_{\mathrm{e}} N_{\mathrm{SiH}_4}} = \frac{N_{\mathrm{H}_2} K_{\mathrm{rad}}^{\mathrm{H}_\alpha}}{N_{\mathrm{SiH}_4} K_{\mathrm{rad}}^{\mathrm{Si}^*}} \tag{4.7}$$

Where I_{rad} indicates the amount of generated photons per unit volume per second, and N denotes the concentration of electrons (e) and silane (SiH_4) and hydrogen (H_2) molecules. The rate constants, K_{rad}, for the indicated emission of Si^* and H_α, depend on the electron temperature (T_e). The T_e-dependence of these rate constants will be discussed later on in the derivation.

The flux ratios are slightly more complicated, since the flux of silicon species can originate from both electron impact dissociation and hydrogen abstraction:

$$\frac{\Gamma^{\mathrm{H}}}{\Gamma^{\mathrm{Si}}} = \frac{\Gamma^{\mathrm{H}}}{\Gamma_{\mathrm{dis}}^{\mathrm{Si}} + \Gamma_{\mathrm{abs}}^{\mathrm{Si}}} \tag{4.8}$$

Γ is used for volumetric generation of the species that will result in a flux at the electrodes. In this way no information on the reactor properties is necessary in this derivation. However, it should be kept in mind throughout this derivation that the units of this Γ are $cm^{-3} \cdot s^{-1}$. To arrive at a real flux quantity, $d_e\Gamma/2$ has to be evaluated.

Atomic hydrogen results from the electron impact dissociation reaction of molecular hydrogen and every dissociation event yields two hydrogen atoms,

$$\Gamma^{H} = 2K_{\mathrm{dis}}^{\mathrm{H}_2} N_{\mathrm{e}} N_{\mathrm{H}_2} \tag{4.9}$$

However the origin of the flux of silicon species towards the walls is more complicated. There is a contribution from the electron impact dissociation of silane; From photolysis experiments it was reported that dissociation of silane results in SiH_2 and SiH_3 with quantum yields of 0.83 and 0.17 respectively [64]. Experimental results in a plasma environment confirm that SiH_2 is the dominant product of electron impact dissociation [73].

The SiH_3 radicals have a low reaction probability at the substrate. Most of them are reflected, but since they also hardly react in the volume, all of them will eventually react with the surface. Then, two processes are possible: abstraction of an H atom, creating a dangling bond, and transformation into a silane molecule, or deposition. In this way, approximately 35% of the SiH_3 is deposited and 65% returns as SiH_4 [74, 75]. It is not likely that all SiH_2 is deposited since this very reactive radical is rapidly lost in gas phase reactions and, moreover, a large contribution of SiH_2 to the growth of the film is in contradiction with a surface diffusion model for the formation of nc-Si:H [57]. For these reasons, at this point an empirical average deposition probability ξ for all silane dissociation products is introduced:

$$\Gamma_{\mathrm{dis}}^{\mathrm{Si}} = \xi K_{\mathrm{dis}}^{\mathrm{SiH_4}} N_{\mathrm{e}} N_{\mathrm{SiH_4}} \tag{4.10}$$

On top of generation of growth precursors from electron impact dissociation, the hydrogen abstraction mechanism (Equation 4.4) creates the growth precursor SiH_3. The deposition via this mechanism is proportional to the atomic hydrogen concentration:

$$\Gamma_{\mathrm{abs}}^{\mathrm{Si}} = 0.35 K_{\mathrm{abs}} N_{\mathrm{H}} N_{\mathrm{SiH_4}} \tag{4.11}$$

The concentration of atomic hydrogen N_{H} depends on the residence time of atomic hydrogen in the reactor, which is determined by diffusion to the electrodes rather than outflow to the pump system. That is the case even when the diffusion length, on a timescale of the residence time, has the same order of magnitude as the electrode diameter, which is already an extreme deposition regime (see also Subsection 5.2.1, taking into account that the diffusion constant of atomic hydrogen in H_2 is even higher than that of argon in H_2), considering the assumption of a small d_{e} compared to the electrode area.

If a general parabolic density profile (Figure 4.6) for the generated atomic hydrogen is assumed, $N_{\mathrm{H}}(x)=N_{\mathrm{H},0}(1-x^2/L^2)$, the flux to the walls and the density of atomic hydrogen are related as follows:

$$\Gamma^{\mathrm{H}} \frac{d_{\mathrm{e}}}{2} = -D_{\mathrm{H,H_2}} \left.\frac{dN(x)}{dx}\right|_{x=L} = \frac{2D_{\mathrm{H,H_2}} N_{\mathrm{H,0}}}{L^2} x\Big|_{x=L} = \frac{2D_{\mathrm{H,H_2}} N_{\mathrm{H,0}}}{L} \qquad (4.12)$$

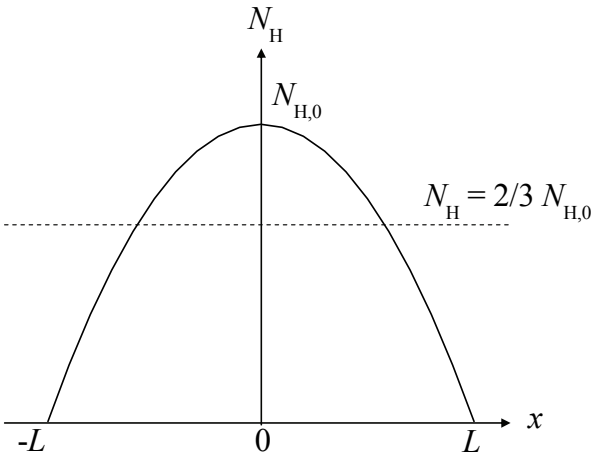

Figure 4.6: The assumed parabolic density profile for the atomic hydrogen.

Now setting $L = d_e/2$, and considering the fact that for a parabolic density distribution the average atomic hydrogen concentration N_H is given by $N_H = ⅔N_{H,0}$, where $N_{H,0}$ is the peak hydrogen concentration, the relation between the hydrogen flux to the walls and the average atomic hydrogen concentration is:

$$N_{\mathrm{H}} = \frac{\Gamma^{\mathrm{H}} d_{\mathrm{e}}^2}{12 D_{\mathrm{H,H_2}}} \qquad (4.13)$$

The product of the diffusion coefficient of H in H_2 and the pressure is a constant:

$$D_{\mathrm{H,H_2}}\, p = 19.7 m^2 s^{-1} \mathrm{Pa} \qquad (4.14)$$

and the pressure p can be written in terms of the molecular hydrogen concentration and the gas temperature T_{gas} as

$$p = N_{\mathrm{H_2}} k T_{\mathrm{gas}} \qquad (4.15)$$

Where k is Boltzmann's constant. Using Equation 4.9, the density of atomic hydrogen can be written as

$$N_{\mathrm{H}} = \frac{1}{12}\frac{N_{\mathrm{e}} d_{\mathrm{e}}^2 N_{\mathrm{H}_2}^2 K_{\mathrm{dis}}^{\mathrm{H}_2} kT_{\mathrm{gas}}}{19.7} = 8.4{\cdot}10^{-3} N_{\mathrm{e}} d_{\mathrm{e}}^2 N_{\mathrm{H}_2}^2 K_{\mathrm{dis}}^{\mathrm{H}_2} kT_{\mathrm{gas}} \qquad (4.16)$$

The correction factor that converts the emission ratio into the flux ratio can now be derived. With

$$R_{\mathrm{dis}} = \frac{K_{\mathrm{dis}}^{\mathrm{SiH}_4}}{K_{\mathrm{dis}}^{\mathrm{H}_2}}, \qquad (4.17)$$

$$R_{\mathrm{rad}} = \frac{K_{\mathrm{rad}}^{\mathrm{Si}^*}}{K_{\mathrm{rad}}^{\mathrm{H}_\alpha}}, \qquad (4.18)$$

and

$$K_{\mathrm{abs}} = 1.2{\cdot}10^{-18}\,\mathrm{m^3 s^{-1}} \text{ [69]}, \qquad (4.19)$$

we arrive at

$$\frac{\Gamma^{\mathrm{H}}}{\Gamma^{\mathrm{Si}}} = \frac{I_{\mathrm{rad}}^{\mathrm{H}_\alpha}}{I_{\mathrm{rad}}^{\mathrm{Si}^*}} \frac{R_{\mathrm{rad}}}{R_{\mathrm{dis}}\xi + 1.8{\cdot}10^{-21}(pd_e)^2 / kT_{\mathrm{gas}}}. \qquad (4.20)$$

Equation 4.20 shows how the flux ratio and the emission ratio are different by a factor that depends on the product $(pd_{\mathrm{e}})^2/kT_{\mathrm{gas}}$ and on the ratios of the rate constants for emission, R_{rad}, and electron-impact dissociation, R_{dis}.

4.4.2 The role of the electron temperature in the correction factor

The rate constants depend on T_e. However, the *ratio* of the rate constants for dissociation, R_{dis}, is approximately constant for T_e in the range of 3 - 8 eV, as can be seen from Figure 4.7. The ratio of the rate constants for the emission, R_{rad}, depends more strongly on T_e so that an indicator for the electron temperature is necessary to find a valid correction to the emission ratio.

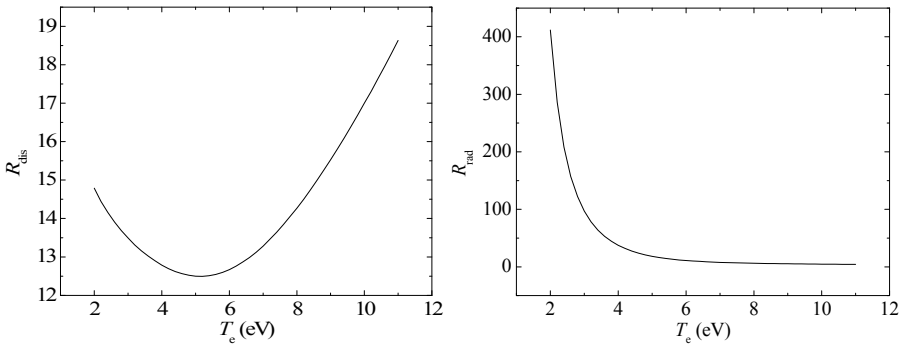

Figure 4.7: The ratios of rate constants for dissociation (left) and radiation (right) against the electron temperature derived from the rate constants used in the 1-D simulation.

A suitable candidate for such an indicator of the electron temperature is the emission ratio H_β/H_α [76]. The ratio of this emission is equal to the ratio of the rate constants:

$$\frac{I_{rad}^{H_\beta}}{I_{rad}^{H_\alpha}} = \frac{K_{rad}^{H_\beta} N_e N_{H_2}}{K_{rad}^{H_\alpha} N_e N_{H_2}} = \frac{K_{rad}^{H_\beta}}{K_{rad}^{H_\alpha}} = R_{\beta\alpha} \tag{4.21}$$

It is not necessary to exactly find T_e; a monotonous dependence of R_{rad} on $R_{\beta\alpha}$ is sufficient. The extended computer simulation includes also H_β emission, so a series with varying T_e was simulated to find the relation between the observable $R_{\beta\alpha}$ and the needed R_{rad}. This relation is presented in Figure 4.8. The indicated fit yields the following relation between R_{rad} and $R_{\beta\alpha}$:

$$R_{rad}(R_{\beta\alpha}) = 2.4 \cdot 10^{-7} R_{\beta\alpha}^{-6.9} \tag{4.22}$$

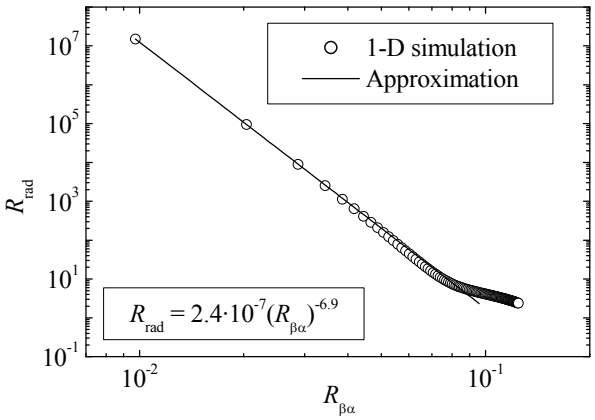

Figure 4.8: The ratio of the rate constants for radiation of Si^* and H_α against the ratio of the rate constants for radiation of H_α and H_β from a simulation series of varying T_e.

In the graph another relation can be identified for $R_{\beta\alpha}$-values above 0.1, but this relation is not relevant since for all deposition regimes presented in Figure 4.5 the values of $R_{\beta\alpha}$ are in the range between 0.04 and 0.08.

4.4.3 Application of the correction factor in simulation and experiment

With the incorporation of a measurable quantity ($R_{\beta\alpha}$) to determine the T_e-dependent R_{rad}, the derived correction factor can be tested for the various simulated process regimes from Figure 4.5. Equation 4.20 can be rewritten as follows:

$$R_{\mathrm{rad}} \frac{I_{\mathrm{rad}}^{\mathrm{H}_\alpha}}{I_{\mathrm{rad}}^{\mathrm{Si}^*}} \Big/ \frac{\Gamma^{\mathrm{H}}}{\Gamma^{\mathrm{Si}}} = a\left\{(pd_e)^2 / kT_{\mathrm{gas}}\right\} + b \tag{4.23}$$

This suggests a linear relationship between

$$\frac{I_{\mathrm{rad}}^{\mathrm{H}_\alpha}}{I_{\mathrm{rad}}^{\mathrm{Si}^*}} \Big/ \frac{\Gamma^{\mathrm{H}}}{\Gamma^{\mathrm{Si}}} R_{\mathrm{rad}}$$

and $(pd_e)^2/kT_{gas}$, where b in Equation 4.23 equals $\xi \cdot R_{dis}$ and a should be close to the estimated value of $1.8 \cdot 10^{-21}$ in Equation 4.20. The plotting and fitting according to Equation

4.23 is shown in Figure 4.9. Most of the simulation points in this figure constitute a good linear relationship, yielding $a = 1.9 \cdot 10^{-21} \pm 2 \cdot 10^{-22}$ and $b = 5.5 \pm 1.9$. The deviation of the points indicated with (□) is very large, which can be explained from the low silane flow in combination with high power. The discharge has to run practically on hydrogen ionisation in that case, which requires a much higher T_e. Probably the approximation of a constant R_{dis} is not valid here.

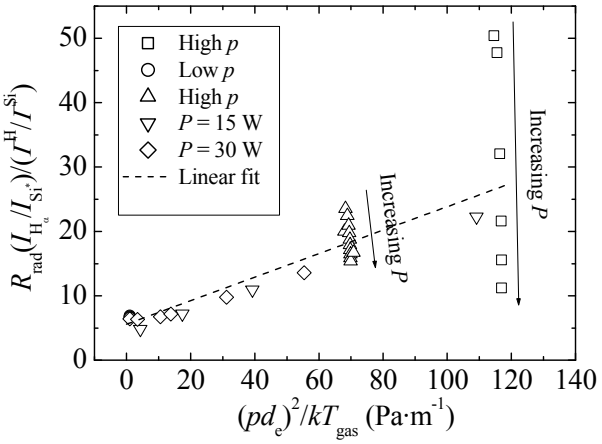

Figure 4.9: Correction factor to calculate the actual flux ratio of atomic hydrogen to silicon species from the emission ratio of H_α and Si^*, as obtained from simulation. The straight line represents the fit of the model derived in this chapter to the data from the simulation:
(□) p = 8 mbar, d_e = 6 mm, f_{silane} = 1.2 sccm, $f_{hydrogen}$ = 100 sccm, P = 15 – 100 W;
(○) P = 15 W, p = 1.1 mbar, d_e = 6 mm, f_{silane} = 1.2 sccm, d_H = 25 – 200;
(△) p = 9 mbar, d_e = 6 mm, f_{silane} = 20 sccm, $f_{hydrogen}$ = 500 sccm, P = 20 – 200 W;
(▽) P = 15 W, d_e = 6 mm, f_{silane} = 1.2 sccm, $f_{hydrogen}$ = 100 sccm, p = 1.1 – 8 mbar;
(◇) P = 30 W, d_e = 6 mm, f_{silane} = 1.2 sccm, $f_{hydrogen}$ = 100 sccm, p = 1.1 – 8 mbar.

The values obtained for a and b along with the relation between R_{rad} and $R_{\beta\alpha}$ enable one to use Equation 4.20 in combination with the experimentally determined p, T_{gas}, d_e and $R_{\beta\alpha}$, to correct the observed emission ratio between H_α and Si^* into the actual flux ratio of atomic hydrogen to silicon species arriving at the electrode. For calibration, a single series of depositions should reveal the flux ratio at which the transition to nc-Si:H growth sets in.

4.5 Conclusions

In this chapter it was demonstrated that there is a good agreement between the used computer simulation of deposition plasmas in various process regimes and the experiment.

The optical emission is predicted well both in higher and lower power conditions. For lower power conditions the deposition rate is also predicted well. At power densities above 0.5 W/cm^2 a discrepancy occurs between the simulated and the experimental deposition rate.

In order to predict the transition from the a-Si:H to the nc-Si:H growth regime, it is not sufficient to observe the optical emission ratio H_α/Si^* alone; hydrogen abstraction and variations in the electron temperature cause this emission ratio to deviate from the flux ratio of atomic hydrogen to silicon species at the electrodes, which actually determines the transition from a-Si:H to nc-Si:H growth.

A simple correction factor can correct the observed emission ratio for these deviations so that it reflects the flux ratio much more accurately for the various most commonly used deposition regimes. The correction factor is based on in situ measurable quantities only, so that the flux ratio can immediately be used to tailor the deposition conditions with respect to the threshold for nc-Si:H growth. This makes this procedure very suitable for industrial production processes for thin film a-Si:H and nc-Si:H solar cells. The state of the deposition regime can be controlled throughout the deposition phase to be in the optimal condition close to, but on the proper side (a-Si:H or nc-Si:H) of the transition.

Chapter 5

Challenges for high-deposition rate growth of nanocrystalline silicon

Abstract

High deposition rate growth of thin film nanocrystalline silicon with Very High Frequency Chemical Vapour Deposition (VHF PECVD) poses a number of challenges compared to low deposition rate regimes. The regime of high deposition rate can be accompanied by a very high degree of depletion of the silane source gas. Control of the crystalline ratio by hydrogen dilution is not possible anymore; instead the crystalline ratio has to be tuned by variation of the degree of depletion via the power or the silane flow. The depletion of the source gas was observed via the variation of the deposition rate with the flow rate, and via the optical emission from the discharge. The behaviour of the optical emission was explained in terms of a qualitative model. The deposition rate increased stronger with increasing VHF power than the optical emission due to silane dissociation suggested, indicating a large role for the hydrogen abstraction mechanism in creating growth precursors in the gas phase.

A deep depletion can give rise to back diffusion of silane into the discharge zone. The length scales for diffusion in the discharges for the high (4.5 nm/s) and low (0.5 nm/s) deposition rate regimes were calculated, as well as the stabilisation times for back diffusion. In the high deposition rate regime, back diffusion influences a thicker part of the deposited film. This can partially explain the rather thick (>200 nm) amorphous incubation layer observed in high deposition rate nanocrystalline film deposition. The amorphous incubation layer could be substantially reduced (to <<100 nm) by a hydrogen plasma start prior to the film deposition. The hydrogen plasma start resulted in a smooth surface indicating a high nucleation density. Further manipulation of the crystalline ratio can be achieved through silane profiling.

5.1 Tuning the crystalline ratio

5.1.1 Using VHF power variation for crystalline ratio adjustment

In conventional regimes for the deposition of hydrogenated nanocrystalline silicon (nc-Si:H), with a pressure << 1 mbar and a power << 1 W/cm^2, the crystalline ratio could be tuned using variation of the flow of hydrogen towards the reactor, effectively changing the hydrogen concentration relative to that of silane. The main reason that this method does not work in deposition regimes aimed at high deposition rates, is that such regimes are characterized by a high power density, which enables an efficient use of the silane source gas. As long as the silane remains largely depleted and most of its derived products are deposited within the residence time, variation in the hydrogen flow has no effect on the gas composition – a higher inflow of hydrogen will just result in a larger outflow of hydrogen, and similar reasoning holds for a decrease in the hydrogen flow. In other words, at a high level of silane depletion, there is a significant difference between the inflow ratio of hydrogen to silane, and the actual ratio of the hydrogen and silane concentrations in the reactor. The latter ratio is influenced by the rates of the various dissociation, abstraction and polymerisation mechanisms.

Evidence for the high degree of depletion and deposition efficiency was found in an experiment where the flows were reduced by a factor of 2, compared to the standard regime for high deposition rate nc-Si:H material. The standard flows were 20 sccm silane and 300 sccm hydrogen, and these flows were reduced to 10 and 150 sccm, respectively, using the same delivered VHF power of 350 W. The deposition rate went down by 43%, from 3.8 nm/s to 2.1 nm/s, which indicates a high level of depletion in the original regime.

When such a high level of depletion is present, methods for the control of the crystalline ratio other than hydrogen dilution variation have to be applied. In section 4.2.1 it was already put forward that the important plasma properties that determine the crystalline growth are the silicon species flux and the atomic hydrogen flux. Rather than tuning the hydrogen flow, the keys to control are therefore now to be found in the degree of depletion and the amount of dissociation by variation of the VHF power [56], or by variation of the silane flow.

5.1.2 Optical Emission Spectroscopy in the high power, high pressure regime

A series of layers with a thickness of 500 nm was deposited in the ASTER deposition system on Corning Eagle 2000 glass substrates using VHF power variation under a fixed hydrogen dilution as a means of crystalline ratio control, as was suggested above. The series were deposited around the transition regime from the amorphous to the nanocrystalline phase. The intensities of the H_α and Si^* lines from Optical Emission Spectroscopy (OES), which were recorded during this series, are presented in Figure 5.1.

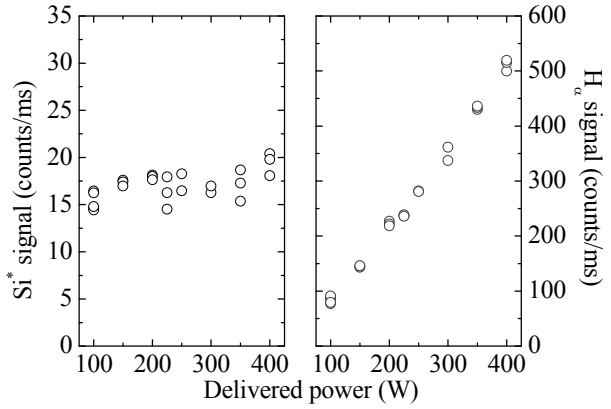

Figure 5.1: Delivered power dependence of Si^* and H_α emission intensity vs. delivered power. p = 9 mbar, d_e = 6 mm, f_{silane} = 20 sccm, $f_{hydrogen}$ = 500 sccm.

With increasing delivered VHF-power to the reactor an increase in the H_α emission, but an almost constant Si^* emission is observed. Apparently the electron impact dissociation of silane is constant in the range of applied powers and the dissociation of atomic hydrogen develops with increasing delivered power. This again points to a high degree of depletion of the silane source gas. In dilution-controlled low pressure, low power deposition regimes, the transition to crystalline growth generally occurs beyond a certain threshold in the H_α/Si^* ratio, as was stated in section 4.2.1. This principle turns out to be valid in this power-controlled high pressure, high power regime as well (see Figure 5.2).

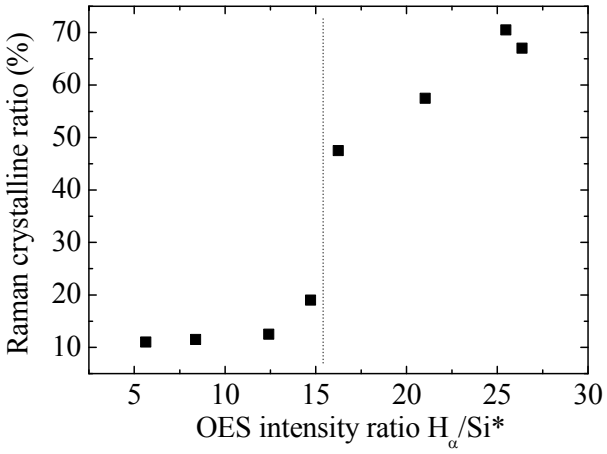

Figure 5.2: Raman crystalline ratio, obtained from the film side of the samples, vs. OES H_α/Si* intensity ratio for 500 nm films on glass. The dotted line indicates the threshold for nanocrystalline growth. p = 9 mbar, d_e = 6 mm, f_{silane} = 20 sccm, $f_{hydrogen}$ = 500 sccm, P = 100 – 400 W.

However, the threshold value observed in this case can not be taken to be a universal one, not even for this very reactor geometry, since this regime of high depletion makes it difficult to establish a workable conversion factor between the physical fluxes present in the reactor and the measured OES intensities.

5.1.3 A simple depletion model for the Optical Emission Spectroscopy

The optical emission results presented above can be understood in terms of the simple model that was introduced in section 4.4, if the concept of silane depletion is introduced in this model. Keeping in mind that the assumption of a much higher hydrogen concentration compared to the silane concentration remains valid, the hydrogen concentration is determined only by the pressure p and temperature T:

$$N_{H_2} = \frac{p}{kT} \tag{5.1}$$

Where k is Boltzmann's constant and N is the steady-state concentration in the plasma. The residence time is

$$\tau_{\mathrm{res}} = \frac{N_{\mathrm{H_2}}}{S_{\mathrm{H_2}}}, \tag{5.2}$$

where S denotes the rate of change of concentration because of the inflow of gas into the reactor. Under the assumption of equal pump speeds for silane and hydrogen, which is justifiable for the used turbomolecular pump, and a much higher concentration of hydrogen compared to silane the same τ_{res} holds for silane as well, so that the rate of silane being evacuated by the pump system becomes:

$$Q_{\mathrm{pump}}^{\mathrm{SiH_4}} = \frac{N_{\mathrm{SiH_4}}}{\tau_{\mathrm{res}}} \tag{5.3}$$

Q has the same units as S. The silane concentration can be determined using the measured deposition rate. There should be a balance between the rate of silicon entering in the form of silane, and the rate of silane molecules exiting the active volume either through the pump system or by being deposited on the electrodes:

$$S_{\mathrm{SiH_4}} = Q_{\mathrm{pump}}^{\mathrm{SiH_4}} + \Gamma_{\mathrm{dis}}^{\mathrm{SiH_4}} + \Gamma_{\mathrm{abs}}^{\mathrm{SiH_4}} \tag{5.4}$$

Just as in Section 4.4, Γ represents a rate of change of the concentration due to dissociation and abstraction reactions. Polymerisation reactions are not taken into account in this simple model. Substituting Equations 4.10, 4.11 and 5.3,

$$S_{\mathrm{SiH_4}} = \frac{N_{SiH_4}}{\tau_{\mathrm{res}}} + \xi K_{dis}^{SiH_4} N_e N_{SiH_4} + 0.35 K_{\mathrm{abs}} N_{\mathrm{H}} N_{\mathrm{SiH_4}} \tag{5.5}$$

Rearranging and using the expression for the atomic hydrogen density from Equation 4.16 gives:

$$S_{\mathrm{SiH_4}} = N_{SiH_4}\left[\frac{1}{\tau_{\mathrm{res}}} + N_{\mathrm{e}}\left(\xi K_{dis}^{SiH_4} + 2.9\cdot 10^{-3} K_{\mathrm{abs}} K_{\mathrm{dis}}^{\mathrm{H_2}} N_{\mathrm{H_2}}^2 d_{\mathrm{e}}^2 k T_{\mathrm{gas}}\right)\right] \tag{5.6}$$

In this way one arrives at a relation between the silane density and the electron density, where the latter governs the depletion of the source gas:

$$N_{SiH_4} = \frac{S_{\mathrm{SiH_4}}}{1/\tau_{\mathrm{res}} + N_{\mathrm{e}}\left(\xi K_{dis}^{SiH_4} + 2.9\cdot10^{-3} K_{\mathrm{abs}} K_{\mathrm{dis}}^{\mathrm{H_2}} N_{\mathrm{H_2}}^2 d_{\mathrm{e}}^2 kT_{\mathrm{gas}}\right)} \tag{5.7}$$

This silane density as a function of the electron density can be used to investigate the effect of electron density on optical emission in regimes of high depletion. From equation 4.7, separate equations for the generation of the optical emission peaks H_α and Si^* can be formulated:

$$I_{\mathrm{rad}}^{\mathrm{H}_\alpha} = K_{\mathrm{rad}}^{\mathrm{H}_\alpha} N_{\mathrm{e}} N_{\mathrm{H_2}} \tag{5.8}$$

$$I_{\mathrm{rad}}^{\mathrm{Si}^*} = K_{\mathrm{rad}}^{\mathrm{Si}^*} N_{\mathrm{e}} N_{\mathrm{SiH_4}} \tag{5.9}$$

In Equation 5.9 the expression for the silane concentration from Equation 5.7 can be substituted.

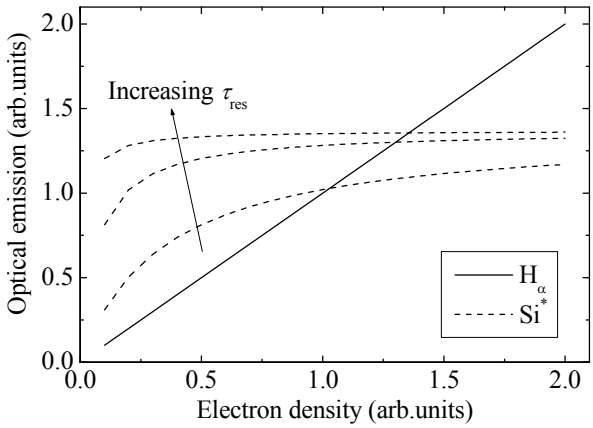

Figure 5.3: Sketch of the behaviour of the optical emission based on the simple model of Section 4.4 extended in this chapter to incorporate the silane depletion.

Again without explicitly accounting for the electron temperature dependence of the various rate constants for dissociation, a sketch of the emission is constructed in Figure 5.3.
In this simple sketch the same behaviour is observed as in the experimental results in Figure 5.1: For a certain range of the electron density, which is assumed to be more or less proportional to the delivered power, the Si^* emission is roughly constant, whereas the H_α intensity increases linearly with the electron density. The experimentally observed behaviour of the Si^*, being constant even when the power is doubled, is therefore well explained from the perspective of depletion. Therefore, this behaviour is another indicator for the depletion of the silane source gas.

5.1.4 Deposition rate

Although it has been reported that the deposition rate in silane plasmas often follows the trend of the Si^* intensity from OES [51], here a different situation was encountered: The deposition rate increased with increasing power, even though the Si^* intensity saturated. This is illustrated in Figure 5.4, showing the deposition rate and the Si^* emission as a function of the delivered power. Since at higher delivered power the material developed a considerable crystalline ratio and an increased surface roughness, the thickness determination from optical methods became unreliable.

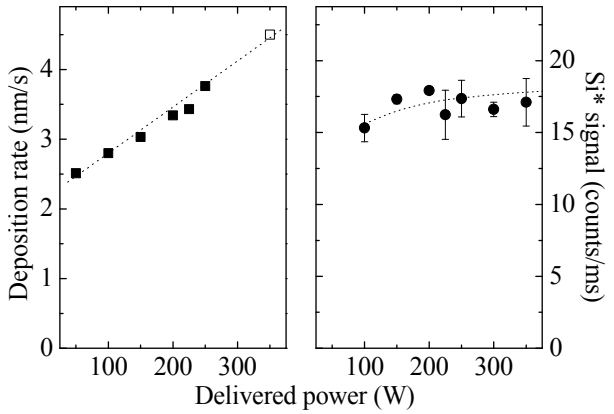

Figure 5.4: Deposition rate (r_d) and Si^* emission for a series of layers deposited in the high power, high pressure regime. The r_d-data are a compilation of optical measurements (■) and a measurement of a thicker layer using surface profilometry (□). The dotted line in the left figure is a guide to the eye. The dotted line in the right figure is a fit of the form $aP / (b + cP)$, where P is the delivered power, in line with the model in Subsection 5.1.3.

Therefore, the point at 350 W was taken from the measurement of a 1000-nm sample using a profilometer. The guide to the eye for the emission data is intentionally curved to illustrate the resemblance with the sketched behaviour of the Si^* emission in Figure 5.3. An explanation for the increasing deposition rate with power, while the Si^* emission saturates, is found in the gas phase reactions that are likely to occur in high pressure deposition regimes. In particular the hydrogen abstraction mechanism [77],

$$SiH_4 + H \rightarrow SiH_3 + H_2\,, \tag{5.10}$$

can be responsible for the formation of additional SiH_3 radicals. The result is an increased deposition rate, without an increase of the Si^* optical emission. This mechanism cannot be explained by the simple model that relates the depletion of silane to the experimentally observed behaviour of the optical emission, because the hydrogen abstraction is in this simple model proportional to the silane concentration, in the same way as the dissociation of silane itself. This clearly demonstrates the limits of this simple model. Since the electron temperature is not taken into account, the simple model cannot predict the effect of the shift in the electron temperature to higher values as the power is increased, which in turn facilitates the dissociation of hydrogen at the cost of direct silane dissociation. Furthermore, polymerisation reactions of dissociation products with silane molecules can cause a single dissociation event of a silane molecule to result in multiple deposited silicon atoms, which further increases the discrepancy between Si^* emission and deposition rate.

5.2 Time and length scales for silane back diffusion

5.2.1 Diffusion length for back diffusing silane

A significant difference between conventional deposition regimes and high deposition rate conditions is the degree of depletion of the silane source gas. This is intentionally done, to arrive at an efficient use of the gas and prevent clustering reactions with SiH_4 molecules as described in 3.2.3. The drawback of this high depletion regime is that it introduces inhomogeneities of the gas composition in the reactor, both in space and in time.

One of the time dependent effects is the back diffusion of silane from the passive reactor volume into the active volume, i.e. between the electrodes [78]. This causes, from the

moment of switching on the VHF power, a stabilisation period in the order of tens of seconds, depending on process parameters such as pressure and flow, and the geometry of the reactor. To see if the back diffusion of silane into the plasma region is plausible, it should be investigated how the diffusion length relates to the typical reactor dimensions during a time interval equal to the residence time in the plasma zone, τ_p. The residence time for the gas in the plasma zone of the reactor, with a volume, V, of 100 cm^3, a pressure p of 9 mbar (p_0 = 1 bar) and a total gas flow, S, of 320 sccm, is:

$$\tau_p = 60\frac{V}{S}\frac{p}{p_0} = 0.19\,\mathrm{s} \tag{5.11}$$

The diffusion coefficient for argon in hydrogen at 100°C and atmospheric pressure is 1.2 cm^{2}s^{-1} [79]. For silane the diffusion coefficient will not be significantly different. The diffusion constant is inversely proportional to the pressure; hence the diffusion constant for argon in hydrogen at 9 mbar is:

$$D = D_{0,\mathrm{Ar-H_2}}\frac{p}{p_0} = 130\,\mathrm{cm^2 s^{-1}} \tag{5.12}$$

The diffusion length L_d in a time interval τ_p is then:

$$L_d = 2\sqrt{Dt} = 2\sqrt{D\tau_p} = 10\,\mathrm{cm} \tag{5.13}$$

This value of L_d is very comparable to the lateral dimensions of the active area of the reactor, which has a diameter of 15 cm. This shows that in the described discharge regime, the (back) diffusion length of silane from the inactive region of the reactor into the discharge region, at the beginning of the deposition, provides a realistic explanation for the observed amorphous incubation layer in the films. For comparison, the diffusion length in the growth regime for performance-optimized nc-Si:H is roughly twice as large, where the difference in residence time has also been taken into account. That means that the back diffusion mechanism plays a role here as well, but the effect will at least be more uniform

along the lateral dimension because the diffusion length is larger, compared to the electrode diameter, than in the high r_d case.

5.2.2 The stabilisation time for the back diffusion of silane

The timescale for the composition stabilisation of the background gas mixture in the inactive region of the reaction chamber was estimated by calculation of the rate of change of the silane fraction in this gas mixture. To avoid unnecessary complexity, in this derivation only the inactive region was considered. Furthermore, the situation was simplified by assuming that all silicon species that were not deposited contribute to the background gas in the inactive region in the form of silane. The used symbols for the rates of concentration change are indicated in Figure 5.5.

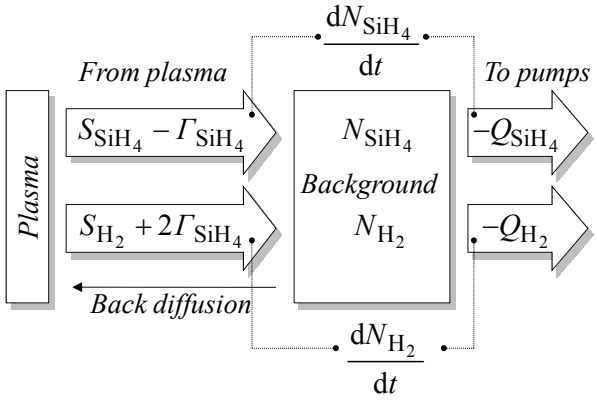

Figure 5.5: Visualization of the rates of change of the hydrogen and silane concentrations in the background gas.

The supply of silane to the inactive region is then given by the difference between the silane inflow (S) and the silane used in the deposition (Γ). A fraction of the silane in the inactive region is pumped away (Q).

$$\frac{dN_{SiH_4}}{dt} = \left(S_{SiH_4} - \Gamma_{SiH_4}\right) + Q_{SiH_4} \tag{5.14}$$

The supply of hydrogen to the inactive region is the sum of the inflow of hydrogen and the extra hydrogen (two hydrogen molecules per deposited silane molecule) that results from the deposition of silane.

$$\frac{\mathrm{d}N_{\mathrm{H_2}}}{\mathrm{d}t} = \left(S_{\mathrm{H_2}} + 2\Gamma_{\mathrm{SiH_4}}\right) + Q_{\mathrm{H_2}} \tag{5.15}$$

Assuming that the residual gas from the plasma region and the background gas are sufficiently mixed on exit through the pump, the concentration change rate, Q, corresponding to silane that leaves the reactor through the pump, is the product of the actual silane fraction in the background gas and the total rate of change of the concentration due to gas leaving the reactor.

$$Q_{\mathrm{SiH_4}} = \frac{N_{\mathrm{SiH_4}}}{N_{\mathrm{SiH_4}} + N_{\mathrm{H_2}}}\left(Q_{\mathrm{SiH_4}} + Q_{\mathrm{H_2}}\right) \tag{5.16}$$

Because the pressure is constant, there has to be a balance between gas flowing into the inactive region and gas being pumped away:

$$\frac{\mathrm{d}\left(N_{\mathrm{SiH_4}} + N_{\mathrm{H_2}}\right)}{\mathrm{d}t} = \left(S_{\mathrm{SiH_4}} + S_{\mathrm{H_2}} + \Gamma_{\mathrm{SiH_4}}\right) + \left(Q_{\mathrm{SiH_4}} + Q_{\mathrm{H_2}}\right) = 0 \tag{5.17}$$

$$Q_{\mathrm{SiH_4}} + Q_{\mathrm{H_2}} = -\left(S_{\mathrm{SiH_4}} + S_{\mathrm{H_2}} + \Gamma_{\mathrm{SiH_4}}\right) \tag{5.18}$$

This balance can be used to relate the total rate of change due to gas inflow to the total rate of change due to gas being pumped away, and this latter part is known via the deposition rate and the applied flows to the reactor. Substituting Equation 5.18 in Equation 5.16 gives:

$$Q_{\mathrm{SiH_4}} = -N_{\mathrm{SiH_4}}\frac{S_{\mathrm{SiH_4}} + \Gamma_{\mathrm{SiH_4}} + S_{\mathrm{H_2}}}{N_{\mathrm{SiH_4}} + N_{\mathrm{H_2}}} = -\frac{N_{\mathrm{SiH_4}}}{\tau_{\mathrm{r}}} \tag{5.19}$$

In the last part the total concentration change due to inflow divided by the sum of all concentrations is recognized as the residence time for particles in the inactive region of the reactor, τ_r.

The rate of change of the silane concentration in the inactive region of the reactor can now be formulated:

$$\frac{dN_{SiH_4}}{dt} = \left(S_{SiH_4} - \Gamma_{SiH_4}\right) - \frac{N_{SiH_4}(t)}{\tau_r} \tag{5.20}$$

The solution to this differential equation can be written as

$$N_{SiH_4}(t) = (1 - e^{-t/\tau_r})(S_{SiH_4} - \Gamma_{SiH_4})\tau_r + N_{SiH_4,0}e^{-t/\tau_r} \tag{5.21}$$

This solution describes the transition from the original background gas mixture, before the plasma starts, to the stabilised mixture that is governed by the flows coming from the active plasma zone, after the plasma is started. These flows depend on the degree of depletion. An example calculation of the transition for three values of the net silane inflow is shown in Figure 5.6. For the last curve, the silane content in the inactive region decays to zero, since it is assumed that at this flow rate the silane is fully consumed in the deposition.

The time constant in the solution for the time dependence of the silane concentration in the inactive region is dependent mostly on the total flow, which will often be dominated by the hydrogen flow, the pressure and the reactor volume. Realistic values were used for the reactor volume, pressure and the gas flows, so that the estimated τ_r of 7 seconds is valid for the regime of high (4.5 nm/s) deposition rate. The estimated reactor residence time in the performance-optimized regime for state-of-the-art nc-Si:H is 15 seconds, although the deposition rate is ten times smaller (0.5 nm/s). Therefore a more significant thickness of the deposited film is affected by the back diffusion mechanism in the high deposition rate regime for nc-Si:H growth compared to the high quality, low deposition rate regime.

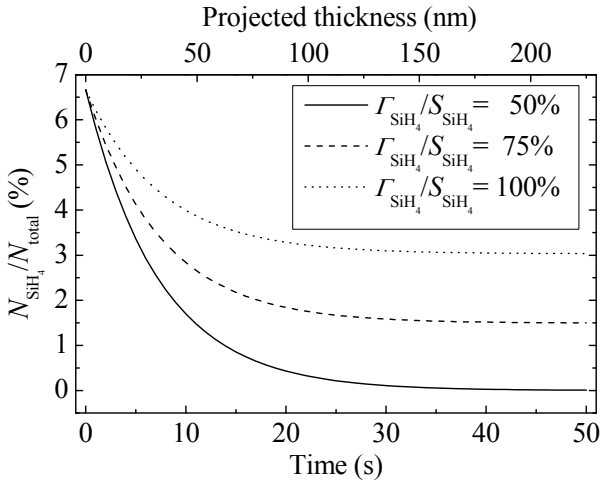

Figure 5.6: Calculation of the development of the fraction of silane in the inactive region, at the beginning of the deposition in the high r_d-regime. The flows of SiH_4 and H_2 were set to 20 sccm and 300 sccm, respectively and the initial fraction of silane was taken according to this flow mixture. The reactor volume was 4.6 litre and the pressure was 9 mbar. The different curves represent different degrees of depletion, as can be achieved by variation of the VHF power. The difference between the curves is the degree of depletion of the source gas as indicated.

This can be one of the reasons for the thick a-Si:H incubation layer, of at least 200 nm before nc-Si:H growth, which is observed in the high r_d regime, compared to less than 100 nm for the films deposited at low deposition rates. An additional explanation is the reduced time available for surface diffusion, in the regime of higher r_d, for silicon species to find a suitable nucleation site. This may be compensated by an increased ion energy flux towards the film, via an increase of the hydrogen flow, as was demonstrated in Chapter 3. The investigation and reduction of the incubation layer will be described in the next section.

5.3 Crystalline ratio development

5.3.1 Crystalline development in high and low deposition rate regimes

To investigate the incubation phase and the development of the crystalline phase in the high r_d material, and compare it to the conventional regime used to arrive at the highest quality material, multiple series of layers were deposited on a glass substrate with increasing layer thickness. To keep the initial conditions as close as possible to those employed in solar cell fabrication, the layers were always deposited on top of a 27 nm nc-Si:H seed layer, with a

crystalline ratio equal to the preceding doped layer applied in complete nc-Si:H solar cells. The Raman crystalline ratio (R_c) was determined using the method of Gaussian fitting as described in Subsection 2.3.2. The method of a-Si:H signal subtraction was not suitable for all samples in this experiment, because of the glass background signal present in the thin or highly crystalline samples. The results of the experiment for samples of both conventional and high deposition rates using standard deposition methods as described in Subsection 2.2.2, are presented in Figure 5.7.

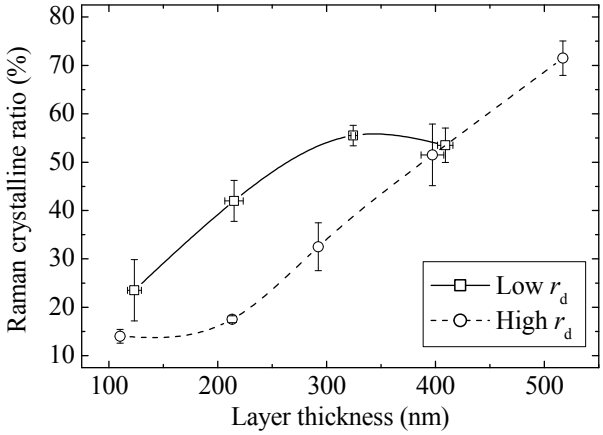

Figure 5.7: Evolution of the Raman crystalline ratio in layers of increasing thickness deposited on top of a nc-Si:H seed layer at low (0.5 nm/s) and high (4.5 nm/s) deposition rate.

The crystalline ratio in the conventional deposition regime at low r_d showed already a significant amount of crystallinity after 100 nm. The crystalline ratio saturated around 300 nm for this regime. The high r_d regime, however, exhibited a relatively thick incubation layer of about 200 nm, after which the crystalline ratio increased at the same rate as in the low r_d case. The fact that the crystalline ratio does not start at 0%, is explained by the nc-Si:H seed layer that was deposited before the films under investigation. Also contrary to the low r_d regime, in the fast growth regime the crystalline ratio did neither saturate after 300 nm, nor at the same ratio of the first regime.

5.3.2 Reducing the incubation thickness by hydrogen plasma start

In literature a frequently adopted method for the improvement of the homogeneity in the growth direction is profiling of the hydrogen dilution for both a-Si:H [80] and nc-Si:H [81] material. The use of power or silane flow profiling as a function of time has also been reported for the compensation of start-up effects [82]. Lateral power profiling has been used as well, to compensation for local differences in the degree of depletion, in order to achieve a homogeneous phase composition [83, 84]. Whereas these methods alter the deposition regime after the start of the actual deposition, it is also possible to change the conditions prior to the actual deposition, for example by tuning the background mixture on forehand in anticipation of the stabilised mixture during deposition [85]. A similar approach was applied here to reduce the incubation layer, with the exception that the plasma was started, but the silane flow and hence the deposition was postponed for a few seconds.

The likely cause of the relatively thick incubation layer in the high r_d regime was suggested in Section 5.2 to be the limited time for diffusion of the growth precursors on the growing surface because of the high flux of silicon species to the growing film under these circumstances, in combination with a long stabilisation time for back diffusing silane in to the plasma region. To overcome these problems, it was attempted to start with no silane flow at all, leaving only a hydrogen plasma for the first 5 seconds in the deposition process. After these first seconds of hydrogen plasma the silane flow was started. Since the main part of the total flow already consists of hydrogen, this would not seriously affect the pressure control system. The expected result of this ‘hydrogen start’ was an increased crystalline ratio because a hydrogen plasma is known to cause crystallization in the top (seed) layer [58] and because the first silicon species to arrive at the substrate would experience longer surface diffusion times related to the low initial concentration of silane in the reactor. The effect of a 5-second hydrogen treatment on the underlying p-layer was examined by Raman spectroscopy as presented in Figure 5.8.

The peak intensity of both signals were normalized so that it becomes clear that no macroscopic change in the crystalline structure took place as a consequence of the hydrogen plasma that was applied to increase the crystalline ratio of the layer that was to be deposited subsequently.

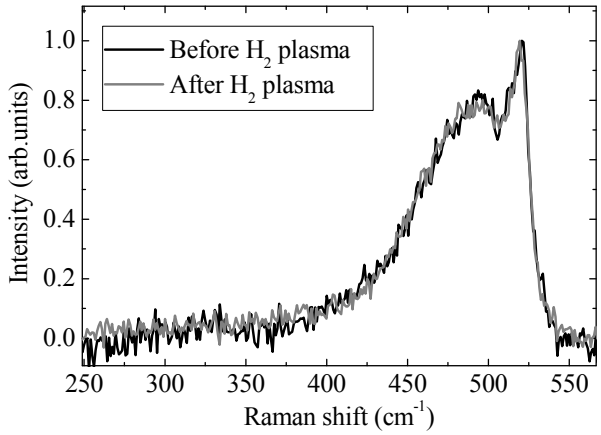

Figure 5.8: Normalized Raman traces with their background removed showing the effect of a 5-second H_2-plasma start on the 27 nm nc-Si:H seed layer.

The effect of the implementation of the hydrogen start procedure to the high deposition rate deposition process was very strong, as can be seen from Figure 5.9.

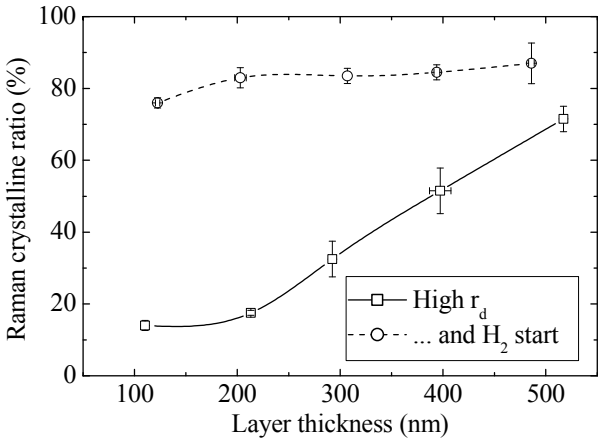

Figure 5.9: Evolution of the Raman crystalline ratio in high-r_d nc-Si:H layers of increasing thickness deposited on top of a nc-Si:H seed layer, both without and with a 5-second H_2-plasma start at the beginning of the deposition.

It indeed provided the desired reduction of the thickness of the incubation layer. In fact, the incubation layer for the films deposited with the 5-second H_2-plasma start was much less

than 100 nm and could not be detected with Raman spectroscopy anymore. The crystalline ratio after 100 nm of high r_d deposition with the hydrogen plasma start was already higher than that of a 500 nm film deposited at high rate without hydrogen plasma start.

5.3.3 Hydrogen start and surface morphology

In a typical Raman measurement, after background subtraction, the spectrum exhibits not only the peaks of interest that are indicative of the phase composition of the silicon material under investigation, but also a peak of unshifted energy, representing the laser at its original photon energy. The strength of this laser line in the Raman spectrum is dependent on the scattering strength, which is mainly caused by the roughness of the sample. If the sample is smooth, then the laser light is reflected specularly towards a dump location, while the Raman signal, which is diffuse by nature, finds its way to the detector via a lens system. With increasing roughness of the sample material, an increased amount of the unshifted laser light is scattered towards the detector as well.

When the samples that were deposited with the H_2-plasma start were characterised with the Raman setup, a clear difference with the conventionally deposited high r_d material was noticeable. For the latter material, usually an increasing roughness with increasing thickness is observed.

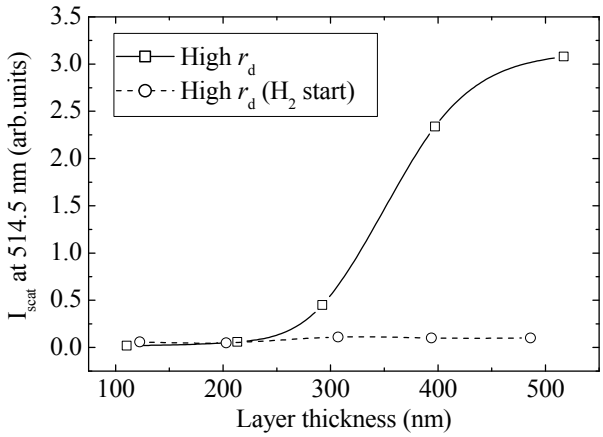

Figure 5.10: Scattering from the Raman laser (514.5 nm) for the thickness series of high deposition rate material without and with a H_2-plasma start.

However, the scattering signal in the Raman setup indicated that the material deposited using the H_2-plasma start procedure, had significantly lower roughness for all layers with a thickness of 300 nm and above (Figure 5.10).

To quantify the differences in roughness, the same samples have been investigated using Atomic Force Microscopy (AFM) in tapping mode with a silicon tip, analysed with the WSxM software [86] and visualised using the POV-Ray software [87]. Figure 5.11 shows 3D impressions of the surface morphology of the samples, both with and without H_2-plasma start and at two different thicknesses.

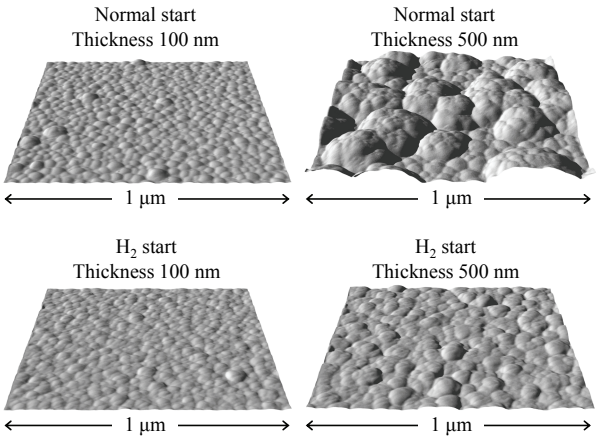

Figure 5.11: AFM surface image of high deposition rate nc-Si:H, deposited with the different methods and at different thicknesses. Roughness analysis, performed on a 25 times larger area than shown, yielded 2.5 nm and 22 nm for the top row and 2.6 nm and 5.1 nm for the bottom row for 100 nm and 500 nm thick films, respectively.

The morphologies for 100 nm thickness appear similar, and the *rms* roughness of both samples was almost equal, being 2.5 nm for the conventional start and 2.6 nm for the H_2-plasma start. However, as shown in Figure 5.9, the difference in crystalline ratio as determined from Raman spectroscopy is very large, since the material deposited with the H_2-plasma start was already highly crystalline after 100 nm, whereas the material deposited without special treatment consisted still mostly of amorphous phase material. After 500 nm of growth the material deposited without the H_2-plasma start was much rougher, with a surface *rms* roughness of 22 nm, than the layer deposited with the alternative start, which had a *rms* roughness of 5.1 nm. In the first case the spherical caps of the developed

crystalline cones can still be identified, indicating a much lower density of nucleation sites in the initial phase compared to the latter case of the H_2-plasma start.

5.3.4 Tuning the crystalline ratio after a hydrogen plasma start

Since the H_2-plasma start was a great aid towards improvement of the homogeneity in the growth direction by strongly reducing the incubation layer in the high r_d regime, methods to reduce the average crystalline ratio could be studied. The first attempt was to alter the hydrogen flow, as it is the normal procedure for the tuning of the crystalline ratio in conventional deposition regimes. In this experiment a series of layers were deposited using different H_2 flows. The resulting Raman spectra for these films are presented in Figure 5.12. In each of these depositions the H_2 flow that was used during the deposition was also employed during the 5 seconds of initial H_2-plasma treatment. That means that the last curve in this figure represents the experiment where there was no hydrogen flow during the initial 5 seconds; the H_2-plasma treatment was a closed chamber treatment only in that case. As soon as the silane flow was started the pressure control valve opened in order to keep the process pressure constant.

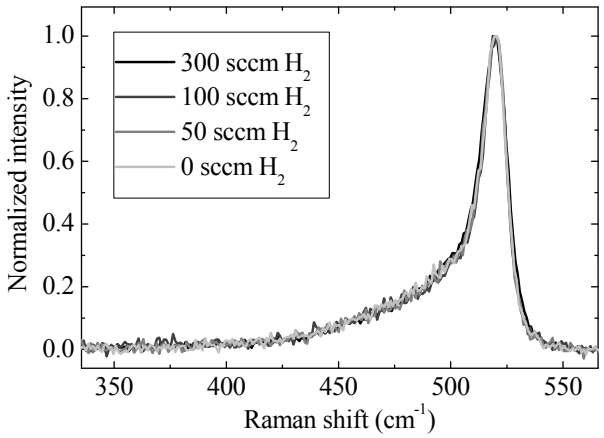

Figure 5.12: Normalized Raman signal for layers of 100 nm deposited using the H_2-plasma start method and using different H_2 flows during deposition.

The resulting spectra show that it is futile to try to control the crystalline ratio in the bulk of the material by variation of the hydrogen flow, since there is no difference at all in the

observed crystalline ratio, even if the hydrogen flow is completely absent. This is consistent with an experiment from the literature mentioned before [85], where it was found that upon elimination of the back diffusion mechanism by choosing a proper background gas mixture in the reactor, high quality nc-Si:H material could be attained from a pure silane flow. That experiment was done with a deposition rate of about 1 nm/s, whereas the present results show that very high deposition rate nc-Si:H material (5 nm/s) can be made from a pure silane flow as well. An explanation for this observation is that the silane utilization is already very close to 100% in the case of the original hydrogen flow, so that the decreased hydrogen inflow results only in a decreased outflow of hydrogen to the pumps, leaving the gas composition essentially the same. What does change, is the residence time of the gas in the reactor, which may have its effect on the amount of powder that is produced.

Since the degree of gas utilization appears to play an important role in this deposition regime, the next step was to try to decrease this utilization degree by increasing the flow of silane. The results of that experiment are presented in Figure 5.13.

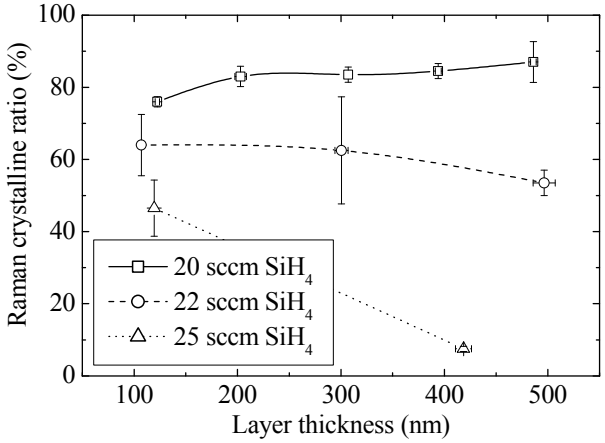

Figure 5.13: Raman crystalline ratio in layers of increasing thickness deposited at high (4.5 nm/s) rate using a H_2-plasma start of 5 seconds. Different curves represent different, indicated silane flows.

This figure shows that with the original silane flow of 20 sccm, the crystalline ratio remained at a high level throughout the deposition. When the silane flow was increased, the crystalline ratio after 100 nm was lower than it was under the original deposition conditions, provided the H_2-start was applied. Using 22 sccm of silane, the Raman

crystalline ratio was around 50% after 500 nm of deposition. After about 400 nm of growth using 25 sccm, the material turned out to have become predominantly of a-Si:H structure. Two mechanisms can be simultaneously responsible for the decline of the crystallinity in the growing film. Firstly the increased availability of silane resulted in an increased dissociation of silane and accordingly, because the VHF power remained constant during the deposition, a reduction of the dissociation of hydrogen. This resulted in a lower flux ratio of atomic hydrogen-to-silane species. Secondly, since the total amount of silane is no longer fully utilized, a background concentration of silane started to develop in the inactive volume of the reactor. Via the mechanism of back diffusion, this increased the available silane in the active part of the reactor, where the plasma is located, even more. Both mechanisms should, in the ideal case, be visible in the Si^* emission measured with OES. However, the variation in the OES emission intensity due to pressure fluctuations made it impossible to detect these small variations in the Si^* emission. It was estimated in Subsection 5.2.2 that the stabilisation time for the back diffusion mechanism was around 30 seconds; in 30 seconds a film thickness of about 150 nm can be achieved under high deposition rate conditions. The fact that the phase composition is still changing after the deposition regime is stabilized, can be explained from the influence of the local epitaxy on the structure of the deposited film [88]; deposition in a regime that would normally yield a-Si:H growth, but close to the transition to nc-Si:H growth, on an interface with a significant crystalline ratio, will still grow nc-Si:H.

5.4 Conclusions

When depositing nanocrystalline silicon at a high rate, it is important to account for the influence of back diffusion and the characteristic timescales and length scales that are involved. Because of the high deposition rate, a few seconds of non-ideal plasma conditions may result in thick incubation layers in devices, which have a strong deleterious influence on performance. The deposition regime and in particular the crystalline ratio are very sensitive to small changes in control parameters that determine the degree of depletion, such as the VHF power and the silane flow, and to initial conditions. This makes the reproducible deposition of high rate nanocrystalline silicon far from trivial.

However, it is possible to control the crystalline ratio of the growing film at every stage of the deposition. A constant, optimal crystalline ratio over the entire thickness of the film can be achieved by application of a hydrogen plasma start, together with profiling of the VHF power or the silane flow.

Chapter 6

Performance and stability of high-deposition rate solar cells

Abstract

A series of layers with varying crystalline ratio was deposited using Very High Frequency Plasma Enhanced Chemical Vapour Deposition (VHF PEVCD) with a high deposition rate around the transition from the amorphous to the nanocrystalline phase. The crystalline ratio was controlled by variation of the delivered power. Solar cells of the p-i-n-type with the same 6.4% conversion efficiency were obtained, employing hydrogenated amorphous silicon (a-Si:H) and hydrogenated nanocrystalline silicon (nc-Si:H) deposited at 4.5 nm/s and 3.2 nm/s, respectively.

The a-Si:H cells showed a normal light-induced degradation of 20% relative. The defect density of the i-layer in the nc-Si:H solar cells was determined from the sub-band gap absorption obtained from Fourier Transform Photocurrent Spectroscopy (FTPS) before and after light soaking. The nc-Si:H solar cells were very stable under light soaking, and although the mid-gap defect density remained constant, the solar cells even improved slightly.

High-deposition rate nc-Si:H solar cells have been subjected to a 1-MeV proton beam to investigate their radiation hardness. The inflicted damage is visible in a strong increase of the dangling bond density. This could partially be undone by isochronal annealing up to 180°C, the temperature at which *light*-induced dangling bonds are known to be annealed away completely. From comparison of the results with a similar experiment in the literature the suggestion arises that the thickness of the cells is an important parameter to the degree of radiation hardness.

6.1 Introduction

Typical deposition rates for the intrinsic layer in performance-optimized thin film silicon solar cells, for both a-Si:H and nc:Si:H, are in the Å/s range. Therefore the deposition times, in particular for nc-Si:H i-layers that need to have a thickness up to 2 or 3 μm, are in

the order of hours. Therefore, the deposition of this type of layer, both in tandem structures and in single junction designs, will be a bottleneck in a high throughput production process. Or, in the case of a roll-to-roll production line, a long deposition time translates into a section of the deposition reactor that has to become very long compared to the compartments for the other layers in a typical device, which brings additional costs for production space, vacuum equipment and of course the technical realization of homogeneous source gas and Radio Frequency (RF) power distribution over such lengths. Thus, it may be more economic to produce the intrinsic layers at a much higher deposition rate, even if it is at the cost of a reduced performance of the cells. In this chapter a study on the performance of high deposition rate intrinsic thin film silicon layers both as a material and as intrinsic layer in solar cells is presented. The performance of the high-deposition rate (r_d) material is compared to that of device-optimized intrinsic layers. Furthermore, the light induced degradation has been investigated for both high r_d-a-Si:H and high r_d-nc-Si:H, and finally a study on proton degradation of the high-deposition rate nc-Si:H solar cells is presented, exploring the feasibility of this solar cell type for space applications.

6.2 Deposition and initial performance

6.2.1 Deposition

The series of layers was deposited using the deposition regime for high-r_d material as described in Subsection 2.2.2. The delivered VHF power was varied in order to obtain films with a range of phase compositions around the transition from a-Si:H to nc-Si:H. The deposition rate and the optical emission in these regimes were discussed in Subsection 5.1.2.

Furthermore, nc-Si:H and a-Si:H solar cells were deposited in the high pressure depletion regime. The nc-Si:H silicon solar cells were made with an nc-Si:H absorber layer of one micrometer deposited with 4.5 nm/s. This layer was deposited using a showerhead electrode with 6 mm spacing between the powered electrode and the grounded substrate. The delivered electrical power was 350 W and had a frequency of 60 MHz. The pressure was 9 mbar and the flows of hydrogen and silane were 500 sccm and 18 sccm, respectively. The temperature of the substrate was calibrated to be 200°C at the beginning of the

deposition. This layer was incorporated in a p-i-n structure that was deposited on a texture-etched ZnO:Al substrate on glass. The p-layer was an nc-Si:H layer of 27 nm thickness and the n-layer was an a-Si:H layer of 40 nm. On top of the p-i-n structure a back reflector was applied that consists of 100 nm ZnO:Al followed by evaporated silver and aluminium back contacts. The metal contacts of 4×4 mm^2 defined the area of the test cells; the ZnO:Al outside the area of the metal contacts were etched away by diluted HCl.

The intrinsic layer in the a-Si:H solar cells was 500 nm deposited at 3.2 nm/s. This layer was deposited under very similar conditions as the nc-Si:H cell, differing only in the silane flow of 20 sccm, and the delivered power of 200 W. This layer was incorporated in a p-i-n structure that was deposited in the ASTER deposition system on a commercial Asahi U-type substrate consisting of glass covered with a textured layer of SnO_2:F. The p-layer was an a-Si:C:B layer of 9 nm thickness and the n-layer was an a-Si layer of 33 nm thickness. This second cell has the same back reflector construction and type of contacts as the first cell.

6.2.2 Properties of the layers

For each deposited layer a crystalline ratio was derived using the method of spectral subtraction that is described in Chapter 2. The relation between the delivered power and the Raman crystalline ratio is depicted in Figure 6.1.

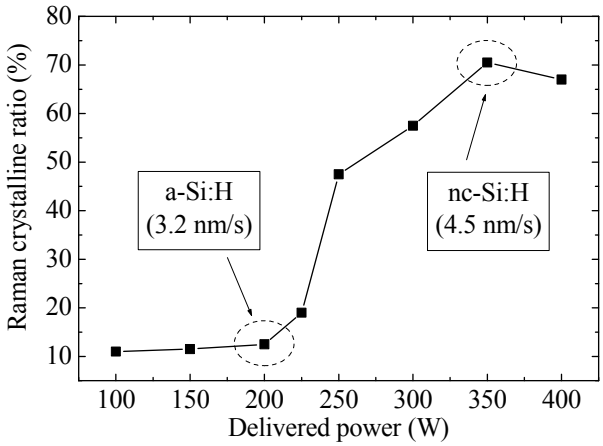

Figure 6.1: Delivered power and Raman crystalline ratio. Indicated are the growth rates for the regimes selected to deposit solar cells, which are the topic of Subsection 6.2.3.

It is evident from the figure that it is possible to deposit materials that have a broad range of crystalline ratios using only the VHF power as the controlling deposition parameter.
The activation energy and photosensitivity of the materials are presented Figure 6.2 and Figure 6.3.

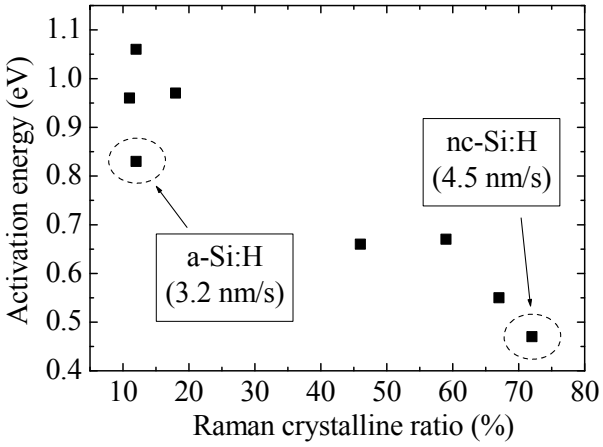

Figure 6.2: Activation energy vs. Raman crystalline ratio for a series of 500 nm-films deposited using different values of the delivered power.

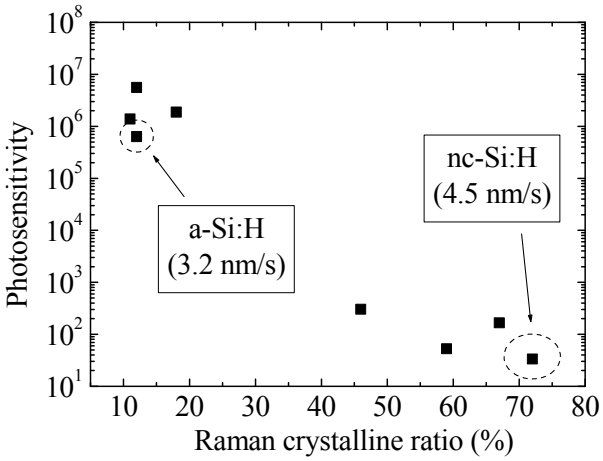

Figure 6.3: Photosensitivity vs. Raman crystalline ratio for a series of 500 nm-films deposited using different values of the delivered power.

From these figures it becomes clear that the obtained range of crystalline ratios includes the desirable types of material close to the transition from a-Si:H to nc-Si:H material, where the

optimal conditions are found for solar cells [49, 50]. The two regimes for high deposition rate a-Si:H and nc-Si:H silicon that are indicated in Figure 6.1 - Figure 6.3 were chosen for the deposition of solar cells, to form a trade-off between deposition rate and material quality. The properties of the resulting solar cells are presented in Subsection 6.2.3.

6.2.3 Properties of the deposited solar cells

The cell parameters of the high r_d solar cells are shown in Table 6.1, together with performance-optimized nc-Si:H and a-Si:H solar cells that were also deposited using VHF PECVD.

Table 6.1: Solar cell parameters for nc-Si:H and a-Si:H solar cells deposited at high rates in comparison with parameters for performance-optimized solar cells.

Type	r_d *(nm/s)*	N_{eff}	J_{sc} *(mA·cm^{-2})*	V_{oc} *(V)*	*FF*	R_s *(Ω·cm^2)*	R_p *(Ω·cm^2)*	*n*	J_0 *(mA·cm^{-2})*
nc-Si:H	4.5	6.4	20.3	0.47	0.67	2.6	237	1.48	$5.1\cdot10^{-5}$
nc-Si:H	0.5	9.9	26.3	0.52	0.73	1.4	559	1.36	$8.0\cdot10^{-6}$
a-Si:H	3.2	6.4	12.3	0.91	0.57	9.0	444	1.71	$3.3\cdot10^{-9}$
a-Si:H	0.2	9.4	15.8	0.89	0.67	6.5	2006	1.45	$6.3\cdot10^{-10}$

The properties of the solar cells that are fabricated at high deposition rates mainly depart from their performance-optimized low deposition rate counterparts in the fill factor, the J_{sc}, and the V_{oc}. There is also a distinct difference in the dark J-V characteristics between the high and low deposition rate solar cells. The saturation current J_0 is an order of magnitude higher for high-r_d solar cells, and the increased value of the diode quality factor n indicates an increased density of defect states as well. In Figure 6.4 the electrical behaviour of both types of high-r_d solar cells is presented. Both the high r_d solar cells and the performance-optimized solar cells are shown.

Figure 6.5 shows the spectral response for both the nc-Si:H and the a-Si:H cell that was deposited at a high deposition rate, together with the spectral response obtained for typical performance-optimized solar cells. What is obvious from the electrical characteristics is again visible here: especially for the nc-Si:H cell it holds that the quantum efficiencies reported for performance-optimized nc-Si:H is much higher resulting in a higher current.

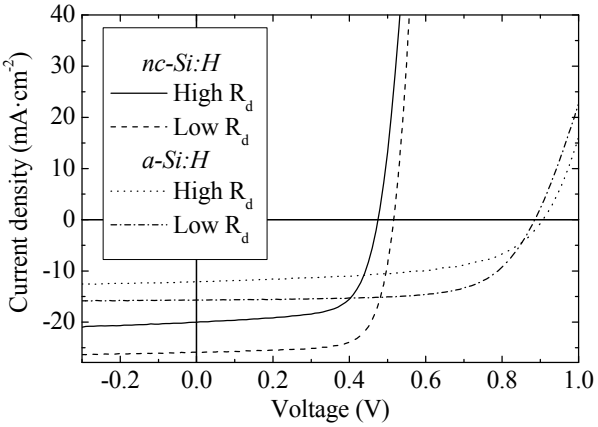

Figure 6.4: AM1.5 J-V curves for high-deposition rate nc-Si:H and a-Si:H solar cells together with the JV curves of performance-optimized solar cells.

The indicated J_{sc} values are determined by convolution of the spectral response curve with the solar spectrum over the relevant wavelength range. These J_{sc} values may differ from the values from Table 6.1 because of spectral differences between the solar simulator spectrum and the AM1.5 spectrum. Other factors include the missing wavelength range above 950 nm and below 350 nm in the spectral response measurement, and integration errors due to the spectral resolution of the quantum efficiency measurement.

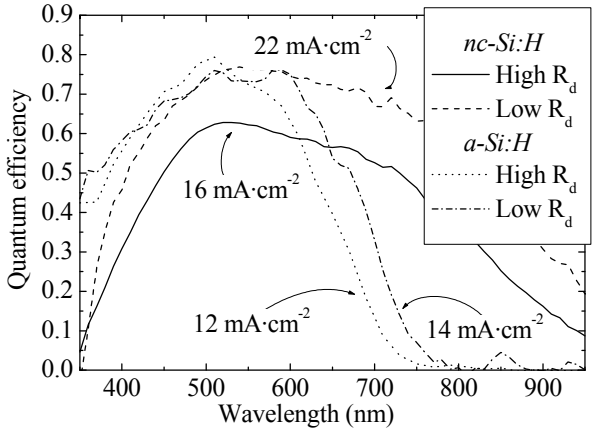

Figure 6.5: Spectral response for high deposition rate nc-Si and a-Si solar cells together with the spectral response of performance-optimized solar cells; the measurements are performed under short circuit conditions and white bias light illumination. Indicated are the J_{sc} values corresponding to each curve.

6.3 Light-induced degradation of high deposition rate solar cells

6.3.1 Description of the light soaking experiment

The effect of light soaking on high deposition rate solar cells was monitored in a degradation setup with continuous illumination by a combination of halogen lamps, metal-halide lamps and high-power white LEDs with a spectrum comparable to the AM1.5 solar spectrum and an intensity approaching 100 mW/cm^2. A temperature control system maintained the cell temperature at a constant level of 50ºC. Before the experiment the cells were annealed for 30 minutes at 160°C in a nitrogen environment to minimize the effect of the heating during lightsoaking. To investigate the trends of the various solar cell parameters during the process of light soaking, without the need to interrupt the light soaking process too often, the cells in the light soaking setup remained permanently connected to a computer controlled Keithley 2400, which recorded the J-V curves of the cells in situ at exponentially increasing time intervals and kept the cells in the open-circuit condition (worst case condition) between the measurements. A reference cell was measured along with the cell under investigation to correct for the fluctuations in the lamp intensity during the in situ J-V measurements. Before and after the degradation experiment the J-V characteristics of the solar cells were characterized using the AM1.5 spectrum of the solar simulator.

6.3.2 Effect of light soaking on the fill factor

Figure 6.6 shows the in situ behavior of the fill factor of the solar cells during the light soaking experiment. The high-r_d a-Si:H solar cell degraded mainly in fill factor, which is indicative for the Staebler-Wronski-effect [2] that normally affects the performance of a-Si:H solar cells when subjected to light intensities that are comparable to AM1.5 sunlight. This effect can be attributed to the increase in the density of the dangling bonds, which results in an increase in electronically active defects causing recombination and therefore a loss of current, especially at low internal electric field, that is, under forward biased conditions of the solar cell.

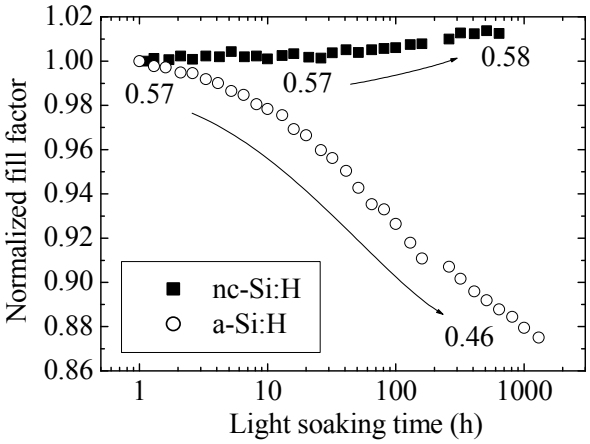

Figure 6.6: The normalized fill factor of high-r_d a-Si:H and nc-Si:H solar cells during light soaking. The values in the graph indicate the fill factors measured before and after the experiment using AM1.5 illumination.

In this case the degradation in the conversion efficiency of the high r_d a-Si:H solar cell from the as-deposited state to the stabilized condition after more than 1000 hours of light soaking was 20%, which is comparable to the stability of low deposition rate a-Si:H solar cells [89, 90].

The nc-Si:H cell improved rather than degraded as a result of the illumination, even though the initial point was taken after the cells had passed through an annealing step before starting the light soaking experiment. This behaviour is not only observed for high deposition rate nc-Si:H solar cells, but also for performance-optimized nc-Si:H solar cells. The question arises if this change in performance is related to a change in the dangling bond density as well. A suitable technique for the measurement of the mid-gap defect density is FTPS.

6.3.3 Effect of light soaking on the defect density

To investigate if the dangling bond density in the light-soaked nc-Si:H solar cell had increased or not, in the light-soaked nc-Si:H solar cell, it is interesting to examine the absorption in the near infrared. Absorption at mid gap photon energies indicates the presence of electronically active defect states in the material, the so-called dangling bonds. A decrease or increase would likewise be visible in the absorption spectrum. FTPS is a

highly suitable method to obtain the absorption characteristics of a nc-Si:H solar cell, enabling the measurement of defect absorption in a completed cell structure.

In Figure 6.7 the absorption curve, obtained using FTPS, is shown for the nc-Si solar cell. The absorption at 0.8 eV is assumed to be proportional to the density of dangling bonds [22]. One has to keep in mind that the absorption as measured using FTPS as such does not include corrections for scattering or interference effects. However, the fact that both curves coincide in the region above 1.0 eV, together with the knowledge that it is very unlikely that exactly the same spot on the solar cell was probed before and after the light-soaking, indicate that the scattering is sufficiently homogeneous. As long as the absorption coefficiënt α and the sample thickness d are small enough so that $\alpha \cdot d << 1$, which is the case for the weakly absorbing nc-Si:H especially in the infrared region of the spectrum, the generated photocurrent can be taken to be proportional to the absorption coefficient. The FTPS spectra have been calibrated to the absorption spectrum of crystalline silicon at 1.4 eV.

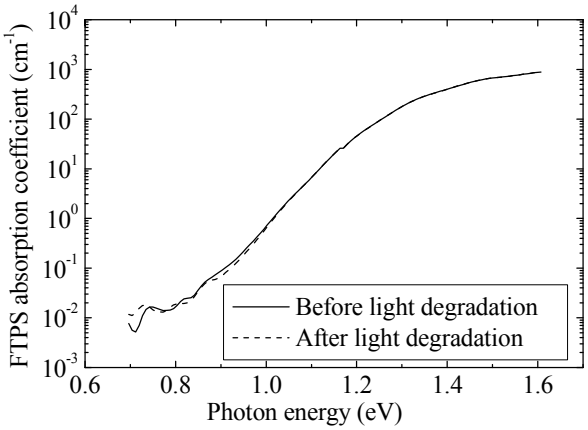

Figure 6.7: FTPS absorption curves for nc-Si:H with high deposition rate prior to and after light soaking. The spectra have been calibrated to the c-Si absorption spectrum at 1.4 eV.

The sensitive FTPS measurement shows no change in the absorption at 0.8 eV, indicating that there is no significant change in the amount of midgap defect states. Therefore, although a changing fill factor is observed during light soaking, the trends in the cell performance are not correlated to a change in the density of midgap states in the material. It

is possible that the long term annealing at a controlled 50°C improves the contact between the cell and the back electrode.

6.3.4 Conclusions on light-soaking

For a-Si:H deposited under performance-optimized conditions using considerable H_2 dilution a relatively high light soaking stability is expected [33] and an observable increase of the medium-range order in the material [35]. Although the high-r_d a-Si:H solar cells presented here are deposited using a considerable H_2 dilution as well, the plasma conditions are very different, involving high power and pressure and therefore a high probability of incorporation of SiH_2 bonds in the amorphous matrix, that have a negative effect on the stability [91]. The Urbach energy of 60 meV in this material, measured using the constant photocurrent method (CPM), confirms that a high concentration of SIH_2 bonds is present in this high-r_d a-Si:H material [92]. The high-r_d nc-Si:H solar cells were very stable under light-soaking; no sign of light-induced defect creation could be detected using the sensitive FTPS method.

6.4 Proton irradiation of nanocrystalline silicon solar cells

6.4.1 Potential for thin film solar cells in space

Space applications of thin film solar cells thus far have not drawn much attention, although they can have an exclusive advantage over conventional wafer-based solar cells due to their low weight. For solar cells to be used in space, it is rather the weight per watt-peak than the cost per watt-peak that matters, which would make thin film cells a superior choice, provided that a suitable lightweight substrate is used, such as plastic or thin metal foil. However, a second necessity for space solar cells is their radiation hardness. The radiation hardness of nc-Si:H solar cells is the topic of this section. It is not possible to make definite conclusions about the lifetime of nc-Si:H solar cells in space, since the radiation conditions strongly depend on the type of space mission and the activity of the sun, which is the main source of the radiation. However, it is possible to compare the present results to similar experiments on nc-Si:H [93] and amorphous a-Si:H [94] or tandem cells consisting of both materials [95]. Thin film silicon solar cells generally show a higher radiation hardness

compared to multicrystalline silicon (mc-Si) solar cells. Since crystalline silicon (c-Si) has an indirect band gap and a correspondingly low optical absorption coefficient, mc-Si solar cells have to be thick and the carrier collection is based on diffusion rather than drift. Therefore, in mc-Si solar cells defect creation by radiation has a relatively large effect [96]. Investigations of the proton irradiation resistance for c-Si and mc-Si solar cells can be found in [97, 98]. Those experiments were performed using mostly 10-MeV protons, whereas in this section the used proton energy was 1 MeV.

6.4.2 Proton irradiation of nanocrystalline silicon solar cells

Superstrate type nc-Si solar cells were deposited using the same conditions as described in Section 6.2.1, on top of a texture-etched ZnO:Al TCO layer [10]. The i-layer thickness was about one micrometer. After characterisation, the cells were subjected to a 1-MeV proton beam from the thin film side. The penetration depth for protons with this energy is in the order of one millimeter into the glass. Since the film thickness was much less than that, the energy dissipation was practically homogeneous over the thickness of the film. The cells were in open-circuit condition and at room temperature during the irradiation. The set consisted of 30 test cells. The cells were divided into five groups, each of which received a different fluence of high energy protons, ranging from 10^{13} to 10^{15} protons per cm^2. In addition a group was included that received no irradiation at all, which served as a reference. Before and after proton irradiation, the cells were characterised using current-voltage (J-V) measurement under dark and AM1.5 conditions, spectral response and FTPS; as in Section 6.3.3, FTPS was used to measure the sub-gap absorption which is taken to be proportional to the mid-gap density of defect states. After characterisation, the cells that had received the largest proton fluence were isochronically annealed in ten-minute, ten-degree steps up to 180°C and after each step the sub-gap absorption was measured again.

6.4.3 Effect of proton irradiation on electrical performance

Figure 6.8 shows the normalized solar cell performance parameters, i.e. the short-circuit current (J_{sc}), the open-circuit voltage (V_{oc}), the fill factor (FF) and the conversion efficiency (N_{eff}), under AM1.5 illumination. Each point consists of the average of 4 test cells that received the same fluence. The degradation affects all cell parameters. N_{eff} shows the

greatest decrease in performance, since it is the product of the other three numbers. It is remarkable that the V_{oc} and the J_{sc} degrade more than the fill factor. The cause of this behaviour is not fully understood. The glass substrate did not show any degradation on visual inspection. An infrared camera did not reveal any observable proton-induced change to the glass transparency either, so that darkening glass can be ruled out as a main cause for the observed trend. It is therefore speculated that, in addition to damage to the bulk of the i-layer, the ZnO:Al layer is affected by the proton radiation as well.

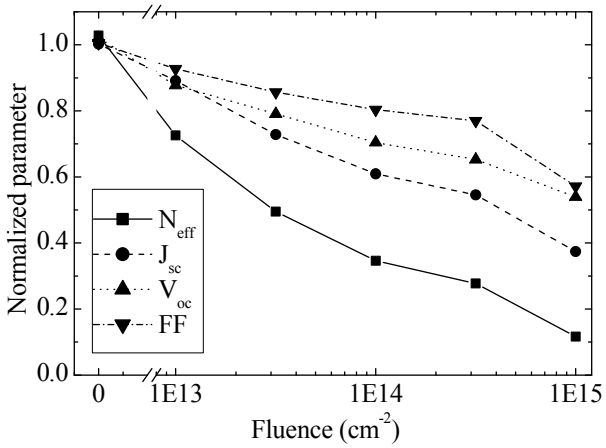

Figure 6.8: Normalized parameters from JV measurement, averaged over 4 cells.

Figure 6.9 shows some of the results of Klaver [94] for a similar experiment on amorphous silicon cells, together with the behaviour of the nanocrystalline silicon solar cell described in this section. The degradation of the nc-Si:H cell with increasing fluence shows a trend similar to that of a-Si:H cells. Moreover, the degradation appears to be dependent on thickness, regardless of the type of material used. This is understandable, since the energy deposition of the radiation is homogeneous, and therefore proportional to the cell thickness, whereas solar cell performance is typically measured on a per-unit-area basis. In thicker solar cells, more defects are created per unit area.

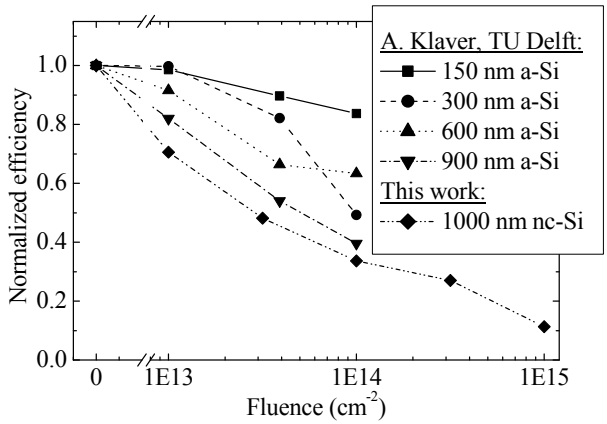

Figure 6.9: Effects of proton degradation on both amorphous and nanocrystalline silicon solar cells.

6.4.4 Effect of proton irradiation on quantum efficiency

The average spectral responses for the differently irradiated groups are shown in Figure 6.10. The fact that the cells are relatively thin for nc-Si:H cells and that they lack a ZnO:Al-Ag back reflector construction is clearly visible in the quick decrease of the quantum efficiency in the red part of the spectrum.

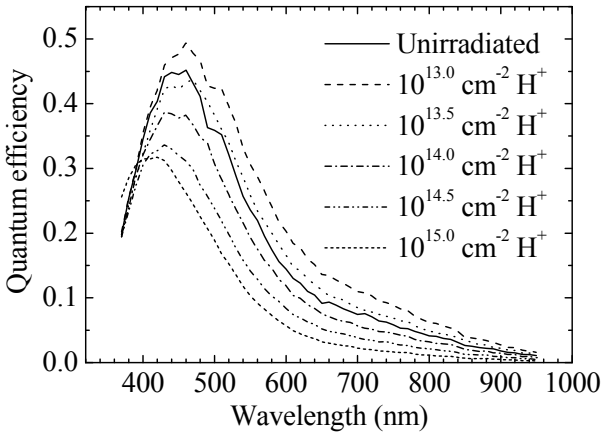

Figure 6.10: The spectral response of cell groups with varying proton damage.

Because the spread in results from different cells, and the limited degradation after the smallest fluences, the spectral response of two of the irradiated groups of cells is actually better than the unirradiated group in Figure 6.10. Therefore, a clearer presentation of the

spectral response is given in Figure 6.11, which shows the spectral response curves of groups of varying proton fluence relative to the response of the same groups before the degradation. This figure makes it very clear that the biggest setback in quantum efficiency caused by the proton irradiation occurs in the red part of the spectrum. Note that the quantum efficiency of the unirradiated sample also departs from the first measurement. This is partially attributed to the measurement error and partially to environmental and handling effects on the sample during the experiment.

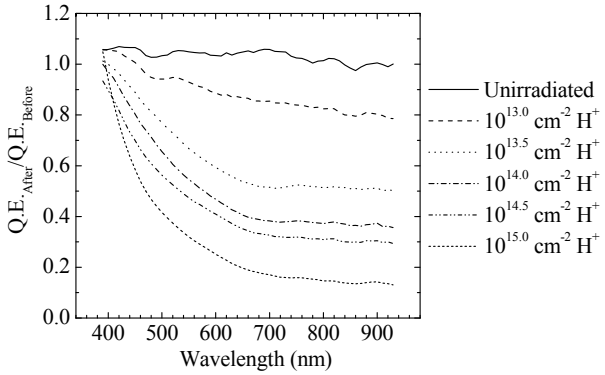

Figure 6.11: The ratio of the quantum efficiencies before and after the proton irradiations, averaged for each group of cells.

6.4.5 Effect of proton irradiation on defect density

Figure 6.12 shows the result of the FTPS measurement of the absorption coefficient in the infrared part of the spectrum. A large change in the absorption coefficient is observed for photons with energy around 0.8 eV. The absorption coefficient at 0.8 eV is commonly taken to be proportional to the dangling bond density [22]. Again, all measured FTPS spectra have been calibrated to the c-Si absorption spectrum at 1.4 eV. At 0.8 eV, the absorption coefficient increased by a factor of 20 in case of the largest proton fluence.

This is represented more clearly in Figure 6.13, where the ratio between the absorption curves before and after the measurements is shown. In this figure also a change of the absorption on the right side of the 1.4 eV calibration point is observed. This suggests a slight amorphisation by the irradiation, although too small to be detectable by Raman spectroscopy. Using a proportionality constant [22] between α(0.8 eV) and the density of

mid-gap defect states, N_d, it is found that for the largest fluence of 10^{15} 1-MeV protons per cm^{-2}, N_d increased from 10^{16} cm^{-3} to 2×10^{17} cm^{-3}.

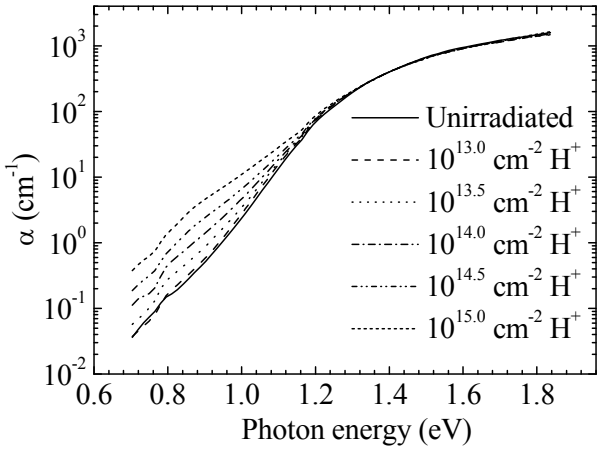

Figure 6.12: FTPS absorption of nc-Si solar cells with varying proton damage.

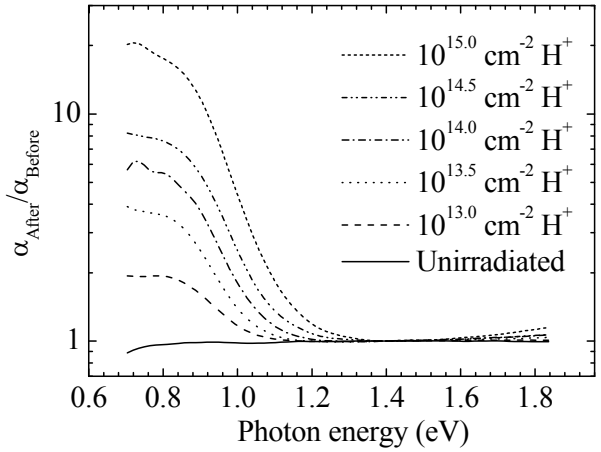

Figure 6.13: Ratio of the absorption in proton degraded cells to that of the reference group.

6.4.6 Annealing of nc-Si:H solar cells damaged by proton radiation

In order to test the reversibility of the proton-induced defect creation, the cell that received the largest fluence was annealed. After annealing this cell in a nitrogen atmosphere in consecutive steps of ten minutes at temperatures increasing by 10°C for each step up to

180°C, the absorption coefficient was observed to decrease again. Figure 6.14 shows the absorption coefficient of this cell after annealing relative to its as-irradiated state. To prevent the figure from becoming too cluttered, the 110°C, 130°C, 150°C, and 170°C, steps are not shown. After the 180°C step, the absorption coefficient, and therefore the defect density, was reduced by a factor of 5. The absorption coefficient at 0.8 eV finally reached a level very comparable to that of the samples that received a fluence of 3×10^{13} cm^{-2}. The conversion efficiency, however, as could be inferred from Figure 6.8, was not restored to a level consistent with this fluence, thus indicating that the inflicted damage is not totally reversible by annealing.

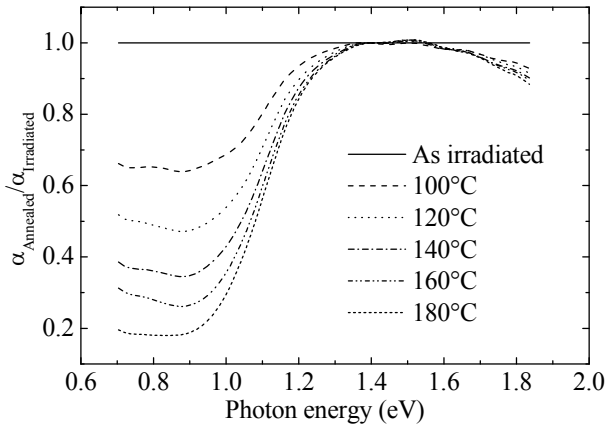

Figure 6.14: Isochronal annealing of the cell that received the highest fluence. The curves indicate the absorption coefficient relative to the as-irradiated condition of the cell, after the 10-minute step at the indicated temperature.

The annealing treatment was not continued above 180°C, to stay clear of the deposition temperature and rule out the possibility of concomitant structural modification. At this temperature, dangling bonds that were created by illumination, should have been removed completely [1].

6.4.7 Conclusions on proton irradiation

After irradiation with 10^{15} 1-MeV protons the performance of a typical nanocrystalline silicon solar cell is decreased to 10% of its original conversion efficiency. From the quantum efficiency it can be concluded that most of the performance is lost in the low

energy part of the spectrum, for which the charge carriers are created in the bulk of the cell. From the absorption coefficient in the infrared as measured from FTPS it is learned that the amount of mid gap defects is strongly increased by the degradation by protons. The strongly increased recombination causes a degradation of the quantum efficiency, which is strongest in the red part of the spectrum. Comparison with similar experiments on thin film a-Si:H solar cells from the literature [94] suggests a relation between thickness and performance degradation for thin film cells. This makes the thinner a-Si:H solar cells the better candidate for space applications compared to nc-Si:H solar cells. The negative effects of the proton degradation on the defect density can only partially be undone by thermal treatment.

6.5 Conclusions

Solar cells of nc-Si:H and a-Si:H that were deposited with a high deposition rate of 4.5 and 3.2 nm/s respectively, had a reasonable conversion efficiency of 6.4%, for both types of solar cells. The light-induced degradation of the high-r_d a-Si:H solar cell was typical for a-Si:H solar cells. The high-r_d nc-Si:H solar cell was very stable under light-soaking and its fill factor even showed some improvement. The defect density in the intrinsic layer of this solar cell, which was an order of magnitude higher than that of performance-optimized nc-Si:H, was not affected by light-soaking.

1-MeV proton irradiation of the high-r_d nc-Si:H solar cells showed that these cells have less then 10 % of their original conversion efficiency after receiving a 1-MeV proton fluence of 10^{15} cm^{-2}. A comparison with a-Si:H proton degradation revealed that a-Si:H solar cells are more resistant to proton irradiation, but this is apparently because of the thickness of the respective solar cells, the nc-Si:H being the thicker cells, and not related to the type of material used.

The fact that the proton induced defects could be partially removed by annealing suggests that a part of these defects are of the same nature as light-induced defects. On the other hand, there are a number of differences between the effects of proton irradiation and the Staebler-Wronski effect: Light-induced degradation affects mostly the fill factor whereas in proton-induced degradation the fill factor was the least affected parameter. Furthermore, nc-Si:H was found to be highly stable against light-induced degradation, contrary to a-Si:H;

however the proton-induced degradation affects both materials in the same way. And finally, light-induced defects can be fully removed by annealing at 180°C [1], but the proton irradiation damage is not fully reversible. These observations show that the defect creation mechanism by proton irradiation is fundamentally different from light-induced degradation.

Bibliography

[1] C. R. Wronski, B. von Roedern and A. Kolodziej, *Vacuum* **82** (2008), p. 1145.

[2] D. L. Staebler and C. R. Wronski, *Applied Physics Letters* **31** (1977), p. 292.

[3] M. Berginski, J. Hüpkes, M. Schulte, G. Schöpe, H. Stiebig, B. Rech and M. Wuttig, *Journal of Applied Physics* **101** (2007), p. 074903.

[4] M. Berginski, J. Hüpkes, A. Gordijn, W. Reetz, T. Wätjen, B. Rech and M. Wuttig, *Solar Energy Mat. and Solar Cells* **92** (2008), p. 1037.

[5] B. Yan, G. Yue, J. M. Owens, J. Yang and S. Guha, *Applied Physics Letters* **85** (2004), p. 1925.

[6] B. Rech, T. Roschek, T. Repmann, J. Müller, R. Schmitz and W. Appenzeller, *Thin Solid Films* **427** (2003), p. 157.

[7] S. Klein, F. Finger, R. Carius and H. Stiebig, *Proceedings of the 19th EUPVSEC*, Paris (2004), p. 1579.

[8] M. Nath, P. Roca i Cabarrocas, E. V. Johnson, A. Abramov and P. Chatterjee, *Thin Solid Films* **516** (2007), p. 6974–6978.

[9] M. N. van den Donker, S. Klein, B. Rech, F. Finger, W. M. M. Kessels and M. C. M. van de Sanden, *Applied Physics Letters* **90** (2007), p. 183504.

[10] J. Hüpkes, B. Rech, O. Kluth, T. Repmann, B. Zwaygardt, J. Müller, R. Drese and M. Wuttig, *Solar Energy Mat. and Solar Cells* **90** (2006), p. 3054.

[11] H. Meiling, *Ph.D. Thesis*, Utrecht University (1991).

[12] C. A. M. Stap, H. Meiling, G. Landweer, J. Bezemer and W. F. van der Weg, *Proceedings of the Ninth European Community Photovoltaic Solar Energy Conference*, Freiburg (1989), p. 74.

[13] E. Amanatides, D. Mataras and D. E. Rapakoulias, *Journal of Applied Physics* **90** (2001), p. 5799.

[14] A. Gordijn, Microcrystalline silicon for thin-film solar cells, *Ph.D. Thesis*, Utrecht University (2005).

[15] J. Perrin and J. P. M. Schmitt, *Chem. Phys* **67** (1982), p. 167.

[16] A. Matsuda and K. Tanaka, *Thin Solid Films* **92** (1982), p. 171.

[17] J. S. Lannin, L. J. Pilione, S. T. Kshirsagar, R. Messier and R. C. Ross, *Physical Review B* **26** (1982), p. 3506.

[18] A. Zwick and R. Carles, *Physical Review B* **48** (1993), p. 6024.

[19] C. Smit, R.A.C.M.M. Van Swaaij, H. Donker, A.M.H.N. Petit, W. M. M. Kessels and M. C. M. Van de Sanden, *Journal of Applied Physics* **94** (2003), p. 3582.

[20] S. K. O'Leary, S. R. Johnson and P. K. Lim, *Journal of Applied Physics* **82** (1997), p. 3334.

[21] W. Theiss Hard- and Software, *http://www.wtheiss.com*.

[22] M. Vanecek, A. Poruba, Z. Remeš, J. Rosa, S. Kamba, V. Vorlí˙cek, J. Meier and A. Shah, *Journal of Non-Crystalline Solids* **266** (2000), p. 519.

[23] M. Vanecek and A. Poruba, *Applied Physics Letters* **80** (2002), p. 719.

[24] B. Yan, G. Yue, J. Owens, J. Yang and S. Guha, *Conference Record of the IEEE 4th World Conference on Photovoltaic Energy Conversion* **2** (2006), p. 1477.

[25] K. Yamamoto, A. Nakajima, M. Yoshimi, T. Sawada, S. Fukuda, T. Suezaki, M. Ichikawa, Y. Koi, M. Goto and T. Meguro, *Solar energy* **77** (2004), p. 939.

[26] A. Gordijn, M. N. van den Donker, F. Finger, E. A. G. Hamers, G. J. Jongerden, W. M. M. Kessels, R. Bartl, A. M. B. van Mol, J. K. Rath, B. Rech, R. Schlatmann, R. E. I. Schropp, B. Stannowski, H. Stiebig, M. C. M. van de Sanden, R. A. C. M. M. van Swaaij and M. Zeman, *Conference Record of the IEEE 4th World Conference on Photovoltaic Energy Conversion* (2006), p. 1716.

[27] Y. Ichikawa, T. Yoshida, T. Hama, H. Sakai and K. Harashima, *Solar Energy Mat. and Solar Cells* **66** (2001), p. 107.

[28] J. K. Rath, M. Brinza and R. E. I. Schropp, *Presented at the 34th IEEE Photovoltaic Specialists Conference*, Philadelphia (2009).

[29] A. Matsuda, *Japanese Journal of Applied Physics* **43** (2004), p. 7909.

[30] W. Beyer, *Physica B: Physics of Condensed Matter* **170** (1991), p. 105.

[31] A. Fontcuberta i Morral, P. Roca i Cabarrocas and C. Clerc, *Phys. Rev. B* **69** (2004), p. 307.

[32] P. C. P. Bronsveld, J. K. Rath, R. E. I. Schropp, T. Mates, A. Fejfar, B. Rezek and J. Kocka, *Applied Physics Letters* **89** (2006), p. 051922.

[33] R. J. Koval, J. Koh, Z. Lu, L. Jiao, R. W. Collins and C. R. Wronski, *Applied Physics Letters* **75** (1999), p. 1553.

[34] D. V. Tsu, B. S. Chao, S. R. Ovshinsky, S. Guha and J. Yang, *Applied Physics Letters* **71** (1997), p. 1317.

[35] S. Guha, J. Yang, D. L. Williamson, Y. Lubianiker, J. D. Cohen and A. H. Mahan, *Applied Physics Letters* **74** (1999), p. 1860.

[36] C. Koch, M. Ito and M. Schubert, *Solar Energy Mat. and Solar Cells* **68** (2001), p. 227.

[37] C. Böhm and J. Perrin, *J. Phys. D, Appl. Phys* **24** (1991), p. 865–881.

[38] P. Belenguer and J. P. Boeuf, *Physical review. A* **41** (1990), p. 4447.

[39] G. Oversluizen and W. H. M. Lodders, *Journal of Applied Physics* **83** (1998), p. 8002.

[40] A. A. Fridman, L. Boufendi, T. Hbid, B. V. Potapkin and A. Bouchoule, *Journal of Applied Physics* **79** (1996), p. 1303.

[41] L. Boufendi and A. Bouchoule, *Plasma Sources Science and Technology* **3** (1994), p. 262.

[42] L. Landau and E. Teller, *Physikalische Zeitschrift der Sowjetunion* **10** (1936), p. 34.

[43] G. J. Nienhuis, W. J. Goedheer, E. A. G. Hamers, W. van Sark and J. Bezemer, *Journal of Applied Physics* **82** (1997), p. 2060.

[44] E. A. G. Hamers, W. van Sark, J. Bezemer, H. Meiling and W. F. Van der Weg, *Journal of non-crystalline solids* **226** (1998), p. 205.

[45] S. Vepřek, F. A. Sarrott, S. Rambert and E. Taglauer, *Journal of Vacuum Science & Technology A: Vacuum, Surfaces, and Films* **7** (1989), p. 2614.

[46] A. H. M. Smets, W. M. M. Kessels and M. C. M. van de Sanden, *Journal of Applied Physics* **102** (2007), p. 073523.

[47] A. Fontcuberta i Morral and P. Roca i Cabarrocas, *Journal of Non-Crystalline Solids* **299** (2002), p. 196.

[48] H. Tawara and T. Kato, *Name: At. Data Nucl. Data Tables* **36** (1987), p. 167.

[49] T. Roschek, T. Repmann, J. Müller, B. Rech and H. Wagner, *Journal of Vacuum Science & Technology A: Vacuum, Surfaces, and Films* **20** (2002), p. 492.

[50] O. Vetterl, F. Finger, R. Carius, P. Hapke, L. Houben, O. Kluth, A. Lambertz, A. Mück, B. Rech and H. Wagner, *Solar Energy Mat. and Solar Cells* **62** (2000), p. 97.

[51] J. K. Rath, R. H. J. Franken, A. Gordijn, R. E. I. Schropp and W. J. Goedheer, *Journal of Non-Crystalline Solids* **338** (2004), p. 56.

[52] G. Dingemans, M. N. van den Donker, A. Gordijn, W. M. M. Kessels and M. C. M. van de Sanden, *Applied Physics Letters* **91** (2007), p. 161902.

[53] R. W. Collins, A. S. Ferlauto, G. M. Ferreira, C. Chen, J. Koh, R. J. Koval, Y. Lee, J. M. Pearce and C. R. Wronski, *Solar Energy Mat. and Solar Cells* **78** (2003), p. 143.

[54] N. Layadi, P. Roca i Cabarrocas, B. Drevillon and I. Solomon, *Physical Review-Section B-Condensed Matter* **52** (1995), p. 5136.

[55] P. van Veenendaal, G. W. M. van der Mark, J. K. Rath and R. E. I. Schropp, *Thin Solid Films* **430** (2003), p. 41.

[56] B. Strahm, A. A. Howling, L. Sansonnens, C. Hollenstein, U. Kroll, J. Meier, C. Ellert, L. Feitknecht and C. Ballif, *Solar Energy Mat. and Solar Cells* **91** (2007), p. 495.

[57] A. Matsuda, *Thin Solid Films* **337** (1999), p. 1.

[58] K. Saitoh, M. Kondo, M. Fukawa, T. Nishimiya, A. Matsuda, W. Futako and I. Shimizu, *Applied Physics Letters* **71** (1997), p. 3403.

[59] H. Shirai, B. Drevillon and I. Shimizu, *Japanese journal of applied physics* **33** (1994), p. 5590.

[60] S. Sriraman, S. Agarwal, E. S. Aydil and D. Maroudas, *Nature* **418** (2002), p. 62.

[61] U. Kroll, J. Meier, A. Shah, S. Mikhailov and J. Weber, *Journal of Applied Physics* **80** (1996), p. 4971.

[62] J. E. Gerbi and J. R. Abelson, *Journal of Applied Physics* **89** (2001), p. 1463.

[63] J. Perrin, *J. of Non-Cryst. Solids* **137** (1991), p. 639.

[64] G. G. A. Perkins, E. R. Austin and F. W. Lampe, *J. Am. Chem. Soc* **101** (1979), p. 1109.

[65] Y. Harada, J. N. Murell and H. H. Sheena, *Chem. Phys. Letters* **1** (1963), p. 595.

[66] A. G. Engelhardt and A. V. Phelps, *Physical Review* **131** (1963), p. 2115.

[67] S. Klein, F. Finger, R. Carius and M. Stutzmann, *Journal of Applied Physics* **98** (2005), p. 024905.

[68] G. Dingemans, M. N. van den Donker, D. Hrunski, A. Gordijn, W. M. M. Kessels and M. C. M. van de Sanden, *Applied Physics Letters* **93** (2008), p. 111914.

[69] J. Perrin, O. Leroy and M. C. Bordage, *Contrib. Plasma Phys* **36** (1996), p. 3.

[70] P. M. Meijer, The Electron Dynamics of RF Discharges, *Ph.D. Thesis*, Utrecht University, The Netherlands (1991).

[71] J. D. P. Passchier, Numerical Fluid Models for RF Discharges, *Ph.D. Thesis*, Utrecht University, The Netherlands (1994).

[72] B. Boussadkat, Optical emission and radical production in silane-hydrogen radio-frequency discharges: A numerical study with a one-dimensional fluid model, *Master Thesis*, Utrecht University, The Netherlands (2008).

[73] J. R. Doyle, D. A. Doughty and A. Gallagher, *Journal of Applied Physics* **68** (1990), p. 4375.

[74] J. Perrin, Y. Takeda, N. Hirano, Y. Takeuchi and A. Matsuda, *Surface Science* **210** (1989), p. 114.

[75] A. Matsuda, K. Nomoto, Y. Takeuchi, A. Suzuki, A. Yuuki and J. Perrin, *Surface Science* **227** (1990), p. 50.

[76] J. Felts and E. Lopata, *Journal of Vacuum Science & Technology A: Vacuum, Surfaces, and Films* **6** (1988), p. 2051.

[77] M. Kondo, M. Fukawa, L. Guo and A. Matsuda, *Journal of Non-Crystalline Solids* **266** (2000), p. 84.

[78] M. N. van den Donker, B. Rech, F. Finger, L. Houben, W. M. M. Kessels and M. C. M. van de Sanden, *Progress in Photovoltaics: Research and Applications* **15** (2007), p. 291–301.

[79] D. R. Lide, CRC handbook of chemistry and physics: a ready-reference book of chemical and physical data, CRC press, (2009).

[80] R. R. Arya, A. Catalano and R. S. Oswald, *Applied Physics Letters* **49** (1986), p. 1089.

[81] B. Yan, G. Yue, J. Yang, S. Guha, D. L. Williamson, D. Han and C. S. Jiang, *Applied Physics Letters* **85** (2004), p. 1955.

[82] A. H. M. Smets, T. Matsui and M. Kondo, *Journal of Applied Physics* **104** (2008), p. 034508.

[83] B. Strahm, C. Hollenstein and A. A. Howling, *Progress in Photovoltaics: Research and Applications* **16** (2008), p. 687.

[84] B. Strahm, A. A. Howling and C. Hollenstein, *Materials Research Society Symposium Proceedings* **1066** (2008), p. 3.

[85] M. N. van den Donker, B. Rech, F. Finger, W. M. M. Kessels and M. C. M. Van de Sanden, *Applied Physics Letters* **87** (2005), p. 263503.

[86] I. Horcas, R. Fernandez, J. M. Gomez-Rodriguez, J. Colchero, J. Gomez-Herrero and A. M. Baro, *Review of Scientific Instruments* **78** (2007), p. 013705.

[87] POV-Ray, *http://www.povray.org/*.

[88] L. Houben, C. Scholten, M. Luysberg, O. Vetterl, F. Finger and R. Carius, *Journal of Non-Crystalline Solids* **299** (2002), p. 1189.

[89] A. Shah, P. Torres, R. Tscharner, N. Wyrsch and H. Keppner, *Science* **285** (1999), p. 692.

[90] J. Meier, J. Spitznagel, U. Kroll, C. Bucher, S. Fay, T. Moriarty and A. Shah, *Thin Solid Films* **451** (2004), p. 518.

[91] S. Shimizu, A. Matsuda and M. Kondo, *Solar Energy Mat. and Solar Cells* **92** (2008), p. 1241.

[92] C. Manfredotti, F. Fizzotti, M. Boero, P. Pastorino, P. Polesello and E. Vittone, *Physical Review B* **50** (1994), p. 18046.

[93] F. Meillaud, E. Vallat-Sauvain, X. Niquille, M. Dubey, A. Shah and C. Ballif, *Journal of Non-Crystalline Solids* **352** (2006), p. 1851.

[94] A. Klaver, Irradiation-induced degradation of amorphous silicon solar cells in space, *Ph.D. Thesis*, Delft University of Technology, The Netherlands (2007).

[95] J. Kuendig, M. Goetz, J. Meier, P. Torres, L. Feitknecht, P. Pernet, X. Niquille, A. Shah, L. Gerlach and E. Fernandez, *Proc. 16th EPVSEC* (2000), p. 986.

[96] T. Markvart, *Journal of Materials Science: Materials in Electronics* **1** (1990), p. 1.

[97] M. Alurralde, M. J. L. Tamasi, C. J. Bruno, M. G. Martínez Bogado, J. Plá, J. Fernández Vázquez, J. Durán, J. Schuff, A. A. Burlon and P. Stoliar, *Solar Energy Mat. and Solar Cells* **82** (2004), p. 531.

[98] M. Yamaguchi, S. J. Taylor, M. J. Yang, S. Matsuda, O. Kawasaki and T. Hisamatsu, *Journal of Applied Physics* **80** (1996), p. 4916.

Abstract

Hydrogenated amorphous silicon (a-Si:H) and hydrogenated nanocrystalline silicon (nc-Si:H), deposited using Very High Frequency Plasma Enhanced Chemical Vapour Deposition (VHF PEVCD) on substrates with a temperature of about 200 °C and at deposition rates well below 1 nm/s, are in use in thin film large area solar cells at an increasing production scale. However, the range of applications could be greatly extended if these materials would be deposited at higher growth rates and/or at lower substrates temperatures. In this thesis several obstacles are identified on the road towards this goal and a variety of strategies is presented to overcome these hurdles.

Reduction of the substrate temperature for plasma deposition of a-Si:H solar cells commonly results in a decrease of the performance, which is often attributed to changes in the surface chemistry with respect to the optimal regime. In this thesis the focus is more on the effects of the reduced substrate temperature on the gas phase chemistry and its effects on the plasma physics. An experiment was set up to probe the behaviour of the ion energy under various conditions. It was found that both the ion energy and the ion flux are drastically reduced when the substrate temperature is lowered, from the optimum temperature around 200 °C, towards room temperature. The beneficial effect of an increased hydrogen dilution of the silane source gas was explained in terms of an increased energy flux due to ions. Furthermore, an increase of powder formation with decreasing gas temperatures was suggested, and this was confirmed by measurement of the plasma impedance.

The transition from a-Si:H growth to nc-Si:H growth is determined by the relative fluxes of atomic hydrogen and silicon species, and can be predicted using the optical emission associated with the origin of these fluxes. However, increase of the deposition rate is achieved by an increase in gas flow and pressure and electrical power, giving rise to an increase in both rate and density of gas phase reactions, complicating this prediction of the transition. Using a model that relates gas phase reactions, electron temperature, optical emission and aforementioned fluxes, and which is calibrated using data from a 1-D computer simulation, a correction factor is derived that is purely based on measurable

quantities, and that considerably extends the range of deposition conditions for which the phase transition can be predicted using optical emission.

Due to the increased pressure, power and intentional higher degree of gas utilization, deposition at a higher rate has a number of aspects that is not present in the low deposition rate regime. Due to the high degree of depletion, manipulation of the phase composition can not be done via variation of the hydrogen dilution. It was shown that back diffusion of silane into the plasma region is as probable as in the low deposition rate regime, and that the stabilisation time is a few tens of seconds, which is in the same order as that in the low deposition rate regime, but since the deposition rate is roughly ten times higher, a larger section of the film is affected. This explains the thick incubation layer that was encountered for high deposition rate nc-Si:H films. The thickness of the incubation layer could be strongly reduced by starting the deposition with a hydrogen filled reactor and a short hydrogen plasma. Further control of the phase composition was achieved by manipulation of the degree of silane depletion via the silane flow.

By controlling the crystalline ratio via variation of the VHF power, a series of layers was deposited to explore the potential of high deposition rate for both nc-Si:H and a-Si:H materials. The photosensitivity and activation energy for both types of material were of device quality. A solar cell with an a-Si:H absorber layer grown at 3.2 nm/s had a conversion efficiency of 6.4% and another solar cell with a nc-Si:H absorber layer deposited at 4.5 nm/s showed a conversion efficiency of 6.4% as well. The light induced degradation of the efficiency was 20% relatively for the a-Si:H solar cell and no degradation was observed for the nc-Si:H solar cell. The high deposition rate nc-Si:H cell showed a defect density that was an order of magnitude higher compared to low deposition rate, performance-optimized nc-Si:H cells. Proton irradiation of the nc-Si:H solar cell revealed that radiation resistance was comparable to that of a-Si:H cells from literature, but because nc-Si:H are necessarily thicker, these type of solar cells show stronger degradation.

The results presented in this thesis can be applied in industrial, inline systems for the production of high deposition rate nanocrystalline silicon solar cells with enhanced homogeneity and for the quality improvement of solar cells deposited at low substrate temperatures on less expensive substrates, thus reducing production costs.

Samenvatting in het Nederlands

Amorf silicium (a-Si:H) en nanokristallijn silicium (nc-Si:H), gegroeid met hoogfrequente plasmageïnduceerde chemische dampdepositie (VHF PECVD) op substraten met een temperatuur van ongeveer 200 °C en met groeisnelheden aanzienlijk lager dan 1 nm/s, worden op steeds grotere schaal gebruikt voor de productie van dunnefilm zonnecellen op grote oppervlakken. Het scala aan toepassingen zou echter flink uitgebreid kunnen worden als deze materialen gegroeid zouden worden met hogere groeisnelheden en/of bij lagere substraattemperaturen. In dit proefschrift worden verscheidene obstakels onderkend op de weg naar dit doel en een verscheidenheid aan strategiën wordt gepresenteerd om deze hindernissen te nemen.

Verlaging van de substraattemperatuur voor de plasmadepositie van a-Si:H zonnecellen resulteert over het algemeen in verminderde prestaties, hetgeen dikwijls wordt toegeschreven aan veranderingen in de oppervlaktechemie ten opzichte van de optimale situatie. In dit proefschrift ligt de nadruk meer op de effecten van de verminderde substraattemperatuur op de chemie van de gasfase en de effecten daarvan op de plasmafysica. Een experiment is opgezet om het gedrag van de ionenenergie te meten in verschillende omstandigheden. Zowel de ionenenergie als de ionenflux bleken sterk af te nemen bij een dalende substraattemperatuur, vanaf de optimale temperatuur rond de 200 °C, tot kamertemperatuur. Het gunstige effect van een verdunning van het brongas silaan met waterstof wordt verklaard vanuit de toegenomen energie flux die wordt veroorzaakt door de ionen. Verder wordt een toename van de stofvorming verwacht bij lagere gastemperaturen, hetgeen bevestigd wordt door impedantiemetingen aan het plasma.

De overgang van het groeien van a-Si:H naar het groeien van nc-Si:H wordt bepaald door de fluxverhouding van atomair waterstof enerzijds en siliciumatomen in diverse moleculaire samenstellingen anderzijds. Deze overgang kan voorspeld worden door gebruik te maken van de optische emissie die gerelateerd is aan het ontstaan van deze fluxen. Wanneer echter de groeisnelheid wordt verhoogd, door middel van een verhoging van de druk en het elektrisch vermogen en een vergroting van de hoeveelheid toegevoerde procesgassen, nemen chemische reacties in de gasfase toe in aantal en frequentie, waardoor de voorspelling van de overgang gecompliceerder wordt. Door gebruik te maken van een

model dat de chemische reacties in de gasfase, de elektronentemperatuur, de optische emissie en de fluxen van siliciumatomen en atomair waterstof met elkaar in verband brengt, en dat geijkt is met behulp van data uit een 1-D computersimulatie, is een correctiefactor afgeleid die enkel gebaseerd is op meetbare grootheden, en die het bereik van depositiecondities waarvoor de faseovergang voorspeld kan worden vanuit de optische emissie aanzienlijk vergroot.

Vanwege de toegenomen druk, het toegenomen vermogen en de opzettelijk hogere benuttingsgraad van het brongas, heeft hogesnelheidsdepositie een aantal aspecten die bij lagere groeisnelheden geen rol spelen. Vanwege de hoge benuttingsgraad kan niet worden volstaan met variatie van de hoeveelheid toegevoerd waterstof om de fasesamenstelling van het gegroeide materiaal te manipuleren. Terugdiffusie van silaan naar de plasmazone is net zo waarschijnlijk bij hoge groeisnelheid als bij lage groeisnelheid, en ook de stabilisatietijd van het gasmengsel na aanvang van de depositie heeft dezelfde orde van grootte, namelijk enkele tientallen seconden. Omdat echter de depositiesnelheid in het eerste geval een factor tien hoger ligt, heeft hetzelfde verschijnsel effect op een veel dikker deel van de gegroeide laag. Dat verklaart de dikke amorfe incubatielaag die werd aangetroffen in nc-Si:H lagen met hoge groeisnelheid. De dikte van de incubatielaag kon sterk verminderd worden door de depositie te starten met een reactor gevuld met waterstof en een aantal seconden waterstofplasma. Verdere controle over de fasesamenstelling is bereikt door variatie van de benuttingsgraad via de silaantoevoer.

Er is een serie siliciumlagen gegroeid waarbij de kristallijne fractie werd gecontroleerd door variatie van het toegevoerde VHF vermogen, teneinde het potentieel van zowel a-Si:H als nc-Si:H materialen, die met hoge groeisnelheid zijn gemaakt, te onderzoeken. De lichtgevoeligheid en de activeringsenergie van de beste materialen uit de serie zijn van 'device quality'. Een zonnecel met een a-Si:H absorptielaag gegroeid met 3.2 nm/s had een omzettingsrendement van 6.4% en een andere zonnecel met een nc-Si:H absorptielaag gegroeid met 4.5 nm/s had eveneens een omzettingsrendement van 6.4%. De lichtgeïnduceerde vermindering van het omzettingsrendement was 20% relatief voor de a-Si:H zonnecel. De nc-Si:H zonnecel vertoonde geen vermindering van het omzettingsrendement. De nc-Si:H zonnecel met hoge groeisnelheid is een orde van grootte

defectrijker dan een nc-Si:H zonnecel met lage groeisnelheid (0.5 nm/s) die is geoptimaliseerd voor een hoog omzettingsrendement. Bij bestraling met protonen van de nc-SI:H zonncel is gebleken dat de stralingshardheid vergelijkbaar is met die van a-Si:H zonnecellen uit de literatuur, maar omdat de nc-Si:H zonnecellen noodzakelijkerwijs dikker zijn, vertonen zij een sterkere achteruitgang van het rendement.

De in dit proefschrift beschreven resultaten kunnen toegepast worden in industriële productielijnen voor nanokristallijne zonnecellen met hoge groeisnelheid en verbeterde homogeniteit, en voor de kwaliteitsverbetering van zonnecellen die bij lage temperatuur op goedkopere substraten worden gegroeid, zodat de productiekosten lager worden.

Publications

Publications within the scope of this thesis

A.D. Verkerk, J.K. Rath and R.E.I. Schropp, High deposition rate nanocrystalline silicon with enhanced homogeneity, *presented at the International Conference on Amorphous and Nanocrystaline Semiconductors (ICANS23)*, Utrecht, The Netherlands, August 23-28, 2009; submitted to Physica Status Solidi (c).

A.D. Verkerk, J.K. Rath and R.E.I. Schropp, Degradation of thin film nanocrystalline silicon solar cells with 1 MeV protons, *presented at E-MRS Spring Meeting*, Strasbourg, France, June 8-12, 2009; submitted for publication.

J.K. Rath, M.M. de Jong, A. Verkerk, M. Brinza, R.E.I. Schropp, Gas phase conditions for obtaining device quality amorphous silicon at low temperature and high deposition rate. *Mater. Res. Soc. Symp. Proc.* **1153** (2009) 1153-A22-04.

J.K. Rath, A.D. Verkerk, M. Brinza, R.E.I. Schropp, W.J. Goedheer, V.V. Krzhizhanovskaya, Y.E. Gorbachev, K.E. Orlov, E.M.Khilkevitch, A.S. Smirnov. Gas phase considerations for the deposition of thin film silicon cells by VHF-PECVD at low substrate temperatures. *Materials Science and Engineering: B* **159-160** (2009) 38-43.

A.D. Verkerk, M.M. de Jong, J.K. Rath, M. Brinza, R.E.I. Schropp, W.J. Goedheer, V.V. Krzhizhanovskaya, Y.E. Gorbachev, K.E. Orlov, E.M. Khilkevitch, A.S. Smirnov. Compensation of decreased ion energy by increased hydrogen dilution in plasma deposition of thin film silicon solar cells at low substrate temperatures. *Materials Science and Engineering: B* **159-160** (2009) 53-56.

A.D. Verkerk, J.K. Rath, R.E.I. Schropp, Light-induced improvement of very fast deposited microcrystalline silicon solar cells, *Proceedings of the 22nd European Photovoltaic Solar Energy Conference*, Milan, Italy (2007) 1843-1846.

Publications outside of the scope of this thesis

J.K. Rath, Y. Liu, M. Brinza, A. Verkerk, C. van Bommel, A. Borreman and R.E.I. Schropp, Recent advances in very high frequency plasma enhanced CVD process for the fabrication of thin film silicon solar cells, *Thin Solid Films* **517** (2009) 4758.

V. Verlaan, W.M. Arnold Bik, C.H.M. van der Werf, R. Bakker, Z.S. Houweling, A.D. Verkerk, I.G. Romijn, D.M. Borsa, A.W. Weeber, S.L. Luxemburg, M. Zeman, H.F.W. Dekkers, and R.E.I. Schropp, The effect of composition on the bond structure and refractive index of silicon nitride deposited with HWCVD and PECVD. *Thin Solid Films* **517** (2009) 3499–3502.

R. Bakker, V.Verlaan, A.D. Verkerk, C.H.M. van der Werf, L. van Dijk, H. Rudolph, J.K. Rath and R.E.I. Schropp, Heat transfer model of an iCVD reactor. *Thin Solid Films* **517** (2009) 3555-3558.

P.C.P. Bronsveld, A.D. Verkerk, T. Mates, A. Fejfar, J.K. Rath, R.E.I. Schropp, Relation between electronic properties and density of crystalline agglomerates in microcrystalline silicon, *MRS proceedings* **989** (2007) A7.1.

J.K. Rath, A.D. Verkerk, R.H. Franken, C.O. van Bommel, C.H.M. van der Werf, A. Gordijn, and R.E.I. Schropp, Implementation of Highly Stable Microcrystalline Silicon by VHF PECVD at High Deposition Rate in Micromorph Tandem Cells, *Conference Record of the 2006 IEEE 4th World Conference on Photovoltaic Energy Conversion* **2** (2006) 1473-1476.

Dankwoord

Aan het einde van dit proefschrift neem ik graag nog even de ruimte om degenen te bedanken die belangrijk voor mij zijn geweest, niet alleen bij de totstandkoming van dit proefschrift, maar ook gedurende het hele promotietraject van de afgelopen vier jaar.

Ruud Schropp, ik begin met jou. Bedankt voor het in mij gestelde vertrouwen. Bedankt voor alle suggesties op teksten van artikelen en van het proefschrift, die er vaak toe leidden dat de beoogde boodschap veel sterker uit de verf kwam.

Jatin Rath, dankjewel voor de dagelijkse begeleiding in de vorm van advies ten aanzien deposities en experimenten. Je hebt talent om in elk resultaat wel een positief aspect te ontdekken. Zeer erkentelijk ben ik ook jou voor het vele leeswerk en de verbetersuggesties bij dit boekje en ook bij alle overige publicaties.

De leden van de beoordelingscommissie, Wim Goedheer – bedankt voor je commentaar op mijn proefschrift en de heldere verwoording van diverse onderwerpen in de plasmafysica; Richard van de Sanden – bedankt voor je opbouwende commentaar en de diverse vraag- en uitroeptekens die ik aantrof in het door jou doorgenomen manuscript; Henrik Rudolph en Jaap Dijkhuis: allen bedankt voor jullie tijd en energie.

Caspar van Bommel, Martin Huijzer en Arjen Bink: bedankt voor alle zonnecellen en laagjes die jullie voor me hebben geproduceerd, en al het stof dat jullie zonder morren elke keer weer uit de reactor hebben verwijderd. Karine van der Werf, bedankt voor je praktische adviezen op laboratoriumgebied en het ter beschikking stellen van je bijzonder complete verzameling proefschriften. Ruurd Lof, je hield trouw alle karakterisatie-apparatuur aan de gang en als bonus kreeg ik spontane colleges van je over uiteenlopende zonnecelaspecten. Roberto Ackermann Ietswaart, bedankt voor je technische hulp en je enthousiaste klimverslagen. Wim Arnold Bik, bedankt voor het maken van de protonenbundel.

Postdocs en collega-promovendi Hongbo Li, Monica Brinza, Ronald Franken, Minne de Jong, Paula Bronsveld, Yanchao Liu, Jan Willem Schüttauf, Marites Violanda, Mirela Georgescu, Silvester Houweling, Xin Jin en Jessica de Wild: bedankt voor alle goede samenwerking en gezelligheid.

Hardlopers Hanno Goldbach, Robert Stolk en Arjen Vredenberg: met elkaar hebben we heel wat sportieve en gezellige uurtjes doorgebracht; bedankt voor jullie gezelschap.

Riny de Haas, bij jou kon ik altijd even terecht voor een praatje en vooral tijdens het laatste jaar heb ik daar nogal eens dankbaar gebruik van gemaakt. Bedankt!
Janna Koetze, bedankt voor de gezelligheid en voor al je krabbels.

Ruud Bakker, Timon van Wijngaarden en Vasco Verlaan: jullie zouden ook in een paar andere rijtjes hierboven passen, maar daarnaast zijn jullie in de afgelopen jaren geweldige vrienden gebleken, en dáárvoor ben ik jullie het meest dankbaar.

Mijn ouders, bedankt voor jullie betrokkenheid en onvoorwaardelijke liefde.

Lieve Annechien, Marit en Olger, de afronding van het proefschrift vond plaats in een roerige periode: Vakantie en kraamtijd werden niet gespaard. Bedankt dat jullie er steeds waren om me te steunen, op te vrolijken en liefde te geven.

Curriculum Vitae

The author was born in Maarssen in The Netherlands on October 22, 1979. He obtained his secondary school diploma in 1997 from the Dr. F. H. de Bruijne Lyceum in Utrecht. After a year of contemplation and general education at the Evangelische Hogeschool in Amersfoort, he started a study of Applied Physics in 1998 at the University of Twente in Enschede. In 2000, he was a member of the organising committee of a Christian student conference and, in 2001, he became the chairman of the board of the Reformatorische Studenten Kring for a period of one year. An internship at TNO on the signal processing for an airborne surveillance radar contributed to his interests in software development. The subject of his master thesis was the development of a surface wave launcher for the application of microwave discharges in a XeCl laser mixture, in the Laser Physics group of Klaus Boller. After graduation in 2005 he went on to investigate the application of plasma's of lower, but still very high frequency discharges for the deposition of thin film silicon solar cells as an AIO in the Physics of Devices group of Ruud Schropp at Utrecht University. Besides the experimental work, he assisted in the teaching of various courses in physics and developed a diverse collection of software tools for data analysis. A part of the results of the past four years is described in this thesis.